Poster A

Experimental and Theoretical Studies of a Bond-Forming Reaction Between CF_2^{2+} and X_2O (X = H, D)

N. Lambert, S. D. Price and N. Kaltsoyannis

Department of Chemistry, University College London, 20 Gordon Street, London WC1H 0AJ, UK

Abstract

Currently unpublished work from UCL indicates the existence of a bond-forming reaction between CF_2^{2+} and H_2O to yield the product ion OCF^+. In the current study, reactions of CF_2^{2+} + D_2O were monitored at laboratory-frame collision energies from 3.0 V to 12.0 V using time-of-flight mass spectrometry. As with the collisions with H_2O, reactions with D_2O also yield the OCF^+ product. In addition, F^+ and HF^+ were *not* observed. This indicates that the products of the bond-forming reaction are OCF^+, H^+ and neutral(s). Results also suggest that greater yields of OCF^+ are produced in collisions with D_2O rather than with H_2O.

Computational methods were used to probe the potential energy surfaces of the bond-forming reactions of CF_2^{2+} + X_2O (X = H, D). Optimized geometries and vibrational frequencies of local extrema were calculated using the *Gaussian98* program with both the B3P86 and B3LYP methods. In all calculations the 6-311++G(2df,2pd) basis set was used. These structures and their energies and frequencies as obtained by these two methods were compared. Stationary-point energies were improved by performing single-point calculations at the CCSD(T)/6-311++G(2df,2pd) level on geometries optimized at the hybrid levels. A reactive mechanism loosely analogous to that presented by Mrásek *et al.* [1] for the bond-forming reaction of CO_2^{2+} + H_2 has been determined. The products OCF^+ + H^+ + HF were found to lie on the lowest energy product channel asymptote, in agreement with experimental results. Information obtained from these calculations was also used to determine rate constants for these reactions using statistical Rice-Ramsperger-Kassel-Marcus quasiequilibrium theory [2].

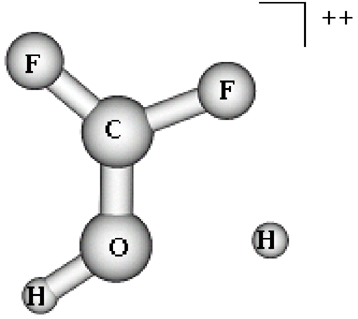

Figure 1: A transition state on the $CF_2^{2+} + H_2O \rightarrow OCF^+ + H^+ + HF$ reaction path

References

---

[1] Mrásek, L.; Zabka, J.; Dolejšek, Z.; Hrušák, J.; Herman, Z. *J. Phys. Chem. A*. **2000**, *104*, 7294.
[2] Baer, T.; Mayer, P. M. *J. Am. Chem. Soc. Mass Spectrom.* **1997**, *8*, 103.

Energy dependence of the reaction rate constants of Ar^+, Ar^{++} and N_2^+ ions with Cl_2

P. Lukáč[1], **W. Lindinger**[+], **I. Morva**[2], **Ľ. Holubčík**[1]

Institut für Ionenphysik, Leopold-Franzens Universität, Innsbruck, Technikerstrasse 25 A-6025 Innsbruck, Austria

[1] Plasma Physics Department and [2]Institute of Physics, FMFI, Comenius University, Mlynská dolina F2, SK-842 48 Bratislava, Slovakia

[+] died on February 16, 2001

Introduction

Dry etching processes using low temperature plasmas in Cl_2 and in Cl_2-noble gas or nitrogen mixtures are common in the manufacture of semiconductor devices, but their chemical mechanisms are often poorly understood. It was shown by F.X. Campos et al [1] that hyperthermal Cl_2 etches room temperature silicon at least ten times faster than thermal Cl_2 and that the etching rate increases significantly at Cl_2 kinetic energies larger than 3 eV. More detailed analysis of neutral mean kinetic energy of Ar, N_2, Cl_2 in ECR plasma source has been carried out by R.S. Goodman et. al. [2]. This energy was varied between 0.04 and 0.45 eV. Enhancement in neutral mean kinetic energy has shown a strong correlation with ion fluxes of atomic and molecular species out of the source for all source gases studied. The average translation energy of Cl^+ ions (determined by LIF Doppler method) gave values in the range 0.24 – 0.61 eV. [3] These values depend also on the gas pressure. It is surprising, but till now only S.G. Lias [4] has measured some reactions of positive inert gas ions with chlorine by ICR method. No other reaction rate coefficient can be found in review papers [5,6] besides our previous reported value [7]. Therefore the aim of this paper is to present the results of the reaction rate constant measurements of Ar^+, Ar^{++}, N_2^+ ions with chlorine as a function of mean relative kinetic energy.

Experimental apparatus

The Innsbruck Flow Drift Tube (IFDT) apparatus was used for the present investigation. It has been described in detail in the literature [8], thus only a brief outline of its main features needs to be given here. Ions were produced in a simple electron impact ion source operating with variable electron energy instead of hollow cathode discharge source. These ions enter the drift chamber through a small orifice of diameter 50 μm and through the helium, neon and argon buffer gas under the influence of an electric field towards the downstream end plate of the chamber, when part of the ions enter in the analyzing system (quadrupole mass spectrometry) through an orifice in the end plate. A constant flow of buffer gas through the drift tube is maintained at a small enough rate, so that the drift velocity of the ions is always high relative to the bulk flow velocity of the buffer gas through the drift section. Addition of chlorine gas (of research grade purity) to the buffer gas causes a decline of the count rate of reactant ions (and an increase of new produced ions) from which the rate coefficient of the reaction can be calculated in the usual way [8].

Measurements were performed at various E/N values, where E is the electric field strength and N the buffer gas density in the drift section. The mean relative kinetic energy KE_{cm} between the ions and the neutral chlorine Cl_2 was calculated using the Wanniers formula [9] in the usual way. Then according to [10] the KE_{cm} is expressed as:

$$KE_{CM} = \frac{M(m+M_i)}{2(M+M_i)} v_d^2 + \frac{3}{2} kT \qquad (1)$$

where M, m and M_i are the masses of the reactant neutral (in our case Cl_2), of the buffer gas and of the reactant ions, respectively, v_d is the drift velocity of the reactant ions in the buffer gas, k is the Boltzmann constant and T is the neutral gas temperature (a room temperature).

Results and discussion

It is common that rate coefficients obtained in drift tube experiments are expressed as a function of KE_{cm} , derived using Eq.(1). Reaction rate coefficients obtained for the total destruction of N_2^+, Ar^+ and Ar^{++} by reaction with chlorine Cl_2 as a function of KE_{cm} are shown in Fig. 1, Fig.2 and Fig.3, respectively for different buffer gas pressures.

The reaction of N_2^+ with Cl_2 has the large reaction rate coefficients. The remarkable changes of rate coefficients from 4 x 10^{-10} cm^3s^{-1} to 2 x 10^{-9} cm^3s^{-1} are observed in energy range from thermal up to a few eV KE_{cm}. The dominant reaction is

$$N_2^+ + Cl_2 \rightarrow Cl_2^+ + N_2 \qquad (2)$$

and for it only decline was observed, so indicating that vibrationally excited N_2^+ either reacts at the same rate as non-excited N_2^+ or that $N_2^+(X, v = 0)$ is quenched faster (mainly in He buffer gas) than it does react with Cl_2. Similar rate coefficients for both vibrationally excited and non excited N_2^+ could be expected in case of these two reactions, as both reactions are fast, even at room temperature and in general fast reactions hardly ever show a significant influence by the vibrational excitation of the ions.

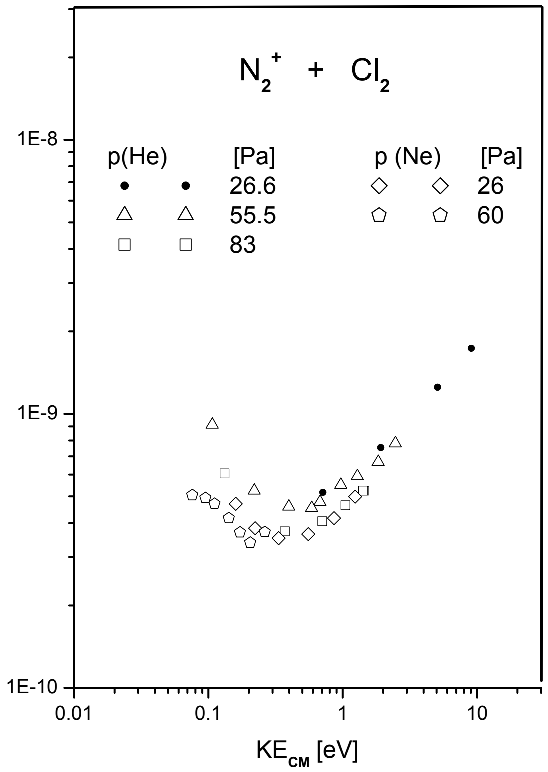

Fig.1: Rate coefficients k for the reactions of N_2^+ ions with Cl_2 in dependence on the relative mean kinetic energy KE_{cm}

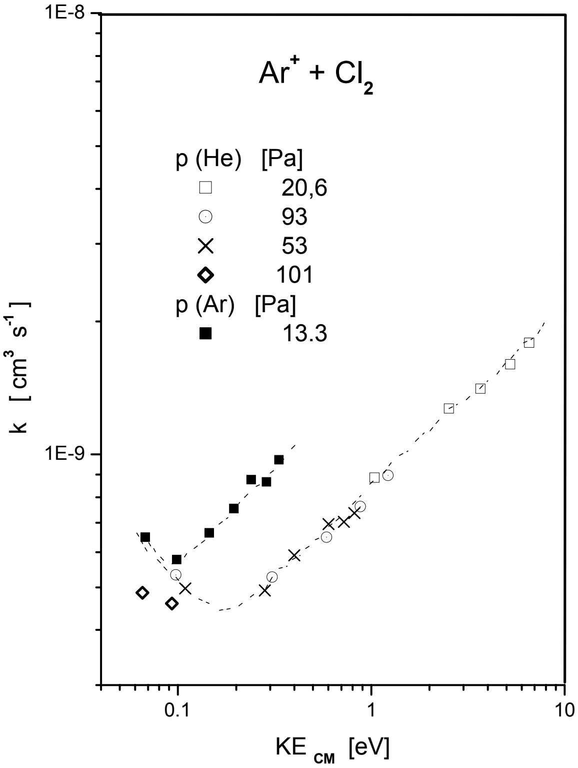

Fig. 2. Rate coefficients k for the reaction of Ar^+ ions with the Cl_2 in dependence on the relative mean kinetic energy KE_{cm}

There are three important and energetically possible reactions of Ar^+ ions with Cl_2:

$Ar^+ + Cl_2 \rightarrow Cl_2^+ + Ar$ more than 50 % (3)
$Ar^+ + Cl_2 \rightarrow Cl^+ + Cl + Ar$ (4)
$Ar^+ + Cl_2 \rightarrow ArCl^+ + Cl$ less than a few percent (5)

The branching ratio between reaction (3) and (4) was measured only for near thermal energy KE_{cm}. This ratio is similar to that observed by Lias [4] and R.S.Goodman [2]. The present results for total reaction rate coefficient of Ar^+ with Cl_2 shown in Fig.2 are about of one order higher than those presented by Lias. (1.5×10^{-10} cm^3s^{-1}) [4].

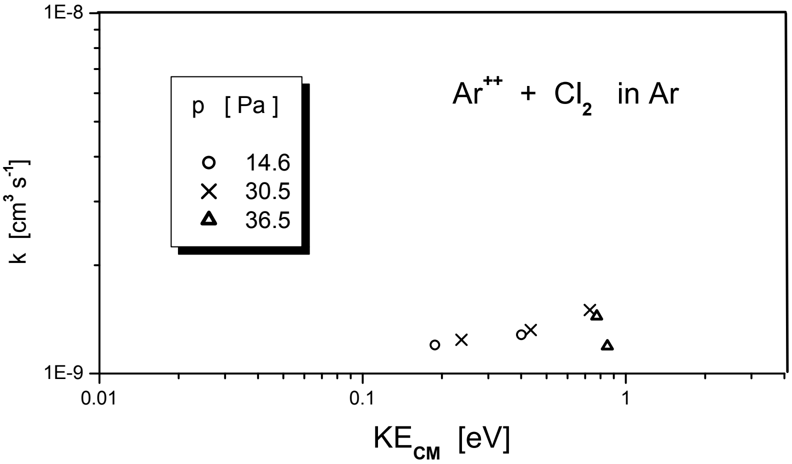

Fig. 3 Rate coefficients *k* for the reaction of A^{++} ions with Cl_2 in argon in dependence on the mean relative kinetic energy

The reaction of doubly ionized argon ions Ar^{++} with chlorine Cl_2 is important for excimer laser. It can be expressed as

$$Ar^{++} + Cl_2 \rightarrow ArCl^+ + Cl^+ \qquad (6)$$

with an exothermicity of about 13 eV.
Results of our measurements are presented in Fig. 3. It can be seen that this rate constant is of order 1×10^{-9} cm^3s^{-1} what is about 3 times higher than that ones (4×10^{-10} cm^3s^{-1}) measured by I. Kuen with F. Howorka [11] and (2.9×10^{-10} cm^3s^{-1}) by S.G. Lias [4].

Conclusions

We have shown that the N_2^+, Ar^+ and Ar^{++} positive ions react with chlorine Cl_2 very fast and that the corresponding reaction rate coefficients depends on the mean relative kinetic energy KE_{cm}. In the case of the reaction of Ar^+ with Cl_2, its reaction coefficient depends also on the buffer gas. It can imply the enhancement of Cl_2^+ ions during etching of Si in the Ar/Cl_2 mixtures. The reaction of He^+, Ne^+ and Kr^+ with chlorine Cl_2 has been also investigated. The results of these measurements will be published elsewhere [12].

Acknowledgement

This work was supported by the Österreichishes Fonds zur Förderung der Wissenschaftlichen Forschung and by the Scienctific Grant Agency VEGA of Slovakia under projects 1/5184/98 and 1/8314/01.

References

---

[1] F.X. Campos, G.C. Weaver, C.J. Waltman, S.R. Leone: *J. Vac. Sci. Technol. B* **10** (1992) 2217

[2] R.S. Goodman, N. Materer, S.R. Leone: *J. Vac. Sci. Technol. B* **15** (1997) 971
[3] T. Nakano, N. Sadeghi, D.J. Trevor, R.A. Gottscho, R.W. Boswell: *J. Appl. Phys.* **72** (1992) 3384
[4] S.G.Lias: *Int. J. Mass. Spectr. Ion Phys.* **20** (1976) 123
[5] Y. Ikezoe, S. Matsuoka, M. Takebe, A.A. Viggiano : Gas Phase Ion-Molecule Reaction Rate Constants Through 1986 (Mass Spectroscopy Society of Japan, Tokyo, 1987)
[6] V. G. Anicich: *J. Phys Chem. Ref. Data* **22** (1993) 1469
[7] H. Villinger, P. Lukáč, F. Howorka, E. Alge, H. Ramler, W. Lindinger: *Czech. J. Phys.* **B31** (1981) 832
[8] W. Lindinger, E. Alge, H. Störi, R.N. Varney, H. Helm, P. Holzmann, M. Pahl: *Int. J. Mass. Spectrom. Ion Phys.* **30** (1979) 251
[9] G.H. Wannier: *Bell Syst.Techn. J.* **32** (1953) 170
[10] W. Lindinger: *Pure and Appl. Chem.* **57** (1985) 1223
[11] I. Kuen, F. Howorka: *J. Chem. Phys.* **70** (1975) 596
[12] P. Lukáč, W. Lindinger, I.Morva, to be published

Reactions of molecular ions and cluster ions with surfaces

C. Mair[1], Z. Herman[1,2], J. Fedor[3], M. Lezius[1] and T.D. Märk[1,3]

[1] *Institut für Ionenphysik, Leopold-Franzens Universität Innsbruck, Technikerstr. 25, A-6020 Innsbruck, Austria*
[2] *V. Cermak Laboratory, J. Heyrovsky Institute of Physical Chemistry, Academy of Sciences of the Czech Republic, Dolejskova 3, CZ-182 23 Prague 8, Czech Republic*
[3] *Department of Plasma Physics, Comenius University, Mlynska dolina, SK-842 15 Bratislava, Slovak Republic*

Introduction:

Collisions of polyatomic and cluster ions with surfaces provide information about structure, energetics and reactivity of the projectiles. Well defined amounts of energy can be deposited into the scattered ions, the distribution of the excitation energy being relatively narrow. Within the last years especially the study of cluster-ion/surface collisions has attracted the interest of researchers, with the aim to learn about reactions induced within the aggregate, between the aggregate and the substrate or modification of the latter by implantation of clusters.

In addition to being of fundamental importance, reactions of polyatomic molecular ions and cluster ions with surfaces are also relevant to technological applications, such as (i) secondary ion mass spectrometry, (ii) reactive scattering for surface analysis, (iii) surface induced dissociation for structural analysis, (iv) surface modifications for the preparation of novel electronic materials (plasma processing) and (v) plasma-wall interactions in electrical discharges and fusion plasmas.

Experimental:

Experiments were carried out on a tandem mass spectrometer system called BESTOF (B-sector, E-sector, Surface, Time-Of-Flight MS). Neutral clusters are produced in a supersonic expansion source and are ionized by electron impact in a Nier-type ion source. The ions produced are extracted from the ion source region and accelerated to 3 keV for mass (and energy) analysis by a double-focusing two-sector-field mass spectrometer. After passing the mass spectrometer exit slit, the ions are refocused by an Einzel lens and decelerated to the required collision energy before interacting with the target surface. Field penetration effects are minimized by shielding the target with conical shield plates. The incident impact angle of the projectile ions is kept at 45° and the scattering angle (defined as a deflection from the incident beam direction) is fixed at 91°. The collision energy of ions impacting on the surface is defined by the potential difference between the ion source and the surface. The potential difference (hence, the collision energy) can be varied from about zero to about 2 keV with a typical resolution of about 200 meV (full width at half maximum). The collision energy and a measure of the projectile beam energy spread was measured by applying to the target a retarding potential and measuring the (reflected) total ion signal as a function of the target potential. A fraction of the product ions formed at the surface exits the shielded chamber through a 1 mm diameter orifice. The ions are then subjected to a pulsed extraction-and-acceleration field which initiates the time-of-flight analysis of the ions. The second mass analyzer is a linear time-of-flight mass selector with a flight tube of about 80 cm length. The mass selected ions are detected by a double-stage multi-channelplate which is connected to a multi-channel scaler (time resolution of 5 ns per channel) and a laboratory computer.

Results:

In experiments on the surface collisions of acetonitrile molecular cations, both, simple dissociations of the projectile ion and chemical reactions involving H-atom transfer from the surface material (followed by dissociations of the protonated projectile ion formed) were observed. Results obtained for the dimer ions $(CD_3CN)_2^+$ indicate the formation of the protonated acetonitrile ions via surface-induced reactions in two ways: (i) an intra-cluster ion-molecule reaction followed by dissociation to form CD_3CND^+, and (b) a hydrogen pick-up reaction from the surface material during the interaction of the dimer ion with the surface leading to CD_3CNH^+. A simple model based on the Brauman double-well potential, suggested earlier to explain the occurrence of analogous reactions in acetone cluster ion - surface interactions, accounts well for the formation of both products. Considerable amounts of non-dissociated dimer ions were observed after acetonitrile dimer cation -surface collisions with energies up to 25 eV. Similarly, both trimer ions (up to 20 eV) and dimer ions (up to 30 eV) were observed in acetonitrile trimer cation - surface interactions. This indicates that unimolecular dissociation kinetics governs the product formation for these cluster ion- surface interactions.

The second system investigated in the frame of the present work deals with the collisions of ethanol monomer cations ($C_2H_5OH^+$) as well as protonated ethanol monomer, dimer and trimer cations, $(C_2H_5OH)_nH^+$ (n = 1-3), with a stainless steel surface covered by several monolayers of hydrocarbons. While we studied the interaction of ethanol molecular cations in the first line to determine the amount of translational energy transferred into internal degrees of freedom upon the collision process, secondary ion mass spectra obtained after surface collisions of protonated ethanol monomer and cluster cations gave evidence of the unimolecular decomposition of surface excited cluster ions via the sequential loss of monomeric units. Breakdown pattern of molecular ions without a neutral precursor were derived for the first time.

Acknowledgement

Partial support of this work by FWF, Wien, Austria, by the Socrates/Erasmus Programme (J.F.), by the Grant No. 203/00/0632 of the Grant Agency of the Czech Republic, by the Slovak-Austria Cooperation Program in Science and Technology (No. 25s19), and by the Czech-Austria Cooperation Program in Science and Technology (Kontakt 2000-06) is gratefully acknowledged.

Electron and Photon Impact Studies of CF_3I

N.J. Mason, S. Eden, P. Limão Vieira, P. Kendall, S. Pathak, A. Dawes and P. Tegeder,

Department of Physics and Astronomy, University College London, Gower Street, London, WC1E 6BT, United Kingdom

M. Kitajima, M. Okamoto, and H.Tanaka

Department of Physics, Sophia University, Chyoicho 7-1, Chiyoda-ku, Tokyo 102-8854, Japan

S. Samukawa

Si System Research Laboratories, NEC Corporation,
34 Miyukigaoka, Tsukuba, Ibaragi 305-8501, Japan

H. Cho

Department of Physics, Chungnam National University, Taejon, Korea

and

S. Hoffmann

Institute of Storage Rings, University of Aarhus, Ny Munkgade, Aarhus, Denmark

1. Introduction

In the manufacture of ultra-large-scale-integrated circuits, it is necessary to fabricate predetermined patterns on a scale of less than 0.1 μm and fine structures with an aspect ratio of more than 10 on a silicon wafers with diameters of greater 30 cm. This process requires a well collimated, spatially uniform, high density plasma source operating under low pressure conditions The main feed gases used by the plasma etching industry are perfluorocarbons (CF_4, C_2F_6, C_3F_8, CHF_3, and c-C_4F_8) however these are also strong greenhouse gases and therefore, under the terms of the Kyoto Protocol, must be replaced by alternative compounds that have low 'global warming potentials' [1]. One possible replacement is CF_3I, which due to its high photolysis rate, is expected to have a very short lifetime in the atmosphere. CF_3I is also predicted to be able to produce high yields of CF_3 radical in any etching plasma since it should be possible to break the weak C-I bond by direct electron impact.

Prior to adapting existing industrial plasma reactors to use CF_3I as a feed gas it is necessary to run simulations of the reactant plasma, such simulations require a detailed database of the electron interactions with the feed gases (and their dissociation products). However at present there is a lack of data on electron interactions CF_3I. Thus we have performed an exhaustive series of measurements to measure elastic and inelastic scattering from CF_3I including an exhaustive study of its electronic state spectroscopy using both photon absorption and electron scattering techniques.

2. Experimental

Two experimental methods were used in these investigations: electron energy loss spectroscopy (EELS) and photo-absorption spectroscopy. Electron scattering experiments were performed both at University College London and Sophia University Tokyo. Measurements of the angular dependence of any discrete electron scattering process were made by studying the intensity of the scattered electron signal at one specific energy loss and at fixed impact energy. In order to study resonances, the analyser was tuned to transmit only electrons corresponding to a specific energy-loss channel and the count rate measured as a function of impact energy. Absolute cross sections were obtained using the well known relative flow technique using helium as the comparison gas.

The photo-absorption spectra were recorded using synchrotron radiation at both the ultraviolet vacuum line (UV1) of the Astrid facility at Aarhus University, Denmark and on beam line 3.1 at the UK Daresbury synchrotron facility. In addition, temperature dependent measurements at long wavelengths were made using the Molecular Structure Facility at the UK Rutherford Appleton laboratory. Absolute photo-absorption cross sections were derived using the Beer-Lambert law:

$$I = I_0 \exp(-n\sigma x) \qquad (1)$$

where n is the target gas number density, σ is the absorption cross section, and x is the path length.

The CF_3I gas was purchased from Argo international for the European experiments and from Takachiho Chemicals Co. Ltd for the experiments performed in Japan all gases were quoted to have a purity of greater than 99.999%.

3. RESULTS

3.1 Elastic scattering and vibrational excitation

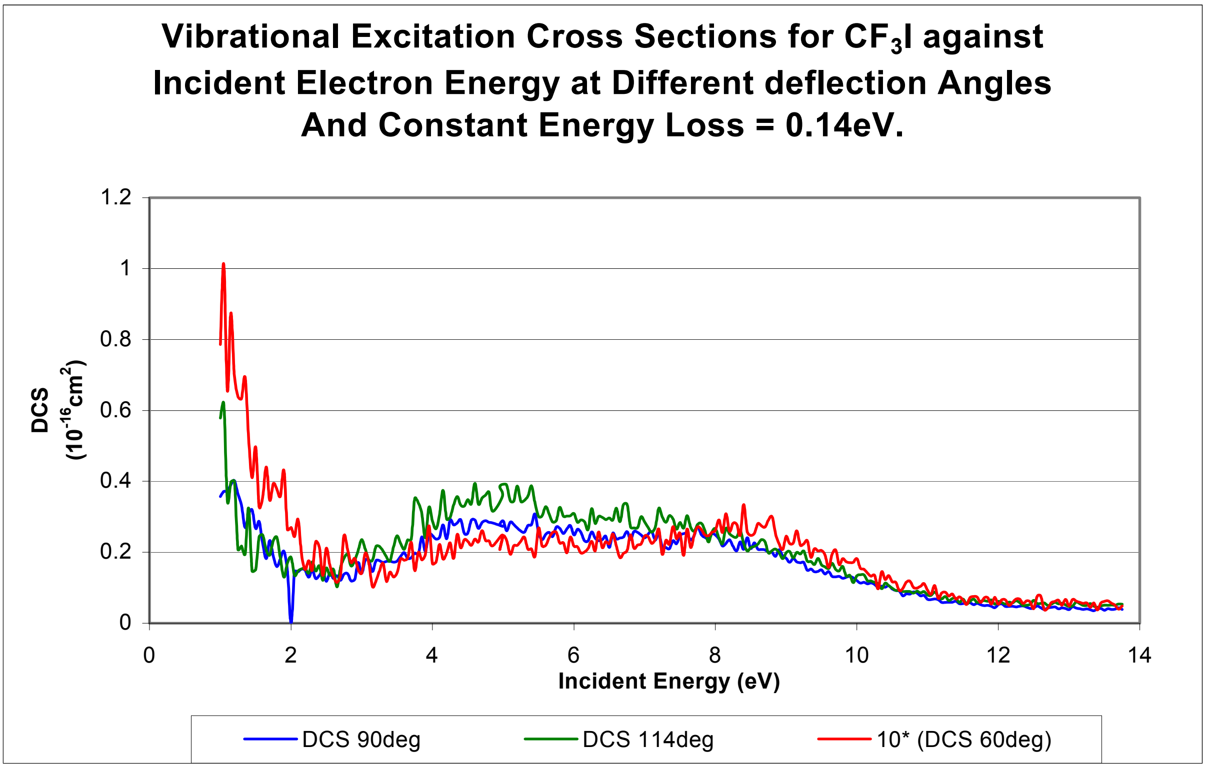

Figure 1:

A comprehensive set of differential cross sections for elastic scattering CF_3I over the impact energy region from 1.5 to 60eV for scattering angles between 20° and 130° has been compiled. These will be presented at the conference. At low incident energies (< 6 eV) a steep increase in the cross section is observed at small scattering angles which may be attributed to the large permanent dipole-moment of CF_3I. As the energy increases from 6 to 8 eV, a new structure emerges around 90°. This energy region corresponds to the position of a shape resonance observed in alkanes and fluoroalkanes.

To probe the formation of temporary negative ions (resonances) in electron scattering, the vibrational excitation function for the 0.14 eV energy-loss peak (mainly the CF_3 stretching modes) was measured. This is shown in Figure 1. Below 4 eV there is a steep increase in cross section and above this energy there are some overlapping structures, i.e. a peak at 5.5 eV, a shoulder at 8 eV, and a long tail up to 12 eV. These provide evidence for the presence of shape resonances associated with the composed symmetry of a_1 (C-Fσ^*) and e (C-Iπ^*) MO's.

3.2 Electronic state spectroscopy

Photo-absorption cross sections measured by both photon impact and electron energy loss spectroscopy between 4 eV (300 nm) and 11.6 eV (110 nm) areown in figure 2. Electron energy-loss spectroscopy provides an alternative methodology for probing the excited states of atoms and molecules. At large scattering angles and low incident energies forbidden transitions dominate the observed Electron Energy Loss Spectrum (EELS) while at small scattering angles and high incident energies allowed transitions are dominant [2]. At electron energies in excess of 100 eV and scattering angle of zero degrees, EEL spectra may be directly compared to photo-absorption results, giving cross sectional data free of any saturation or pressure effects. We have used this technique to explore the photo-absorption cross section of CF_3I above 11 eV, the cut off of the optical window in the synchrotron experiments.

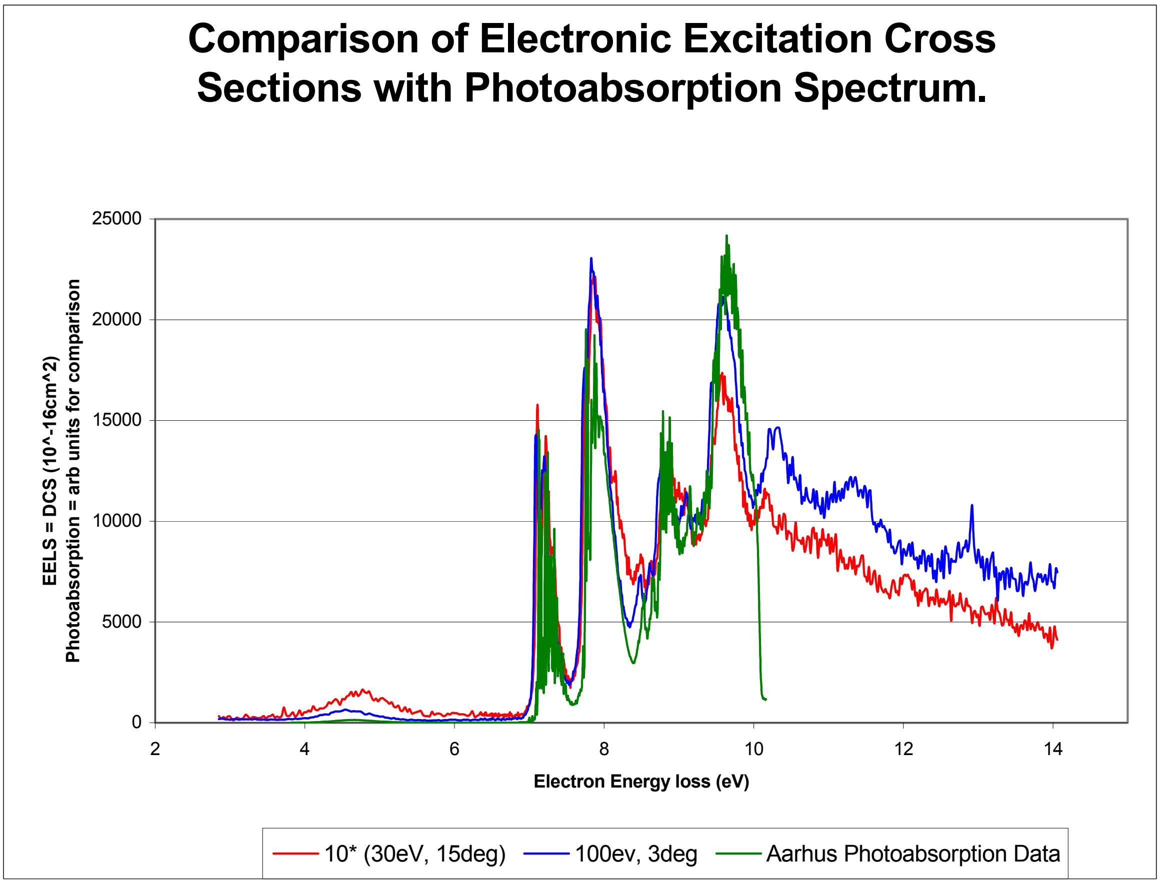

Figure 2:

The photo-absorption spectrum is characterized by three distinct regions. The first region is a very weak continuum around centered about 4.7 eV. The second consists of four prominent band structures observed at around 7.4, 8.1, 9.0, and 9.8 eV, respectively and contains vibrational structure from 7 to 10 eV. The third region (above the ionisation potential) could only be studied by using EELS and shows additional broad peaks. The lowest band is more enhanced at lower incident electron energies suggesting that forbidden transitions are important in this region of the spectrum, while the next four bands show greater differential cross sections at higher incident energies, a trend characteristic of optically allowed transitions.

The broad and weak continuous X → A absorption feature centered at 4.66 eV (266 nm) with a local maximum cross section of 0.67 Mb is a result of the excitation to an antibonding orbital along the C – I bond (n → σ*) of the CF_3I molecule. This band has been assigned to transitions from the ground X state to the excited A state of the CF_3I molecule. Special attention has been devoted to A band (350-200 nm) excitation due to the prompt dissociation along the C-I bond caused by the strong *repulsive nature* of the excited state. Dissociation into a ground state (fluorinated)-alkyl radical (CF_3) and a ground-state I (= I ($^2P_{2/3}$)) or excited-state I^* (= I ($^2P_{1/2}$)) provides a source of radicals for etching silicon wafers in industrial plasma reactors. Absolute photo-absorption cross sections for the A band have been reported in two earlier experiments [3,4] but disagree in the magnitude of the cross section. The present synchrotron results agree well with the data of Fahr et al [3] while the MSF data match the results of Rattigan and Cox [4]. Further details on the classification of higher lying excited states of CF_3I will be presented at the meeting.

References

---

[1] S Samukawa and Mukai 1999 *J. Vac Sci. Technol.* A**17** 5

[2] M Allan, J A Davis and N J Mason 1996 *J. Chem. Phys* **105** 5665.

[3] A Fahr, A K Nayak and R Huie 1995 *J. Geophys. Res.* **199** 275 .

[4] O V Rattigan, D E Dudley and R A Cox 1997 *J. Chem. Soc. Faraday Trans.* **93(16)** 2839.

MICRA : A mobile FTICR mass spectrometer based on a permanent magnet

G. Mauclaire, P. Boissel, M. Heninger, J. Lemaire, P. Maitre

Laboratoire de Chimie Physique, Université Paris-Sud, 91405 Orsay France

Performances of a new, compact, easy to move and operate FTICR ion-trap/mass spectrometer will be discussed.

Combining successfully mobility with the FTICR high mass resolution and powerful ion manipulation techniques opens up new fields of application, in particular when on-line or *in-situ* measurements are necessary.

Experiments where trapped ions must be irradiated with intense photon fluxes from a large scale non movable facility (like a Free Electron Laser) are planned, with emphasis on ion structure determination in the gas phase via IR multi-photon excitation/dissociation as a function of wavelength.

A selected ion flow tube investigation of the positive ion chemistry of a number of bromine containing fully and partially halogenated hydrocarbons

Chris A. Mayhew[a], **Richard Thomas**[a], **and Peter Watts**[b]

[a]*School of Physics and Astronomy, University of Birmingham, Edgbaston, Birmingham B15 2TT, UK,* [b] *RSG Consulting, Salisbury, Wiltshire SP5 1SP, UK*

The reactions of ions with neutral molecules play a significant, and often dominant, role in the chemistry of many gaseous plasma environments, including the interstellar medium, planetary ionospheres and industrial plasmas. This has led to many publications reporting ion-molecule reaction rate coefficients and reaction pathways (product ion distributions). Such critical data are invaluable in the understanding of the formation and abundance of ions and neutral molecules present in natural and man-made plasmas, and to predict how such plasmas chemically and physically evolve.

There have been many studies investigating the positive ion chemistry of chlorofluorocarbons (CFCs) [1], and a number of studies have explored the positive ion chemistry of their replacements, the perfluorocarbons (PFCs) [2-5]. In part these studies have been undertaken because of their relevance to plasmas, and of more specific interest in terms of their relevance to industrial plasma processing. Halogenated molecules are commonly used in plasma processes. In contrast to fluorinated and/or chlorinated species, little attention has been directed to the reactions of positive ions with bromine containing molecules. Yet a systematic study of these reactions permits useful comparison with the ion chemistry of fully and partially fluorinated/chlorinated compounds. This in turn improves our fundamental understanding of ion-molecule reactions, and ultimately leads, for example, to better models to predict the optimum conditions needed to operate industrial plasma processes.

In this paper the thermal bimolecular rate coefficients and product ion branching ratios for the reactions of the positive ions (in order of increasing recombination energy) H_2O^+, N_2O^+, O^+, CO_2^+, CO^+, N^+, and N_2^+ with the bromine containing molecules CF_3Br, CF_2Br_2, $CFBr_3$, CF_2BrCl, $CFBr_2Cl$, $CBrCl_3$, CH_3Br, CH_2Br_2, CH_2FBr, CHF_2Br, $CHFBr_2$, CH_2BrCl, $CHBrCl_2$, $CHBr_2Cl$, CF_3CF_2Br, and CF_2BrCF_2Br at 300 K are reported. This represents the most comprehensive investigation of the positive ion chemistry of brominated molecules to date, with nearly all of the experimental data being presented here for the first time. Only the reactions of H_2O^+ with CF_3Br [6, 7], and O^+ with CHF_2Br [8] have been previously reported. Related to this study is a recent study by Španel and Smith [9], who report the reaction rate coefficients and product ion distributions for the reactions of NO^+ and O_2^+ with CH_3Br and CH_3CH_2Br. Also reported in this paper are the reactions of H_2O^+ with CH_3CH_2Br, CH_2BrCH_2Cl, and CH_2BrCH_2Br. All the reactions are efficient, with all the experimental reaction rate coefficients being greater than 10^{-9} cm^3 molecule^{-1} s^{-1}. Dissociative charge transfer is considered to be the dominant reaction mechanism.

Acknowledgements

We are grateful to the Technological Plasmas Initiative Program, EPSRC, (Grant Reference: GR/L82083) for the financial support of this study.

References

[1] Y. Ikezoe, S. Matsuoka, M. Takebe, and A. Viggiano, *Gas Phase Ion-Molecule Reaction Rate Coefficients Through 1986*, Ion Reaction Research Group, The Mass Spectroscopy Society of Japan.

[2] R. A. Morris, T. M. Miller, A. A. Viggiano, J. F. Paulson, S. Solomon, and G. J. Reid, *J. Geophys. Res.* **100 D** (1995) 1287.

[3] R. A. Morris, A. A. Viggiano, S. T. Arnold, and J. F. Paulson, *Int. J. Mass Spectrom. Ion Processes* **148-151** (1995) 287.

[4] G. Jarvis, C. A. Mayhew and R. P. Tuckett, *J. Phys. Chem. A.* **100** (1996) 17166.

[5] G. K. Jarvis, R. A. Kennedy, C. A. Mayhew, and R. P. Tuckett, *International Journal of Mass Spectrom. Ion Processes* **202** (2000) 323.

[6] R. A. Morris, A. A. Viggiano, J. M. Van Doren, and J. F. Paulson, *J. Phys. Chem.* **96** (1992) 3051.

[7] R. D. Thomas, R. A. Kennedy, C. A. Mayhew, and P. Watts, *J. Phys, Chem. A.* **101** (1997) 8489.

[8] R. A. Morris, A. A. Viggiano, S. T. Arnold, J. F. Paulson, and J. F. Liebman, *J. Phys. Chem.* **99** (1995) 5992.

[9] P. Španel and D. Smith, *Int. J. Mass Spectrom.* **189** (1999) 213.

Investigation on the Spoiling of Meat Using PTR-MS

D. Mayr [a], R. Margesin [b], F. Schinner [b], T.D. Märk [a]

[a] *Institut für Ionenphysik, Universität Innsbruck, Technikerstraße 25, 6020 Innsbruck, Austria*
[b] *Institut für Mikrobiologie, Universität Innsbruck, Technikerstraße 25, 6020 Innsbruck, Austria*

1. Abstract

We investigated the spoiling of meat. Beef (pork) were wrapped into different kinds of packages (air and vacuum) and stored at 4 °C for 10 (13) days. We measured the emitted volatile organic compounds (VOCs) in the course of time and found a large increase in these emissions after a few days of storage. Also a large difference in the spoiling behavior between vacuum- and air- packed meat was observed.

2. Introduction

The preservation of appearance and quality is essential during the distribution and merchandising of perishable products like raw meat. The only criterion consumers have at the point of purchase to select meat cuts is visual appearance. Retail appearance is influenced by numerous factors, including species and muscle of origin, duration of aging, display lighting, temperature (1) and numbers of microorganisms (2).

The principal function of preservative packaging is to delay biodeterioration by restricting the growth of spoilage microorganisms, but to be commercially useful abiotic deterioration must also be controlled – like preservation of the meat color. Delaying the bacterial spoilage of raw meat requires good hygienic condition of the product and low storage temperatures as well as the use of preservative packaging. Under aerobic conditions, the dominant spoilage microorganisms are strictly aerobic pseudomonads. They produce offensive byproducts that cause putrid odors and flavors. Under vacuum, the anaerobic conditions prevent growth of the pseudomonads, the microflora is composed mainly of lactobacilli. If the initial numbers of spoilage bacteria are small, meat will be spoiled slowly by the relatively innocuous byproducts of lactic bacteria. Storage at low temperatures results in reduced growth of spoilage bacteria (3).

The method currently used for determining the status of meat, with respect to spoilage, is analysis of the counts of total bacteria and/or specific spoilage bacteria. An obvious drawback with a bacteriological method is the incubation period of 1-2 days that is required for colony formation. For enrichment cultures several days are needed.

In the present work we have measured the concentrations of several “spoiling compounds” in the headspace air of different kinds of meat that was stored at 4 °C. We compared beef and pork as well as the effect of different kinds of packaging (normal air and vacuum). The goal of these investigations is to replace the time-consuming bacteriological method by fast headspace air measurements to facilitate the investigation of a huge number of meat samples in very short time and to determine the remaining shelf-life of meat during storage from the emissions.

3. Experimental

The measurements were performed using a Proton-Transfer-Reaction-Mass-Spectrometer (PTR-MS) system that allows for on-line monitoring of the concentrations of volatile organic compounds (VOCs). The system and measuring procedure has been described in detail in Refs. (4) and (5). The meat samples (about 15 g) were placed in a glass flask (300 ml) that was incubated at 25 °C. The headspace air was drawn at 114 ml/min by a vacuum pump, 14 ml/min of which was led through a heated teflon transfer line into the PTR-MS system for on-line analysis. The mass spectrometric data were collected for m = 20–260 amu.

The meat samples were all cut from the same piece of meat, and each of them was separately packed and stored at 4 °C in a refrigerator. The emissions of 22 pork samples packed in normal air were measured one by one in the course of 13 days. Seventeen beef samples packed in normal air and 16 beef samples packed in vacuum were investigated in the same way for 10 days. An additional experiment was to measure the VOCs of vacuum-packed beef that was exposed to air after unpacking and incubated for 2 days at 25 °C after a storage time of 6.4 days at 4 °C.

4. Results

In a first set of measurements we investigated the emissions of the pork samples in the course of time. Typical spoiling compounds (6) detected on mass 89 (ethylacetate, methylpropionate, propylformate) are shown in Fig. 1. The concentrations started to exponentially increase after 3.5 days. After about 6 days the concentrations remained more or less unchanged. This behavior of the emitted VOCs corresponds to a typical bacterial growth curve. An initial lag phase where the bacteria get used to the medium components is followed by an exponential increase in the bacterial biomass. After reaching a maximum, a stationary phase is obtained for a certain time before the number of bacteria decreases. We noticed the same trend in the emitted concentrations of many compounds like those shown in Fig 1. Therefore, we conclude that bacteria produce these components.

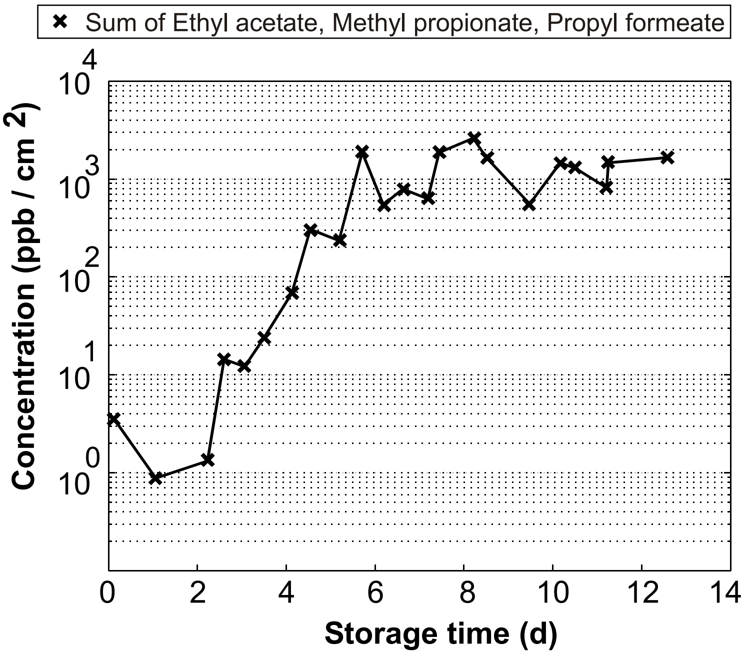

Fig. 1: Concentration of typical spoiling compounds emitted by pork pieces that were stored at 4 °C for 13 days.

In a second set of measurements we compared the VOCs emitted by beef under aerobic (normal packed) and anaerobic (vacuum-packed) conditions. The results are shown in Fig. 2 A. While the typical spoiling compounds ethylacetate, methylpropionate and propylformate (C3-esters) strongly increased with time in the case of the normal air-packed beef, the vacuum-packed beef showed a strong increase of ethanol. That confirms what we expected. Under anaerobic conditions (vacuum) mainly heterofermentative lactic bacteria are metabolically active and produce ethanol beside of lactic acid.

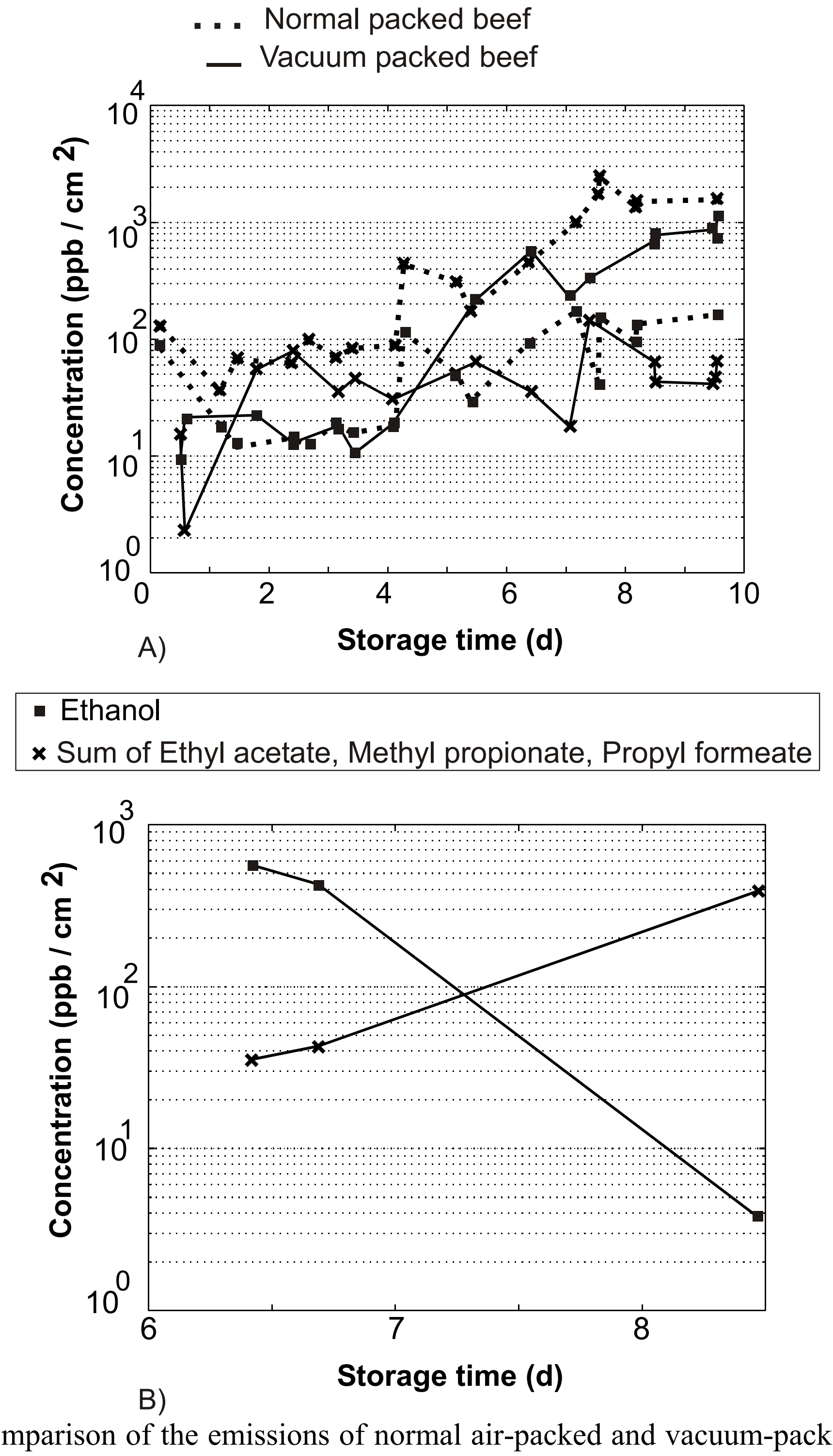

Fig. 2: A) Comparison of the emissions of normal air-packed and vacuum-packed beef in the course of time: The C3-esters (ethylacetate, methylpropionate, propylformate) are typical spoiling compounds emitted under aerobic conditions (normal air packed beef), and ethanol is typically emitted under anaerobic conditions (vacuum-packed beef). B) A vacuum-packed beef sample was stored after a first measurement (storage time = 6.4 d at 4°C) unwrapped in an open glass flask for 2 days at 25 °C, and emissions were measured 6.5 and 49.25 h after the first measurement. Ethanol, the typical spoiling compound emitted by vacuum-packed meat, strongly decreased and the C3-esters increased.

We measured also the VOCs of beef that was initially vacuum packed, stored for 6.4 days at 4 °C, afterwards unwrapped and exposed to air for 2 days at 25 °C. What we can see in Fig. 2 B is that the ethanol concentration was strongly decreasing while the concentration of the C3-esters was increasing. It seems that aerobic bacteria (producing C3-esters) replaced the lactic bacteria (producing ethanol) with time. However, lactic acid bacteria can grow under aerobic conditions but stop ethanol production.

Moreover, the present results indicate, that the emissions of pork and beef under aerobic conditions (normal air packed) are quite similar.

5. Conclusion

In the present work we have found that the time dependence of some VOCs emitted by spoiling meat seems to be comparable to a bacterial growth curve. We have shown big differences in the emissions of normal air- and vacuum-packed meat, which result from different bacteria living under aerobic and anaerobic conditions.

Encouraged by these results we will repeat the measurements and additionally we will carry out a bacteriological examination at the same time. The aim of these experiments is to replace bacteriological examination by fast measurements of the VOC concentrations in the headspace air of the meat sample to facilitate the investigation of a huge number of pieces of meat in very short time and to determine the maximum storage time and storage temperature from the emissions. One also could use this method to investigate the growth of bacteria or the changes in the microbial composition.

6. Acknowledgement

The authors are grateful to Anton Mölk (head of the M-Preis, Innsbruck) by supporting this study in providing us with the meat samples. This work is dedicated to Prof. Dr. W. Lindinger who always urged us to do such measurements. This work was supported by the Austrian "Fonds zur Förderung der wissenschaftlichen Forschung".

7. References

---

[1] L. E. Jeremiah, *Food Res. Int.* 34 (2001) 749-772.
[2] M. Al-Bachir, A. Mehio, *Food Chem.* 75 (2001) 169-175.
[3] C. O. Gill, *Meat Sci.* 43 (1996) 99-109.
[4] W. Lindinger, A. Hansel, A. Jordan, *Int. J. Mass Spectrom. Ion Processes* 173 (1998) 191-241.
[5] A. Hansel, A. Jordan, R. Holzinger, P. Prazeller, W. Vogel, W. Lindinger, *Int. J. Mass Spectrom. Ion Processes* 149/150 (1995) 609-619.
[6] R. A. Edwards, R. H. Dainty & C. M. Hibbard, *J. Appl. Bacteriol.* 62 (1987) 403-412.

Destruction of Bacillus Subtilis Cells Using an Atmospheric-Pressure Dielectric Capillary Electrode Discharge Plasma

N.S. Panikov[1], S. Paduraru[1], R. Crowe[2], P.J. Ricatto[2], C. Christodoulatos[3], and K. Becker[4]

[1] *Department of Chemistry and Chemical Biology, Stevens Institute of Technology, Hoboken, NJ 07030, USA*

[2] *PlasmaSol Corporation, Hoboken, NJ 07030, USA*

[3] *Department of Civil, Ocean, and Environmental Engineering, Stevens Institute of Technology, Hoboken, NJ 07030, USA*

[4] *Department of Physics and Engineering Physics, Stevens Institute of Technology, Hoboken, NJ 07030, USA*

ABSTRACT

We report the results of experiments aimed at the investigation of the destruction of spore-forming bacteria, which are believed to be among the most resistant microorganisms, using a novel atmospheric-pressure dielectric capillary electrode discharge plasma. Various well-characterized cultures of Bacillus subtilis were prepared, subjected to atmospheric-pressure plasma jets emanating from a plasma shower reactor operated either in He or in air (N_2/O_2 mixture) at various power levels and exposure times, and analyzed after plasma treatment. Reductions in colony-forming units ranged from 10^4 (He plasma) to 10^8 (air plasma) for plasma exposure times of less than 10 minutes.

I. Introduction

The interaction of plasmas with chemical and biological agents, in particular in the context of sterilization and decontamination has received much attention in recent years [1-5]. Particular emphasis has been on the utilization of atmospheric-pressure plasmas as they do not require operation in costly vacuum enclosures and thus facilitate the convenient and low-cost treatment of large surface areas. However, atmospheric-pressure discharge plasmas are highly susceptible to instabilities and the generation and reliable maintenance of uniform, large-volume discharge plasmas at or near atmospheric pressure remain formidable challenges. A new concept to generate and maintain atmospheric-pressure plasmas over a wide range of operating conditions was developed at Stevens Institute of Technology [6,7]. The atmospheric-pressure plasma is produced using a patented capillary dielectric electrode discharge concept [7] that employs dielectric capillaries that cover one or both electrodes of the discharge reactor. The capillaries serve as plasma sources, which produce jets of high-intensity plasma at atmospheric pressure in a variety of carrier gases under the right operating conditions.

Spore-forming bacteria, in particular bacteria of the genera Bacillus, are believed to be among the most resistant microorganisms. The species Bacillus subtilis has received particular attention, as these bacteria are easy to grow in a reproducible fashion under chemically well-defined conditions. As a result, Bacillus subtilis has been the species of choice in many sterilization experiments in the past (see e.g. Refs. [8] and [9] and references therein to earlier work). Reliable and reproducible experimental data on sterilization rates have been obtained by different investigators using a variety of methods and can readily be compared.

In this paper, we report the results of experiments aimed at the quantitative determination of the destruction of spore-forming bacteria using a novel atmospheric-pressure plasma shower reactor [6,7]. We established a straightforward protocol to prepare and characterize various bacteria including Bacillus subtilis on either glass or aluminum surface supports and analyze the samples after treatment by atmospheric-pressure plasma jets emanating from the plasma reactor using either in He or air (N_2/O_2 mixture) as a carrier gas at varying power levels and exposure times. We found significant reductions in colony-forming units ranging from 10^4 (He plasma) to 10^8 (air plasma) for plasma exposure times of less than 10 minutes.

II. Experimental Details

II.1 The Atmospheric-Pressure Capillary Electrode Plasma

The atmospheric-pressure plasma jets are produced using a patented capillary dielectric electrode discharge concept [6,7], which employs dielectric capillaries that cover one or both electrodes of the discharge reactor (see fig. 1). The capillaries produce jets of high-intensity plasma at atmospheric pressure under the right operating conditions. The plasma jets emerge from the end of the capillary and form a “plasma electrode” for the main discharge plasma. Under the right combination of capillary geometry, dielectric material, and exciting electric field, a steady state can be achieved. In the present study we used PlasmaSol’s patented system [10] either with pure He, air (N_2/O_2 mixture), or a combination thereof as a carrier gas. The plasma jets emanating from the plasma source were fired against well-characterized cultures placed either on glass or aluminum substrates. In the course of this work we determined both the cell kill rate of the microorganism caused by the plasma exposure as well as the removal of the residual biomass from the respective substrate (cleaning).

Fig. 1: Schematic diagram of the Plasma Reactor.

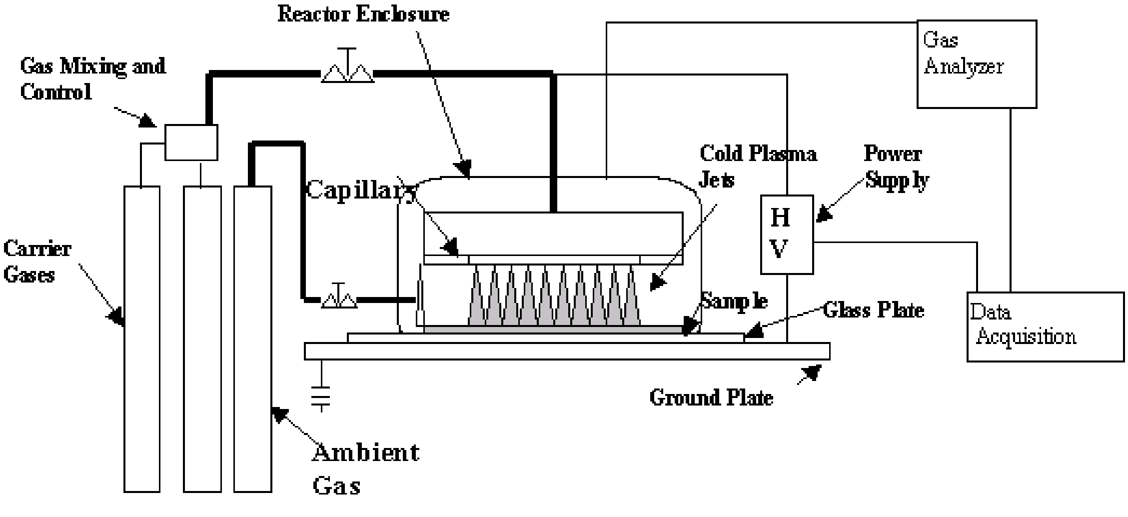

II.2 Characteristics of the Micro-organisms

We used several Bacillus subtilis strains as prototypical examples of spore-forming bacteria. In some cases, we also used non-spore-forming bacteria (Pseudomonas fluorescens ATCC 1474) for selected experiments. The growth kinetics of the selected bacteria as well as the cultivation conditions that were used in the present work has been described previously [11,12]. The bacteria were sub-cultured on Difco nutrient broth slants. The spore suspensions were obtained from homogeneous batch cultures grown on chemically defined media.

III.3 Sample Preparation and Analysis

The protocol for the preparation of the samples for plasma treatment and for establishing reliable bacterial counts after the plasma treatment consists of the following steps:

(i) 100 µl of the stock spore suspension was distributed evenly across a standard microscope slide within an area of 22 x 50 mm^2 and air-dried in a laminar-flow hood. This resulted in an essentially continuous monolayer of biofilm on the slide with patches of bare glass (total surface coverage in the range from 70% to 80%). Alternatively, the suspension (200 µl in this case) was placed on aluminum substrates in an area of 50 x 50 mm^2.

(ii) The samples were then exposed to various plasma treatments.

(iii) After the plasma treatment the biomass was removed from the glass/aluminum substrate by dispensing a small amount of Tween 80 solution on the surface, removing the wet biofilm from the substrate surface, and placing it in a Petri dish. This procedure was repeated until most bacterial mass was removed from the substrate as determined by optical density measurements of the bacterial count on the substrates using direct microscopy. We routinely achieved removal rates of up to (and in some cases exceeding) 90%.

(iv) The resulting cell suspension was transferred from the Petri dish into a test tube and sonicated to disrupt cell aggregates before carrying out the following analytical steps:

- determination of the concentration of colony forming units (CFUs) by plating
- determination of the viability of cells by micro cultivation on agar films [13]
- determination of the viability of cells by staining and direct microscopy [14,15]
- determination of the total amount of solid mass and released nucleic acid by UV/VIS spectrophotometry
- determination of the total number of residual active cells by respirometry measurements

III. Results and Discussion

In a first step, we measured the UV/VIS absorption spectrum of the spore suspension before and after several minutes of plasma treatment. The UV absorption spectrum of a suspension of Bacillus subtilis shows an increase in the absorption of the plasma-treated sample below 300 nm with a local maximum around 260 nm. This is attributed to the presence of extra-cellular compounds that are released during the plasma treatment, most likely DNA, RNA, and proteins and thus indicates the destruction of the cell by the plasma. However, the increased absorption provides only a qualitative measure of the cell kill rate.

A more quantitative measure of the efficiency of the plasma treatment on the destruction of the bacteria is the rate constant, k, for cell destruction (the so-called cell "kill" rate). The kill rate k is determined from a series of experiments in which samples are exposed to the plasma for varying periods of time (under otherwise constant plasma operating conditions) and the number of destroyed cells is plotted versus the plasma exposure time. The CFU number per ml solution plotted as a function of exposure time, y(t) follows an exponential law of the form

$$(1) \qquad y(t) = y_0 \cdot e^{-(k\,t)}$$

where y_0 denotes the initial cell density at t = 0 and k is the cell kill rate. When plotted on a semi-log scale, the data fall on a straight line whose slope allows the determination of "k". It is often more convenient to introduce a cell half-life, $t_{1/2}$, which is defined as $t_{1/2} = \ln(2)/k$ and denotes the time required to destroy half the cell population for a given plasma treatment.

The cell half-life is a particularly useful quantity when one needs to determine the required plasma exposure to achieve a pre-determined sterilization rate, e.g. a cell destruction of 4 orders of magnitude (i.e. by a factor of 10,000). With our plasma shower reactor operating in air as the carrier gas, which is of particular utility in many practical applications, we achieved cell kill rates of up to 1.6 min^{-1} for glass samples corresponding to a cell half-life of $t_{1/2} = 0.43$ min and a plasma exposure time of a little more than 5 min for a cell destruction by a factor of 10,000.

Lastly, we also used the plasma shower reactor with He as a carrier case to treat both air-dried biofilms of spores and vegetative cells and bacterial suspensions on aluminum samples. Because it is in principle more difficult to generate and maintain atmospheric-pressure plasma jets that fire against a conducting substrate (as opposed to firing against the insulating glass substrate), we had to work with lower plasma currents (and consequently with lower plasma densities) in the experiments that used the aluminum substrates. As a result, we obtained lower cell kill rates under these circumstances of about 0.1 min^{-1}.

Acknowledgments

This work was supported by a NASA-SBIR Phase I award to PlasmaSol. We would also like to acknowledge partial financial support from the National Science Foundation.

References

---

[1] M. Laroussi, *IEEE Trans. Plasma Sci.* **24** (1996) 1188

[2] H.W. Hermann, I. Henins, J. Park, and G.S. Salwyn, *Phys. Plasmas* **6** (1999) 2284

[3] M. Laroussi, I. Alexeff, and W.L. Kang, *IEEE Trans. Plasma Sci.* **28** (2000) 184

[4] D.A. Mendis, M. Rosenberg, and F. Azam, *IEEE Trans. Plasma Sci.* **28** (2000) 1304

[5] N.M. Efremov, B.Y. Adamiak, V.I. Blochin, S.J. Dadashev, K.I. Dimitiev, O. Gryaznova, and V.F. Jubashev, *IEEE Trans. Plasma Sci.* **28** (2000) 238

[6] E.E. Kunhardt, *IEEE Trans. Plasma Sci.* **28**, (2000) 189

[7] E.E. Kunhardt and K. Becker, US Patent Nos. 5 872 426, 6 005 349, and 6 147 452

[8] C.L. Nelson and T.J. Berger, *Curr. Microbiol.* **18** (1989) 275

[9] S. Moreau, M. Moisan, M. Tabrizian, J. Barbeau, J. Pelletier, AS. Ricard, and L'H. Yahia, *J. Appl. Phys.* **88** (2000) 1166

[10] Plasmasol, Patents Pending

[11] A.G. Dorofeyev, J.M. Bazin, J.M. Lynch, and N.S. Panikov, *Microbiology* **143** (1997) 1605

[12] N.S. Panikov, "Microbial Growth Kinetics", Chapman and Hall, London (1995)

[13] J.R. Postgate, *Adv. Microb. Physiol.* **1** (1967) 1

[14] J.L. Ingraham and C.A. Ingraham, "Introduction to Microbiology", Brooks/Cole, Thomson Learning (2000)

[15] D. Rickwood and J.R. Harris, "Cell Biology: Essential Techniques", J. Wiley, New York (1996)

Binding Energies of cluster ions

R. Parajuli, S. Matt, O. Echt[1], A. Stamatovic[2], P. Scheier, T.D. Märk[3]

Institut für Ionenphysik, Leopold Franzens Innsbruck, Technikerstr. 25,
A-6020 Innsbruck, Austria

[1] *Guest Professor, permanent address: Department of Physics, University of New Hampshire, Durham NH 03824, U.S.A.*

[2] *Guest Professor, permanent address: Faculty of Physics, P.O. Box 638, Yu-11001 Beograd, Yugoslavia.*

[3] *Also adjunct professor at: Kaytedra fyziky plazmy, Univerzita, Mlynska dolina F2, SK-84248 Bratislava, Slovak Republic.*

1. Introduction

The evolution of crystalline structure in small elemental clusters, and the convergence of their binding energy towards the bulk value, have been central topics in cluster science. Neutral inert gas clusters have served as model systems because the low computational power that was available decades ago restricted searches for the minimum energy structure to systems with pair-wise additive interaction potentials [1, 2]. Early mass spectrometric analysis of xenon clusters [3] revealed intriguing qualitative agreement with computational work, but it was soon realized that those mass spectra revealed properties of charged, rather than neutral, clusters [4, 5]. The binding energy of charged clusters may be measured by analyzing the kinetic energy released in the metastable decay of mass selected parent ions. In the present work we use finite heat bath theory to determine the binding energies of argon, neon, krypton, oxygen and nitrogen clusters from their respective average kinetic energy releases.

2. Experimental

Details of the experimental arrangement have been published elsewhere [6]. In brief, the apparatus consists of a high-resolution double focusing two-sector field mass spectrometer of reversed Nier-Johnson type geometry. The clusters are produced by expanding the gas from a stagnation chamber with a pressure of about 1-10 bar through a nozzle (diameter 10 μm or 20 μm) into a vacuum of about 10^{-7} torr. The ensuing neutral clusters are ionised by an electron beam of variable energy and current. The cluster ions are then extracted by an electric field and accelerated by 3 kV into the spectrometer. They pass through the first field free region, are then momentum-analyzed by a magnetic sector field, enter a second field-free region (length 33.3 cm), pass through a 90° electric sector field and are finally detected by a channeltron.

MIKE (mass-analyzed ion kinetic energy) spectra are measured to investigate decay reactions of mass-selected ions [7]. Spectra are recorded as follows: The magnet is tuned to the mass of the parent ion, m_p, while the electrostatic sector field voltage U is scanned. Stable singly charged ions will have a kinetic energy of 3 keV and pass at the nominal sector field voltage of U_p = 510 V. Daughter ions (mass m_d), formed in the 2ff in a spontaneous decay reaction, will then pass at a voltage

$$U_d = \frac{m_d}{m_p} U_p \tag{1}$$

This equation relates the position of a daughter ion peak to the position of the parent ion peak in a MIKE spectrum. In practice, the parent ion peak will have a finite width and a distinct shape that will also be imposed on the daughter ion peak. If no kinetic energy were released in the decay reaction, the daughter ion peak would have the same shape as the parent ion peak, only scaled by the ratio of the electric sector field voltages U_d/U_p. However, any kinetic energy release (KER) in the reaction will modify the peak shape of the daughter ion. If the MIKE peak is strictly Gaussian, then the average kinetic energy can be extracted from its full-width-at-half-maximum, ΔU, from the width of the daughter ion ΔU has to be corrected for the finite width of the parent ion by deconvoluting the fragment ion signal with the parent ion signal.

$$< KER >= \frac{z_2^2 m_1^2 U_{acc}}{16 z_1 m_2 m_3} \left(\frac{\Delta U}{U_p} \right)^2 x2.16 \qquad (2)$$

Gaussian peaks are observed when the decaying ensemble is (i) prepared in a way that the internal energy is equally partitioned over all degrees of freedom and (ii) no reverse activation barrier prevents the production of ions with low kinetic energies. The cluster ions are produced with a distribution of internal energies in the ion source, but only a distinct sub-ensemble of these ions will decay in the experimental time window of about 20 to 60 µs which we sample by the MIKE scan technique, depending on the mass of the selected cluster ion. At this time the excess energy is uniformly distributed among all degrees of freedom and thus we can model the decay reactions with statistical theories. Details of the data analysis have been presented elsewhere [8].

3. Results and discussion

The smallest cluster ion for which we observe here statistical driven metastable monomer evaporation is five. The shape of the metastable peaks observed in this work is Gaussian hence the average kinetic energy release in the center-of-mass system <KER> is extracted from the width of the peaks with help of eq. 2. Given the KER and the fact that the KER distributions are Gaussian we can apply finite heat bath theory to derive the transition state temperatures and the dissociation energies of the cluster ions, (for details see Ref. [8-13]).

In Fig.1 we show as an example binding energy values for neon, argon and krypton cluster ions. The solid dots are derived by using a constant Gspann factor of $\gamma = 23.5$. Also shown (as a solid line slightly above the solid dots) are binding energies obtained with a more carefully chosen, size-dependent Gspann factor. The latter binding energies are 10 to 15 % larger than the former, depending on cluster size n and monomer mass. The corresponding deviations in the Gspann factor from the commonly accepted value of $\gamma = 23.5$ [11] are smaller, but they exceed the uncertainty of 6 % that Klots had suggested for γ for small and medium-sized clusters, for a variety of different systems and $k = 10^5$ s^{-1} [12]. Hence, the common practice of using a constant Gspann factor for different cluster sizes, monomer masses and mass spectrometers is questionable.

Included in Fig. 1 are binding energies of argon cluster ions recently measured in our lab [13]. The reader is referred to that report for a comparison with experimental results obtained by Stace and co-workers [14,15], and for a detailed comparison with Engelking's alternative procedure [16] to derive binding energies from average KER values.

For the inert gases Ne, Ar and Kr, the binding energies initially decrease with increasing size n and then level off at a value above the enthalpy of vaporization of the condensed phase [17] which is indicated in Fig. 1 as a solid horizontal line. Beyond this general decrease, there are no features that are common to all three systems. The local variations for larger cluster sizes are probably statistical. It should be noted, though, that neither the geometric structure of small inert gas cluster ions nor the size dependence of their stabilities are expected to follow a common trend. For example, the size distributions observed after electron impact ionization of neutral clusters are notably different in this size range [18-21]. Experiments and computations at various levels of sophistication suggest that the structure of the ionic core may well be different for neon, argon, krypton and xenon cluster ions [22-27]. Results for calculated binding energies (Ne [27] and Ar [24]) are designated by the dotted lines in Fig. 1.

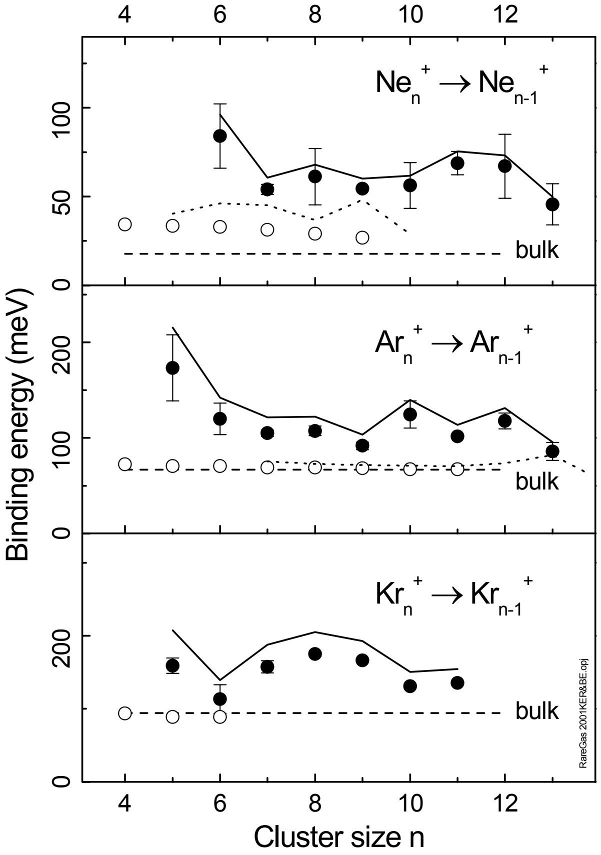

Fig.1: Full dots: Binding energies of Ne, Ar and Kr cluster ions calculated from the average KER with finite heat bath theory and a constant Gspann factor of γ = 23.5. Solid line: Same, but with a more appropriate, size-dependent Gspann factor. Open dots: Results from high-pressure gas phase experiments [28]. Dashed horizontal line: Enthalpy of vaporization of the bulk [17]. Dotted lines: Binding energies calculated for Ne_n^+ [27] and Ar_n^+ [24].

Also shown in Fig. 1 are thermochemical stabilities (ΔH^o values, open dots) determined by Hiraoka and Mori from van't Hoff plots of ionic clustering equilibria in a high-pressure mass spectrometer source [28]. These values are significantly below the values obtained by us. However, as pointed out by Klots [12], these measurements are subject to systematic errors which arise from evaporation of cluster ions before mass analysis is accomplished.

We have applied the same method in order to measure kinetic energy release for decaying N_2 and O_2 clusters ions and derived binding energies from the kinetic energy release data of these metastable decay reactions. Both, average kinetic energy release <KER> data derived from the peak shapes and the time dependence of the metastable fractions of stoichionmetric oxygen cluster ions show a characteristic dependence on cluster size (U-shape) indicating a change in the metastable fragmentation mechanism when going from the dimer to the dekamer ion. The binding energy results obtained are in fair agreement with previous results based on gas phase ion equilibria measurements and the corresponding bulk value.

Acknowledgment

Work partly supported by the Österreichischer Fond zur Förderung der wissenschaftlichen Forschung, Wien, Austria. The research is a part of the European Commission 5th Framework Program ”Delayed ionization and competing cooling mechanisms in atomic clusters” (Cluster Cooling, HPRN-CT-2000-00026). R.P. likes to acknowledge financial support by the ÖAD, Innsbruck through a Eine Welt stipend and likes to thank the Tribhuvan University, Kathmandu, for granting a study leave.

References

[1] J. K. Lee, J. A. Barker, F. F. Abraham, *J. Chem. Phys.* **58** (1973) 3166.
[2] M. R. Hoare, *Adv. Chem. Phys.* **40** (1979) 49.
[3] O. Echt, K. Sattler, E. Recknagel, *Phys. Rev. Lett.* **47** (1981) 1121.
[4] J. M. Soler, J. J. Saenz, N. Garcia, O. Echt, *Chem. Phys. Lett.* **109** (1984) 71.
[5] H. Haberland, *Surf. Sci.* **156** (1985) 305.
[6] S. Matt, M. Sonderegger, R. David, O. Echt, P. Scheier, J. Laskin, C. Lifshitz, T. D. Märk, *Int. J. Mass Spectrom. Ion Proc.* **187** (1999) 813.
[7] R. G. Cooks, J. H. Beynon, R. M. Caprioli, G. R. Lester, *Metastable Ions* (Elsevier, Amsterdam, 1973).
[8] S. Matt, M. Sonderegger, R. David, O. Echt, P. Scheier, J. Laskin, C. Lifshitz, T.D. Märk, *Chem. Phys. Lett.* **303** (1999) 379.
[9] C. Lifshitz and F. Louage, *Int. J. Mass Spectrom. Ion Proc.* **101** (1990) 101.
[10] C. E. Klots, *J. Phys. Chem.* **92** (1988) 5864.
[11] C. E. Klots, *Z. Phys. D* **20** (1991) 105.
[12] C. E. Klots, *Int. J. Mass Spectrom.* **100** (1990) 457.
[13] R. Parajuli, S. Matt, O. Echt, A. Stamatovic, P. Scheier, T. D. Märk, *Eur. Phys. J. D* **16** (2001) 69.
[14] A. J. Stace, *J. Chem. Phys.* **85** (1986) 5774.
[15] C. A. Woodward, A. J. Stace, *J. Chem. Phys.* **94** (1991) 4234.
[16] P. C. Engelking, *J. Chem. Phys.* **87** (1987) 936.
[17] D. R. Lide, *CRC Handbook of Chemistry and Physics* (CRC Press, Boca Raton, 2000).
[18] T. D. Märk, P. Scheier, *Chem. Phys. Lett.* **137** (1987) 245.
[19] A. Ding, J. Hesslich, *Chem. Phys. Lett.* **94** (1983) 54.
[20] I. A. Harris, R. S. Kidwell, J. A. Northby, *Phys. Rev. Lett.* **53** (1984) 2390.
[21] W. Miehle, O. Kandler, T. Leisner, O. Echt, *J. Chem. Phys.* **91** (1989) 5940.
[22] P. J. Kuntz, J. Valldorf, *Z. Phys. D* **8** (1988) 195.
[23] M. Amarouche, G. Durand, J. P. Malrieu, *J. Chem. Phys.* **88** (1988) 1010.
[24] H. U. Böhmer, S. D. Peyerimhoff, *Z. Phys. D* **11** (1989) 239.
[25] J. A. Smith, N. Gotts, J. F. Winkel, R. Hallett, C. A. Woodward, J. A. Stace, B. J. Whitaker, *J. Chem. Phys.* **97** (1992) 397.
[26] B. Von Issendorff, A. Hofmann, H. Haberland, *J. Chem. Phys.* **111** (1999) 2513.
[27] F. A. Gianturco, F. Sebastianelli, *Eur. Phys. J. D* **10** (2000) 399; F. A. Gianturco, E. Yurtsever, F. Sebastianelli, *Int.J.Mass Spectr.*, in print (2002)
[28] K. Hiraoka, T. Mori, *J. Chem. Phys*. **92** (1990) 4408.

Low energy electron interaction with HCOOH and CH_3NO_2

Andrzej Pelc, Wolfgang Sailer, Herwig Drexel, Paul Scheier, Tilmann D. Märk

Institute of Ion Physics, University of Innsbruck, Technikerstrasse 25, 6020 Innsbruck, Austria

Here we report experimental results of low energy, ~ 0 – 10 eV, electron attachment to formic acid (HCOOH) and nitromethane (CH_3NO_2). In case of formic acid we observe $HCOO^-$, OH^-, O^- anions whereas electron capture to nitromethane forms NO_2^-, O^-, OH^-, CN^-, CNO^-. For the above mentioned ions, absolute cross sections for electron dissociative attachment were obtained.

Formic acid is the simplest organic acid and is an important prototype molecule. It is closely related to the possible building blocks of biomolecules so that its properties are of direct interest for radioastronomy and for exobiology studies. Presence of HCOOH in the space has spurred the study of this molecule [1,2].

Nitromethane is the simplest and typical organic nitro compound. It can plays a role in atmospheric chemistry following reaction of CH_3 radicals with oxides of nitrogen. Nitromethane is also important because of its potential use as propellant. CH_3NO_2 is polar molecule with unusually large dipole moment (3.5 D) and there is considerable interest to study formation and structure of dipole bounds anions [3,4].

In order to measure a accurate attachment cross sections a highly monochromatic electron beam is needed. This high energy resolution beam is provided (in our experiments) by a trochoidal electron monochromator (TEM).

In a TEM the electrons are produced by thermal emission from a hairpin filament. An electron beam is then formed by a system of three electrodes and enters the dispersion volume consisting of a homogeneous crossed electric and magnetic field. In this region slow electrons are deflected more strongly than faster ones. Using an exit aperture with a diameter of 0.4 mm, electrons with a narrow energy spread are selected from the dispersed beam and these electrons are accelerated or decelerated by a system of two lenses to the desired energy. After passing through the interaction chamber the remaining electrons are collected and measured by a Faraday cup. A pair of Helmholtz coils mounted outside of the apparatus produces the magnetic field necessary for the operation of the TEM. By adjusting the magnetic field and the electrostatic potentials of the electrodes the electron energy spread and the electron current can be varied in a wide range. Nevertheless, these two parameters depend on each other and cannot be adjusted independently. Ions formed in the interaction chamber are extracted towards the quadrupole mass spectrometer by a very weak electric field. After mass analysis, the negative ions are detected in a channeltron coupled to a computer data acquisition and analysis system. The molecular beam is formed by effusion through a 20 μm diameter orifice.

One of the great advantages of a TEM is that the electrons are guided by a magnetic field. This is especially important for low energy electrons to avoid space charge and to minimize influence of stray magnetic fields (e.g. Earth magnetic field). Additionally the magnetic field helps to separate electrons and negative ions in the interaction chamber, thus electrons, which otherwise would case artefacts in the anion signals, are not extracted by the ion extraction field.

Using a recently improved version of the TEM [5,6] we are able to produce electron beams with spreads in the electron energy of about 30-50 meV (full width half maximum - FWHM). To determine the energy spread and for calibration of the energy scale we used measured cross sections for of Cl^- or SF_6^- produced by dissociative electron attachment to CCl_4 or SF_6, respectively.

In the present experiments the electron energy spread (FWHM) used was 140 meV in case of HCOOH and 150 meV in nitromethane. This low resolution was a reasonable compromise between product ion intensity and incident electron energy distribution. For the calibration of the energy scale we used the Cl^- /CCl_4 system. Samples of 98% (HCOOH) and 99% (CH_3NO_2) pure were purchased from Sigma Aldrich, Wien, Austria. The experiments have been performed at a pressure of about 10^{-6} mbar (HCOOH) and 2×10^{-6} mbar (CH_3NO_2), respectively.

Electron impact with HCOOH in the energy range of ~ 0 – 10 eV produces the three anionic fragments $HCOO^-$, OH^-, O^- (reaction 1a-c) with intensity ratios (maximum peak values) of 240 : 10 : 1,

$e^-(\approx 1.3\text{eV}) \quad + HCOOH \quad \rightarrow HCOO^- \; + H,$ (1a)
$e^-(\approx 7.5\text{ eV}) \quad + HCOOH \quad \rightarrow OH^- \; + HCO,$ (1b)
$e^-(\approx 7.5\text{ or }9.2) \quad + HCOOH \quad \rightarrow O^- \; + HCOH.$ (1c)

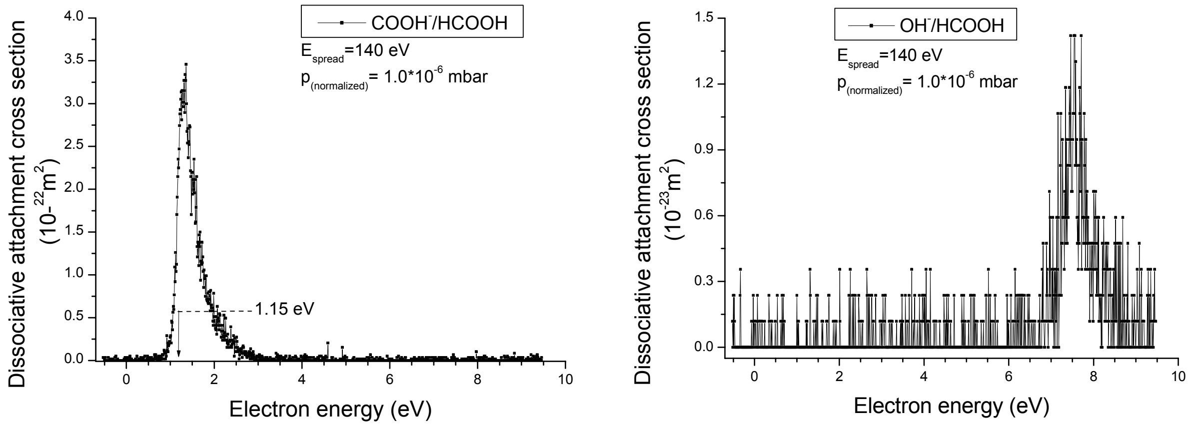

a)

b)

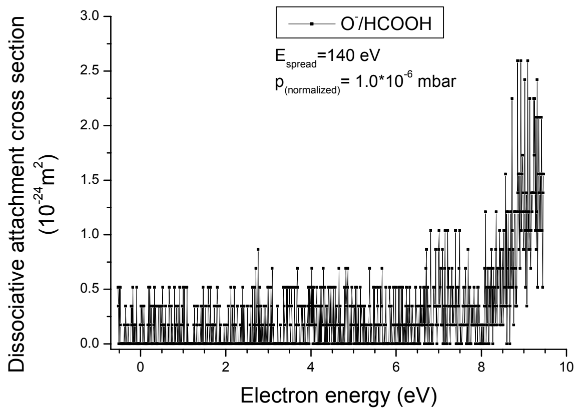

Fig. 1. Formation of negative ions by dissociative electron attachment to formic acid. The pressure in the apparatus was 10^{-6} mbar and the electron energy spread was about 140 meV
a) $HCOO^-$/HCOOH
b) OH^-/HCOOH
c) O^-/HCOOH).

c)

These anions are formed through different channels at electron energies of about 1.3, 7.2, 7.5 and 9.2 eV, respectively. In case of $HCOO^-$ generation we observed vertical onset at 1.15 eV. This experimentally determined onset value does not agree good with a value of 1.30 ± 0.13 derived from the difference between the bond dissociation energy D(HCOO-H) = 4.47 eV (calculated from enthalpy of formation [7]) and the electron affinity EA(HCOO) = 3.17 ± 0.13 eV [7].

Based on earlier measurements of dissociative cross section of Cl^-/CCl_4 [8,9] we obtained estimates for the absolute cross sections for fragments in free electron attachment to the HCOOH molecule (Fig. 1).

In case of electron attachment to nitromethane we observe formation of five fragment ions: NO_2^-, O^-, OH^-, CN^-, CNO^- with an ion current intensity ratio of 100 : 10 : 2 : 1.5 : 1. In a complex molecule such as nitromethane, each ion observed may occur at more than one electron energy. The negative ion signals showed maxima at incident electron energy of about 0, 0.7, 2, 4.3, 5.6 and 8.7 eV. These anions are produced via the following reactions:

$$e^-(\approx 0, 0.7) + CH_3NO_2 \rightarrow NO_2^- + CH_3, \quad (2a)$$
$$e^-(\approx 5.6, 4.3, 8.7) + CH_3NO_2 \rightarrow O^- + CH_3NO, \quad (2b)$$
$$e^-(\approx 0, 4.3, 5.6, 8.7) + CH_3NO_2 \rightarrow OH^- + CH_2NO, \quad (2c)$$
$$e^-(\approx 0, \sim 2, 5.6, 8.7) + CH_3NO_2 \rightarrow CNO^- + H_2O + H, \quad (2d)$$
$$e^-(\approx 0, \sim 2, 4.3, 5.6, 8.7) + CH_3NO_2 \rightarrow CN^- + H_2O + OH. \quad (2e)$$

For these fragment ions produced we also estimated absolute cross section for their formation, the peak value for dominant NO_2^- anion having a value of 5.2×10^{-22} m^2.

Acknowledgements

Work partially supported by FWF and ÖHW, Wien, Austria and European Commission, Brussels.

References

[1] M. Schwell, S.Leach, K. Hottmann, H. W. Jochims, H. Baumgärtel, *Chem. Phys.* **272** (2001) 77
[2] B. W. Walker, L. S. Sunderlin, *Int. J. Mass Spectrom.* **184** (1999) 183
[3] I. C. Walker, M. A. D. Fluendy, *Int. J. Mass Spectrom.* **205** (2001) 171
[4] S. L. Lunt, D. Field, J. P. Ziesel, N. C. Jones, R. J. Gulley, *Int. J. Mass Spectrom.* **205** (2001) 197
[5] V. Grill, H. Drexel, W. Sailer, M. Lezius and T. D. Märk, *Int. J. Mass Spectrom.* **205** (2001) 209
[6] V. Grill, H. Drexel, W. Sailer, M Lezius, T. D. Märk, *J. Mass Spectrom.* **36** (2001) 151
[7] NIST webbook, (webbook.nist.gov)
[8] S. C. Chu, P. D. Burrow, *Chem. Phys. Lett.* **172** (1990) 17
[9] S. Matejcik, G. Senn, P. Scheier, A. Kiendler, A. Stamatovic, T. D. Märk, *J. Chem. Phys.* **107** (1997) 8955

On the separation of enantiomers of 1,1,1,2-Tetrafluoroiodoethane by IR Multiphoton Excitation

Jörg Pochert, Martin Quack, and Georg Seyfang

Physical Chemistry, ETH-Zürich, CH-8093 Zürich, Switzerland

Abstract

We report the first attempt to separate enantiomers of chiral molecules using IR-multiphoton excitation with circularly polarized light. CF_3CHFI has been chosen as its IR-spectroscopy and its IR-photochemistry is well characterized by our previous work. A theoretical model based on a master equation is presented to predict the enantiomeric enrichment factor. Our experimental results show that the experimental sensitivity must be improved to reach the limit of the theoretical prediction.

Introduction

The infrared laser chemistry of chiral molecules is of potential interest for some of the fundamental aspects of molecular chirality [1], including racemization dynamics, the possibility of chiral selection of diastereomers and enantiomers by multiphoton excitation, and the hypothetical influence of the weak nuclear interaction in chemistry. So far, only two classes of chiral compounds have been the subject of detailed studies concerning their infrared laser chemical properties, the chiral sulfoxides [2], and the (mono)fluorooxiranes [3, 4]. Our investigations of sulfoxides proved for the first time [5], that isotopic diastereoisomers can be separated by multiphoton excitation, due to their slightly different vibrational transition frequencies. However, the possibility of enantiomer enrichment by infrared laser radiation has not been investigated previously, mainly because of the difficulties related to highly accurate enantioselective analysis of racemic mixtures of the possible candidates. Now, for the chiral CF_3CHFI these difficulties have been solved, analyzing the racemic mixtures before and after irradiation by means of chiral gas chromatography.

Tetrafluoroiodoethane has many advantages for experimental investigations of IR multiphoton excitation and laser chemistry. Its infrared laser chemistry [6] and spectroscopy were subject to previous studies, including a detailed analysis of the influence of a chiral, symmetry breaking coupling on the infrared spectra of the C–H chromophore [7, 8]. CF_3CHFI contains a strong infrared chromophore moiety (C–F) with an integrated band strength of $G = 2.1$ pm^2. The low threshold energy of $\tilde{E}_T = 18400$ cm^{-1} for the C–I bond fission leads to a simple primary dissociation step in IR-laser chemistry.

Theoretical Model for Enantiomeric Enrichment During IR-Multiphoton Excitation

Our theoretical treatment of the enantiomeric enrichment by infrared multiphoton excitation is based on the vibrational circular dichroism of the pumped chromophore vibration. Irradiation with circularly polarized (CP) light leads to a slightly more efficient excitation of one of the two enantiomers, giving rise to a higher product yield. This effect can be calculated approximately using the master equation [9, 10, 11]. Assuming that the difference in the efficiency of the multiphoton excitation with CP–light for the (R) and (S) enantiomers is essentially determined by their different integrated band strengths $G_{S,R}$, we can apply the master equation with a modified rate coefficient for up–pumping, given by

$$K_{M+1,M} = \frac{CG(1 \pm g/2)I\rho'_M}{\Delta E \rho_M}. \tag{1}$$

where the symbols have been defined previously in [9, 10, 11] and g is the (Kuhn) anisotropy factor [12, 13]

$$g = \frac{\Delta G}{G} = \frac{4R}{D}. \tag{2}$$

ΔG represents the difference between the integrated band strengths of the vibration excited for (R) and (S) enantiomers, irradiated with circularly polarized light. In equation (2) g is furthermore related to the rotatory strength R and the dipole strength D of the vibration [14], molecular quantities which can be measured or calculated ab initio [15, 16, 17]. In equation (1) we assume the approximate validity of the chromophore principle [9, 10, 11] not only for G, but also for g, meaning that both quantities are constant over a wide range of excitation energies.

Enantiomeric enrichment, experiment and theory

To investigate the possibility of chiral selection by infrared multiphoton excitation, we performed experiments irradiating racemic mixtures of tetrafluoroiodoethane with CP–radiation, using the laser lines 9R24 and 9R28 under various experimental conditions. The results are summarized in table 1. Within the experimental accuracy of our analytical method of typically 0.1%, no enantiomeric enrichment could be achieved. Experiments with higher total pressure where collisional deactivation should increase the selectivity because more photons are absorbed until the reaction threshold is reached again gave no significant deviation from the racemic ratio.

$\tilde{\nu}_{exc}$/ cm^{-1}	P_{tot}/ mbar	F/ Jcm^{-2}	N	n	Yield/ %	$\langle(e_1/e_2)\rangle$	$\Delta\langle(e_1/e_2)\rangle$
—	11	—	—	4	—	0.999	0.005
1083.3	11	0.7	8640	4	50	0.998	0.014
1083.3	11	0.5	13500	4	25	1.0032	0.0024
1083.5	11	0.6	23000	4	60	1.004	0.004
1074.7	11	0.7	9000	4	30	1.004	0.007
1074.7	11	0.6	18000	4	30	1.002	0.007
1074.7	11	0.5	37200	4	20	1.007	0.008
1074.7	27	1.4	5600	4	30	0.989	0.04
1074.7	43	1.9	2300	4	50	1.004	0.008
1074.7	17.8	1.1	10670	7	41	1.003	0.013

Table 1: Summary of the experiments on chiral selection of tetrafluoroiodoethane. N, $\tilde{\nu}_{exc}$ and F are the number of multi mode laser pulses, the excitation wavenumber, and the laser fluence in the experiments. P_{tot} is the total pressure (reactant: always $p = 0.5$ mbar CF_3CHFI plus additional N_2), and n is the number of experiments. The first line represents the result of the analysis of the reactant without laser irradiation. For each experiment the reaction yield was determined by IR spectroscopy. The mean enantiomeric ratio $\langle(e_1/e_2)\rangle$ was measured by chiral gas chromatography with the error $\Delta\langle(e_1/e_2)\rangle$ given as 95% confidence interval.

In the simulation a master equation was applied for different values of g and no significant influence from possible nonlinear intensity effects (case C, [10, 11]), even at very low laser intensities ($I < 5\mathrm{MWcm}^{-2}$), was observed. An almost linear dependence of the static yield ratio as a function of the anisotropy factor g is found for different laser fluences. The slope is close to one for all laser fluences. Therefore the effect of chiral selection by multiphoton excitation scales linearly with the anisotropy factor g or the vibrational circular dichroism ΔG:

$$\frac{P_{app}^{R}-1}{P_{app}^{S}-1} \propto g \propto \Delta G \tag{3}$$

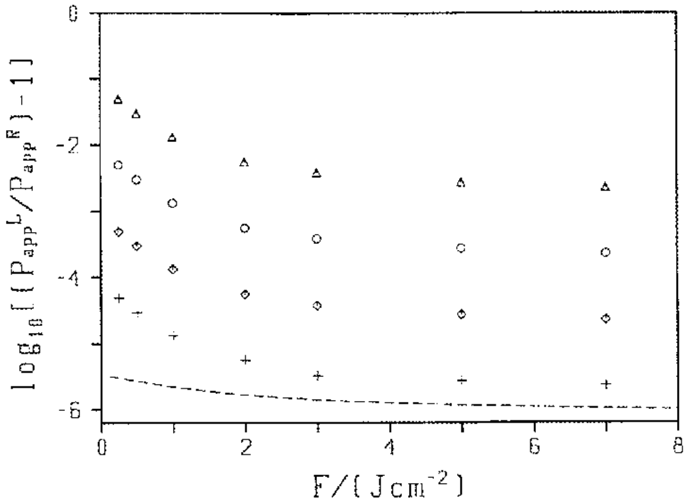

Figure 1: Ratios of apparent yields P_{app}^{R}, P_{app}^{S} in logarithmic scale are given as a function of laser fluence for different values of the anisotropy factor g. (Symbols), g; (△): 4.76·10^{-3}; (o): 4.76·10^{-4}; (◊): 4.76·10^{-5}; (+): 4.76·10^{-6}. The hypothetical single photon selectivity is given as dashed line (g =4.76·10^{-6}).

This finding is consistent with the usual stepwise excitation of the reactant in infrared laser chemistry, whereas for direct absorption of n photons one might expect a scaling with $(\Delta G)^n$. Figure 1 shows the fluence dependence of the static yield ratio for different anisotropy factors. Here, increasing enantiomeric separations are observed for decreasing laser fluences. These data can be compared to the hypothetical single photon case which are shown for the smallest value of g as a broken line in the figure. Concerning chiral selection, single and multiphoton excitation of tetrafluoroiodoethane differ by a factor of 15 for small laser fluences (F = 0.25 Jcm^{-2}). This enhancement is comparable with the number of absorbed IR-photons. For higher laser fluences contributions from the steady state regime are more important and the chiral selection approaches the value for single photon excitation.

To simulate a realistic experiment, we have calculated the vibrational circular dichroism of tetrafluoroiodoethane ab initio. For the ν_{C-F} chromophore vibration a value of $g = 6.75 \cdot 10^{-5}$ was obtained [17]. If one chooses a laser fluence of $F = 0.5$ Jcm^{-2}, one finds that a maximum enantiomeric excess is obtained with the number of laser pulses chosen to be $N_{\max} = 2286$. We then get static yields of $P_{app}^{R} = 1.094069 \cdot 10^{-2}$ and $P_{app}^{S} = 1.093610 \cdot 10^{-2}$. The calculated enantiomeric excess is $ee = 2.1 \cdot 10^{-4}$, one order of magnitude beyond the sensitivity of our experiments using chiral gas chromatography with an uncertainty of about $\Delta ee = 2.5 \cdot 10^{-3}$.

Summary

We have previously determined for the first time hyperfine state selected product distributions in IR–multiphoton excitation with the examples CF_3I, C_6F_5I and CF_3CHFI [6]. Here, several major new results were obtained for the chiral compound CF_3CHFI. A first experiment was performed, resulting in enantiomer separation below the sensitivity of our analytical technique. In principle one can think of increasing the sensitivity, for example by averaging individual gas chromatograms. Parallel to the experiment, enantiomer enrichment was calculated, implementing the vibrational circular dichroism into the statistical theory of multiphoton excitation. The simulation of a realistic experiment, based on the vibrational circular dichroism calculated ab initio revealed that the effect is expected to be below the sensitivity of our current experimental conditions. The calculation points to the fact, that chiral selection in the limit of case B [10] is approximately linear with respect to the number n of photons absorbed. A larger effect would be expected in case C [10], i.e. for a smaller chiral molecule such as fluorooxirane [3, 4].

Acknowledgement

The ab initio calculations of the VCD were performed by Jürgen Stohner. Our work is supported by the Schweizerischer Nationalfonds and the ETH Zürich (including C^4 and CSCS).

References

[1] Martin Quack. *Angew. Chem. Int. Ed. Engl.*, 28:571–586, 1989.

[2] Heike Gross, Yabai He, Martin Quack, Alex Schmid, and Georg Seyfang. *Chem. Phys. Lett.*, 213(1,2):122–130, 1993.

[3] Hans Hollenstein, David Luckhaus, Jörg Pochert, Martin Quack, and Georg Seyfang. *Angew. Chemie Intl. Ed.*, 36(1,2):140–143, 1997.

[4] Tae-Kyu Ha, Jörg Pochert, and Martin Quack. *J. Phys. Chem.*, 102(27):5241, 1998.

[5] Heike Gross, Guido Grassi, and Martin Quack. *Chem. Eur. J.*, 4(3):441–448, 1998.

[6] Y.He, J.Pochert, M.Quack, R. Ranz, and G.Seyfang. *J. Chem. Soc. Faraday Discuss.*, 102:275–300, 1995.

[7] J.Pochert, M.Quack, J.Stohner, M.Willeke. *J. Chem. Phys.*, 113:2719 (2000).

[8] Jörg Pochert and Martin Quack. *Mol. Phys.*, 95:1055–1075, 1998.

[9] M. Quack. Multiphoton excitation. In P. v. Ragué Schleyer, N. Allinger, T. Clark, J. Gasteiger, P. A. Kollman, H. F. Schaefer III, and P. R. Schreiner, editors, *Encyclopedia of Computational Chemistry*, Vol. 3, pages 1775–1791. John Wiley and Sons, (1998).

[10] Martin Quack. *J. Chem. Phys.*, 69(3):1282–1307, 1978.

[11] Martin Quack. *Advances in Chem. Phys.*, 50:395–473, 1982.

[12] E.Charney. *The Molecular Basis of Optical Activity.* John Wiley and Sons, New–York, 1979.

[13] J.A. Shellmann. *Chemical Reviews*, 75(3):323, 1975.

[14] L.A. Nafie and T.H. Walnut. *Chem. Phys. Lett.*, 49(3):441, 1977.

[15] P.J. Stephens and M.A. Lowe. *Annu. Rev. Phys. Chem.*, 36:213, 1985.

[16] P.J. Stephens. *J. Phys. Chem.*, 89:748, 1985.

[17] M. Quack and J. Stohner, *to be published.*

Dissociative Reactions of Hydrogen Molecular Ions H_2^+, D_2^+, HD^+, H_3^+ D_3^+ and HD_2^+ with Graphite and Stainless Steel Surfaces

A. Qayyum, W. Schustereder, C. Mair, Z. Herman[1], W. Hess[2], P. Scheier, T.D. Märk

Institut für Ionenphysik, Leopold-Franzens Universität, A-6020 Innsbruck, Austria

[1] *Inst. of Phys. Chem., Academy of Sciences, Dolejskova 3, CZ-182 23 Praha 8*
[2] *Association Euratom-C.E.A., Cadarache, F-13108 St.Paul-lez-Durance*

1. Introduction:

The importance of molecular hydrogen and small hydrocarbon ions in the edge plasma of tokamaks has only been recognized recently. Previous investigations of some of these molecular ions include photodissociation of H_3^+ [1], neutralization of H_2^+ at metal surfaces [2], scattering of D_2^+ and D_3^+ from Au surface [3] and collision-induced dissociation of HD_2^+ with rare gases [4]. Here we report a first systematic study on the interaction of H_2^+, D_2^+, HD^+, H_3^+ D_3^+ and HD_2^+ ions, in the collision energy range up to 100 eV, with graphite tiles from the tokamak reactor Tore Supra in Cadarache and with a hydrocarbon covered stainless steel surface.

2. Exprimental:

Experiments have been carried out with a tandem mass spectrometer system recently developed in Innsbruck called BESTOF (B-sector, E-sector, Surface, Time-Of-Flight mass spectrometer) [5]. The ions were produced in a newly commissioned commercial Colutron ion source (low-pressure d.c. gas discharge). Ions are extracted from the plasma, accelerated and focused subsequently by a specially designed lens system into the entrance slit of a double focusing two-sector field mass spectrometer. After mass and energy analysis the beam is refocused by an Einzel lens and hits the surface after deceleration to the desired collision energy by an electrostatic lens system. The collision energy is determined by the potential difference between the ion source and the surface and can be varied from about zero up to 2 keV. A fraction of the secondary ions produced in the collision process exits the shielded collision chamber through an orifice, is extracted, accelerated and analyzed in a Time-Of-Flight mass spectrometer.

3. Results and discussion:

The collision energy dependence of intact secondary ions H_2^+ , H_3^+ and their only product ion observed H^+ is shown as a energy resolved mass spectrum in Fig.1. In the case of H_3^+ one needs higher collision energies as compared to H_2^+ to dissociate the molecule, i.e. the fraction of the collision energy transformed into internal energy of the projectile ion in the surface collision process must be higher in the H_3^+ case due to a stronger bonding in this triatomic molecular ion. This is in accordance with the thermochemistry of these ions, i.e., the binding energy of H_3^+ is approx. 1.5 eV larger than that of H_2^+ [6]. This has been confirmed by additional studies with the deuterated species D_2^+ and D_3^+.

Several trends can be deduced from the study of H_2^+, D_2^+ , H_3^+ and D_3^+ ions interacting with graphite and stainless steel surface:

1. Both, the diatomic and the triatomic hydrogen (deuterium) molecular ion fragment exclusively into the atomic counterparts. This is in accordance with results concerning the angular dependence of backscattering of keV molecular ions studied [3].

2. In both cases, hydrogen and deuterium, the fragmentation patterns are very similar for the two target surfaces.
3. In contrast, for both targets the ERMS fragmentation patterns for hydrogen and deuterium ions are quite surprisingly rather different from each other, i.e. shifted approximately by a factor 1.3 (when going from hydrogen to deuterium) and in addition the slopes arround the crossing points (full lines) in the deuterium case are less steep.
4. The threshold values and the crossing point values are higher for the heavier hyrogen molecular ion, i.e., incresing from 26.8 to 29.3 and from 44.3 to 56.5 eV respectively, when going from the H_2^+ to the H_3^+ case. This is in accordance with the somewhat larger binding energy of the H^+ ion in the triatomic ion as compared to the diatomic case. The same is true for the deuterium case, although in this system all values are much higher than in the hydrogen case. It is interesting to note that in the hydrogen case for instance the threshold energies are shifted by about the same order of magnitude as the different binding energy (appr. 2 eV), whereas the crossing point is shifted by a much larger amount (appr. 10 eV).
5. Finally, when the data are converted from an ERMs type plot to a VRMS type plot the ordering in the threshold value and the crossing point value is changing drastically.

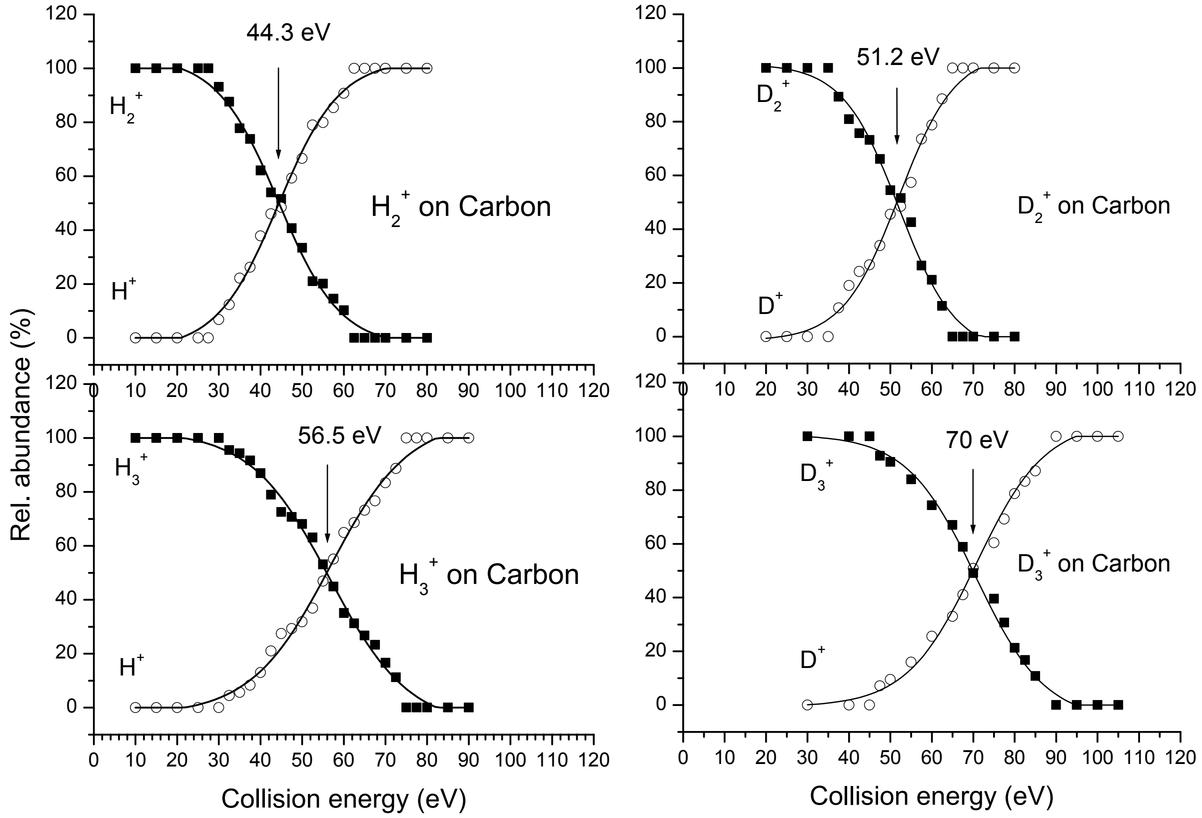

Fig. 1. Energy resolved mass spectra of the H_2^+ , H_3^+ , D_2^+ and D_3^+ interacting with a graphite surface of a Tore Supra tile from Cadarache.

As these studies showed characteristic differences between the two different isotopic species. We have also investigated the interaction of HD^+ and HD_2^+ ions yielding further information on the energetics and dynamics of the break-up patterns for these two ions. A detailed account of this study will be published elsewhere [7].

Acknolegements:

This work has been carried out within the Association EURATOM-ÖAW. It was also partially supported by the FWF and ÖAW, Wien, Austria and by the European Commission, Brussels.

References

---

[1] Alan Carrington and Richard A, Kennedy, *J. Chem. Phys.* **81** (1984) 91.
[2] B. Willerding, W. Heiland and K. J. Snowdon, *Phys. Rev. Lett.* **53** (1984) 2031.
[3] W. Eckstein, H. Verbeek, S. Datz, *Appl. Phys. Lett.* **27** (1975) 527.
[4] I. Alvarez, C. Cisneros, J. de Urquijo and H. Martinez, *Nucl. Instr .Meth, B***53** (1991) 438.
[5] C. Mair, T. Fiegele, F. Biasioli, J. H. Futrell, R. Wörgötter, V. Grill, M. Lezius and T. D. Märk, *Plasma source Sci. Technol.* **8** (1999) 1.
[6] J.L. Franklin, J.G. Dillard, H.M. Rosenstock, J.T. Herron, K. Draxl and F.H. Field, “Ionization potentials, appearance potentials and heats of formation of gaseous positive ions” National bureau of standards U.S.A., NSRDS-NBS 26 (1969).
[7] A. Qayyum, W. Schustereder, C. Mair, Z. Herman, W. Hess, P. Scheier, T.D. Märk, to be published.

Chiral Molecules: Frequencies and Thermodynamic Properties under the Influence of Molecular Parity Violation

Martin Quack and Jürgen Stohner

Laboratorium für Physikalische Chemie - ETH-Zürich (Hönggerberg)
CH 8093 Zürich - Switzerland

Abstract

We report vibrational frequencies for all the fundamentals of CDBrClF as compared to the normal isotopomer CHBrClF already reported at SASP 2000. The parity violating potential energy has been obtained by high quality *ab initio* methods as a function of reduced dimensionless normal coordinates $\vec{q}$ and fitted to a multi-dimensional polynomial expansion. This polynomial has been used to calculate parity-violation induced relative frequency shifts for the fundamentals ω_1 to ω_9 as expectation values using anharmonic vibrational wavefunctions. Anharmonicity can have a magnifying effect on the relative frequency shift as compared to a harmonic approximation. Furthermore, we discuss parity violation in relation to statistical thermodynamic equilibrium properties.

Introduction

More than hundred years ago, van't Hoff [1] pointed out that if one assumes a left-right symmetry of ordinary free space in physics, the heat of formation as well as the entropy of enantiomers are exactly equal. This leads to the conclusion that the equilibrium constant for razemization is exactly equal to one. This fundamental symmetry has not been questioned even when Hund [2] discussed stereomutation tunneling of chiral molecules in quantum mechanical terms and noted that this symmetry leads to a "good" quantum number termed parity. A discussion in a much broader context recognize Hund's considerations as one special case of molecular chirality, namely *de facto* symmetry breaking in the "low barrier" limit [3, 4]: Here, tunneling splitting $\Delta_{\pm}E$ dominates and 'chirality' is very short-lived. Examples are hydrogen peroxide (H_2O_2) and aniline-NHD (C_6H_5NHD) which have been studied by high-resolution infrared spectroscopy as well as computationally [5]. It was found that here chiral states have lifetimes on the order of 10^{-13} to 10^{-11} s. The other fundamental case of molecular chirality, the *de lege* symmetry beaking in the "high barrier" limit with a tunneling splitting much smaller than the parity violating energy difference $\Delta_{\text{pv}}E$ is known in principle since the discovery of parity violation in atomic physics [6, 7] and practically since early quantitative estimates of $\Delta_{\text{pv}}E$ [8, 9]. Progress in computational methodology from early Hartree-Fock [8,9] to high quality ab initio methods using a Multi-Configurational Linear Response (MC-LR) approach [10] identified T_2S_2 [11] and S_2Cl_2 [12] as candidates with important *de lege* symmetry violation. The hamiltonian for parity violating potentials in stable molecules [8, 9, 13–15], which is based on the neutral current for electron-nucleus potentials in a nonrelativistic approximation used in atomic physics, is given by

$$H_{\text{pv}} \approx \frac{G_{\text{F}}}{\sqrt{2}m_{\text{e}}c}\sum_a Q_a \sum_i \left[\vec{p}(i)\cdot\vec{s}(i), \delta^3(\vec{r}(i)-\vec{R}(a))\right]_+ \tag{1}$$

where nuclear spin effects have been neglected. The sums go over nuclei a and electrons i, where m_{e} is the electron mass, c the velocity of light, G_{F}: Fermi-coupling constant, $\vec{p}(i)$: electron momentum, $\vec{s}(i)$: electron spin, $\delta^3(\vec{r}(i)-\vec{R}(a))$: Dirac delta distribution that confines the interaction to the positions of the nuclei, and $[\cdots]_+$ denotes the anti-commutator. The weak charge Q_a is given by $N_a - (1 - 4\sin^2\vartheta_{\mathrm{W}})\, Z_a$ with N_a: neutron number of nucleus a, Z_a: electric nuclear charge, ϑ_{W}: Weinberg angle. This hamiltonian introduces an energy difference between left and right handed molecules, $\Delta_{\mathrm{pv}}E$, and the heat of reaction for stereomutation is [16]

$$\mathrm{S} \quad = \quad \mathrm{R} \qquad\qquad \Delta_{\mathrm{r}}H_0^0 \approx N_{\mathrm{A}}\,\Delta_{\mathrm{pv}}E \tag{2}$$

$\Delta_{\mathrm{pv}}E = 2|E_{\mathrm{pv}}|$ where E_{pv} is the expectation value of H_{pv} with a spin-orbit perturbed ground state wavefunction (for more details, see [10, 13]). ΔE_{pv} might be observable following the proposals in [3, 4]. It has also been discussed on the last SASP 2000 in Folgaria [17] that a less direct route to experimentally determine the influence of parity violation on molecular properties is to try to observe a shift of the vibrational frequencies of enantiomers with respect to each other [18,19]. We have shown [20–22] that the current experimental accuracy still lacks three to four orders of magnitude for the measurement of the relative frequency shift between both enantiomers of CH(D)BrClF in the range of the CF-stretching fundamental at about 1078 cm^{-1}. Figure 1 shows an energy level scheme for (R)-CHBrClF (right) and (S)-CHBrClF (left) with $\Delta_{\mathrm{r}}H_0^0 \approx 2 \times 10^{-11}$ J mol^{-1}.

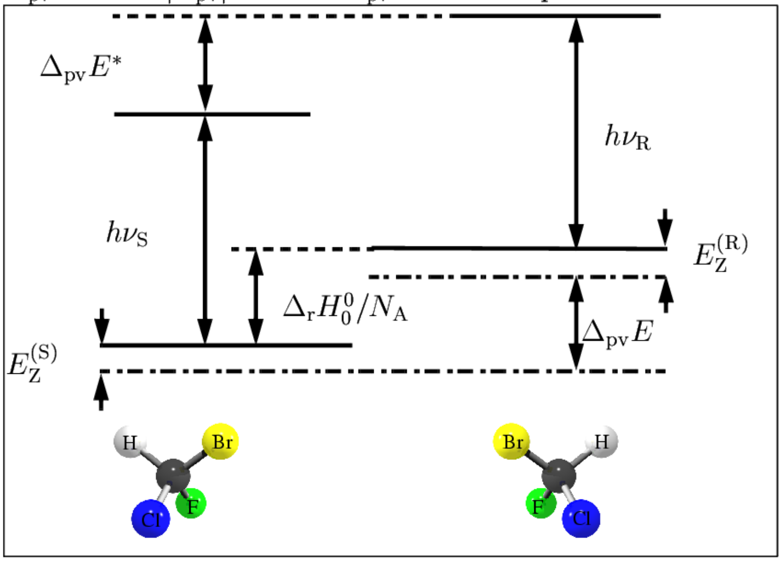

Figure 1: Energy level scheme (not to scale) for the stereomutation of (S)-CHBrClF (left) and (R)-CHBrClF (right).

Theory

The parity violating potential V_{pv} of CHBrClF and CDBrClF has been determined using the RPA and MC-LR CASSCF ab initio method [10] along the reduced dimensionless normal coordinates $\vec{q}$ for all relevant vibrational degrees of freedom. In our early calculations [21,22] we assumed $V_{\mathrm{pv}}(\vec{q})$ diagonal in q_i. $V_{\mathrm{pv}}(\vec{q})$ was then fitted to a polynomial expansion in q_i and the relative frequency shift has been determined analytically in the separable harmonic adiabatic approximation (SHAA) or numerically in the separable anharmonic adiabatic approximation (SAAA) by solving the vibrational Schrödinger equation

$$\begin{aligned} \widehat{H}_{\mathrm{mol}}(\vec{p},\vec{q}) &= \widehat{H}^0_{\mathrm{mol}}(\vec{p},\vec{q}) + V_{\mathrm{pv}}(\vec{q}) && \text{(3a)}\\ E_n &\approx E_n^0 + \langle\Psi_n^0|V_{\mathrm{pv}}(\vec{q})|\Psi_n^0\rangle && \text{(3b)}\\ \Delta_{\mathrm{pv}}E_n &= \left(E_n^{(\mathrm{R})} - E_n^{(\mathrm{R}\,0)}\right) - \left(E_n^{(\mathrm{S})} - E_n^{(\mathrm{S}\,0)}\right) \approx 2\,\langle\Psi_n^0|V_{\mathrm{pv}}(\vec{q})|\Psi_n^0\rangle && \text{(3c)} \end{aligned}$$

$V_{\mathrm{pv}}(\vec{q})$ is expanded in a polynomial of m^{th} order and $\langle\Psi_n^0|V_{\mathrm{pv}}(\vec{q})|\Psi_n^0\rangle$ is evaluated numerically.

$$(\Delta_{\mathrm{pv}}\,\nu^{\mathrm{ul}})/\nu^{\mathrm{ul}} \approx 2\,[\langle\Psi_{\mathrm{u}}^0|\tilde{V}_{\mathrm{pv}}(\vec{q})|\Psi_{\mathrm{u}}^0\rangle - \langle\Psi_{\mathrm{l}}^0|\tilde{V}_{\mathrm{pv}}(\vec{q})|\Psi_{\mathrm{l}}^0\rangle]/\tilde{x}^{\mathrm{ul}} \tag{4}$$

In our current work we consider treatments where both the anharmonic parity conserving Born-Oppenheimer potential for vibrational motion and the parity violating potentials $V_{\mathrm{pv}}(\vec{q})$ contain couplings between several normal modes [23]. $|\Psi_n^0\rangle$ is then the anharmonic eigenfunction to the eigenvalue E_n of the complete vibrational molecular Hamiltonian $\widehat{H}^0_{\mathrm{mol}}$ for the upper (u) or lower (l) molecular state, and $\tilde{x}^{\mathrm{ul}}$ the corresponding energy difference. The factor of 2 in eq. (4) arises from considering the difference between R and S enantiomers, which is twice the individual shift. More details can be found elsewhere [16,21,22]. If the total energy of a molecule is separable in the translational, electronic, vibrational and rotational degrees of freedom, the total partition function is given by the product

$$Q_{\mathrm{tot}} = Q_{\mathrm{trans}} Q_{\mathrm{el}} Q_{\mathrm{vib}} Q_{\mathrm{rot}} \tag{5}$$

(only electronic ground state populated) and the parity violation modifies the individual contributions to Q' [16]. The equilibrium constant $K_{\mathrm{eq}}(T)$ for stereomutation eq. (2) can be written as

$$K_{\mathrm{eq}}(T) = \frac{Q'^{(\mathrm{R})}_{\mathrm{trans}} Q'^{(\mathrm{R})}_{\mathrm{vib}} Q'^{(\mathrm{R})}_{\mathrm{rot}}}{Q'^{(\mathrm{S})}_{\mathrm{trans}} Q'^{(\mathrm{S})}_{\mathrm{vib}} Q'^{(\mathrm{S})}_{\mathrm{rot}}} \exp[-\Delta_{\mathrm{r}} H^0_0 / RT] \approx (1 + x) \cdot (1 + y) \tag{6}$$

Results and Conclusions

The normal coordinate dependence of the parity violating potential has been used to determine relative frequency shifts for all fundamentals and some overtones in CH(D)BrClF in the SHAA and SAAA approximation. The expectation values can also be used for the calculation of temperature dependent equilibrium constants, $K_{\mathrm{eq}}(T)$.

$T = 300$ K	
$Q'^{R}_{\mathrm{vib}}/Q'^{S}_{\mathrm{vib}}$	1.000 000 000 000 000 014 471 568 444 847
$Q'^{R}_{\mathrm{rot}}/Q'^{S}_{\mathrm{rot}}$	0.999 999 999 999 999 967 755 000 000 000
$\exp(-\Delta_{\mathrm{r}} H^0_0/RT)$	0.999 999 999 999 990 880 417 660 488 762
K_{eq}	0.999 999 999 999 990 862 644 228 933 609
$x \approx -1.777\ 343 \times 10^{-17}$	$y \approx -9.119\ 582 \times 10^{-15}$
$T = 4$ K	
$Q'^{R}_{\mathrm{vib}}/Q'^{S}_{\mathrm{vib}}$	1.000 000 000 000 000 000 000 000 000 000
$Q'^{R}_{\mathrm{rot}}/Q'^{S}_{\mathrm{rot}}$	0.999 999 999 999 999 967 755 000 000 000
$\exp(-\Delta_{\mathrm{r}} H^0_0/RT)$	0.999 999 999 999 316 031 324 536 887 904
K_{eq}	0.999 999 999 999 315 999 079 536 887 926
$x \approx -3.224\ 500 \times 10^{-17}$	$y \approx -6.839\ 687 \times 10^{-13}$

In the table we list the ratio of the rotational and vibrational partition functions for (R)- and (S)-CHBrClF, the exponential factor and $K(T)$ for 4 and 300 K. At low temperature, the equilibrium constant K_{eq} is smaller implying that the equilibrium is shifted towards the (S)-CHBrClF, which is also the more stable enantiomer.

References

[1] J. H. van't Hoff, Die Lagerung der Atome im Raume,Vieweg, Braunschweig 1876; in: B.M. Bazendijk (Ed.): La chimie dans l'espace, Rotterdam 1887.

[2] F. Hund, Z. Physik, **43**, 805–826 (1927).

[3] M. Quack, Angew. Chem. Int. Ed. Engl., **28**, 571–586 (1989).

[4] M. Quack, Chem. Phys. Lett., **132**, 147–153 (1986).

[5] B. Fehrensen, D. Luckhaus, and M. Quack, Z. Phys. Chem. N. F., **209**, 1–19 (1999); Chem. Phys. Lett., **300**, 312–320 (1999).

[6] C. S. Wu, E. Ambler, R. W. Hayward, D. D. Hoppes, and R. P. Hudson, Phys. Rev., **105**, 1413–1414 (1957).

[7] T. D. Lee and C. N. Yang, Phys. Rev., **104**, 254–258 (1956).

[8] D. W. Rein, R. A. Hegstrom, and P. G. H. Sandars, Phys. Lett., **A71**, 499 (1979).

[9] R. A. Hegstrom, D. W. Rein, and P. G. H. Sandars, J. Chem. Phys., **73**, 2329–2341 (1980).

[10] R. Berger and M. Quack, J. Chem. Phys., **112**, 3148–3158 (2000).

[11] M. Gottselig, D. Luckhaus, M. Quack, J. Stohner, and M. Willeke, Helv. Chim. Acta, **84**, 1846 (2001).

[12] R. Berger, M. Gottselig, M. Quack, and M. Willeke, Angew. Chem. Int. Ed., **44**, 4195 (2001).

[13] A. Bakasov, T. K. Ha, and M. Quack, J. Chem. Phys., **109**, 7263–7285 (1998).

[14] A. Bakasov, T. K. Ha, and M. Quack. In J. Chela-Flores and F. Rolin, editors, *Proc. of the 4th Trieste Conference (1995), Chemical Evolution: Physics of the Origin and Evolution of Life*, pages 287–296, Dordrecht, (1996). Kluwer Academic Publishers.

[15] A. Barra, J. Robert, and L. Wiesenfeld, Phys. Lett., **A115**, 443–447 (1986).

[16] M. Quack and J. Stohner, Chirality, **13**, 745–753 (2001). (This paper contains a number of misprints to be corrected in M. Quack, J. Stohner, Chirality (to be publ. 2002))

[17] M. Quack and J. Stohner. In *SASP 2000, Proceedings of the XII Symposium on Atomic and Surface Physics and Related Topics* edited by Davide Bassi and Paolo Tosi, Univ. di Trento, Folgaria, Italy, pages PR–11, 1–4, (2000).

[18] C. Daussy, T. Marrel, A. Amy-Klein, C. Nguyen, C. Bordé, and C. Chardonnet, Phys. Rev. Lett., **83**, 1554–1557 (1999).

[19] A. Bauder, A. Beil, D. Luckhaus, F. Müller, and M. Quack, J. Chem. Phys., **106**, 7558–7570 (1997).

[20] J. Stohner, A. Beil, H. Hollenstein, O. Monti, and M. Quack. In *37th IUPAC Congress and 27th GDCh Meeting, Berlin, Germany, August 14-19, 1999, Frontiers in Chemistry: Molecular Basis of the Life Sciences*, page 525. ISBN 3-924763-82-8.

[21] M. Quack and J. Stohner, Phys. Rev. Lett., **84**, 3807–3810 (2000).

[22] M. Quack and J. Stohner, Z. Physik. Chemie, **214**, 675–703 (2000).

[23] A. Beil, H. Hollenstein, O. Monti, M. Quack, and J. Stohner, J. Chem. Phys., **113**, 2701–2718 (2000).

Electron-Driven Neutral Dissociation of Si-Containing Molecules

T. Raynor[1], N. Abramzon[1], K.E. Martus[2], and K. Becker[1]

[1] *Department of Physics, Stevens Institute of Technology, Hoboken, NJ 07030, USA*
[2] *Department of Chemistry and Physics, William Paterson University, Wayne, NJ 07470, USA*

ABSTRACT

A combination of electron scattering and laser-induced fluorescence (LIF) techniques has been used in the experimental determination of the absolute cross section for the formation of Si(^{1}S) and Si(^{1}D) ground-state atoms following the neutral molecular dissociation of Si-containing molecules such as SiH_4 and SiF_4 by electron impact. Electron impact on Si-containing molecules produces - among other species - Si(^{1}S) ground-state atoms which are detected by pumping the Si $(3p)^2\ ^1S \rightarrow (3p)(4s)\ ^1P$ transition at 390 nm with a tunable dye laser and recording the subsequent Si $(3p)(4s)\ ^1P \rightarrow (3p)^2\ ^1D$ fluorescence at 288 nm. Likewise, Si(^{1}D) ground state atoms can be detected by interchanging the pump and probe pathways in the above reaction sequence.

1. Introduction

The collisional interaction of an electron (or any other projectile) with a molecule may result in the dissociation of that molecule. Molecular dissociation induced by electron impact may lead to the formation of neutral ground-state fragments (neutral molecular dissociation) or may combine with other inelastic electron scattering processes resulting in dissociative excitation, dissociative ionization, and dissociative attachment. The electron impact dissociation of a molecule is not only one of the most important fundamental collisional interactions between an electron and a molecule, but dissociation processes also play an important role in many applications including gas discharges, low-temperature processing plasmas, fusion edge plasmas, gas lasers, planetary, cometary and stellar atmospheres, and radiation chemistry [1-3]. While electron impact dissociation processes have been studied extensively since the early years of this century, the focus of most experimental studies has been on dissociative excitation, dissociative ionization, and dissociative attachment processes [1,2]. This is due to the fact that in these processes the resultant dissociation products are formed with internal energy and/or charge that can be used conveniently for their quantitative detection. By contrast, neutral molecular dissociation results in two or more neutral ground-state fragments which are very difficult to detect. Rigorous quantum mechanical descriptions of molecular dissociation processes are also very difficult because of the complexity of both the target and the process. However, first results of the application of variational methods to the electron-impact dissociation of molecules have been reported in the literature recently [4,5].

McConkey and co-workers [6,7] were the first to utilize laser-induced fluorescence (LIF) techniques in the quantitative detection of neutral ground-state dissociation products following electron impact dissociation of a molecule under single collision conditions. Recently, Abramzon et al. [8,9] introduced a variant of this LIF technique, which is conceptually similar to the approach of McConkey and co-workers and differs only in the details of the experimental realization of the technique. In a first step, Abramzon et al. used their apparatus in the determination of the absolute $N_2^+(X)$ ionization cross section as a function of electron energy following electron impact on N_2 [8,9]. Here, we report results of the extension of this technique to the electron impact dissociation of SiH_4 and SiF_4 leading to the formation of Si(^{1}S) and Si(1D ground-state atoms. Silane, SiH_4, is a frequently used constituent of low-temperature processing plasmas employed in the fabrication of Si-based microelectronic devices and other semi-conducting components. SiH_4 plays a particularly important role in the plasma-assisted deposition of silicon and amorphous silicon-hydride (a:SiH) films [10]. SiF_4 is the most abundant volatile by-product of the plasma-assisted etching of Si by plasmas with F-contaioning molecules in the feed gas mixture.

II. Experimental Apparatus and Procedure

The apparatus consists of an electron-beam and a gas-beam intersecting at right angles inside a vacuum chamber in conjunction with a tunable laser beam which propagates either parallel or antiparallel to the electron beam in order to maximize the overlap of the three beams. Optical detection of the LIF signal from the interaction region is made perpendicular to both the electron beam and the gas beam. The energy of the electron beam can be varied between 5 eV and 400 eV with typical beam currents of 3 μA at 25 eV and 20 μA at 100 eV and an energy resolution of about 0.5 eV (FWHM). The electron beam is collected in a Faraday cup which consists of three electrically insulated elements which enables us to measure the beam current as well as the beam divergence. The gas beam is an effusive beam emanating from a multi-capillary array of rectangular shape which is positioned about 8 mm above the electron beam axis. Roughly 50% of the total gas throughput passes through a rectangle of the size of the nozzle array in the interaction region. The pushing pressure behind the nozzle is continuously monitored by a capacitance manometer. The laser system consists of a pulsed Lumonics EX-520 excimer laser operating at 308 nm (XeCl) which is used to pump a Lumonics HD-500 dye laser using Exalite 392A as the dye of choice in the pump wavelength region around 390 nm. The laser system produces 0.0015 nm wide pulses of less than 10 ns duration of up to 3 mJ energy per pulse in the wavelength range from 375-397 nm. The laser beam enters and exists the vacuum chamber through Brewster-angle windows and the beam intensity passing through the vacuum chamber is monitored by a laser pulse energy meter. The fluorescence from the interaction region is imaged onto the cathode of a cooled Hamamatsu R1104 photomultiplier tube (PMT). Spectral isolation is achieved by a narrow-band interference filter. The output pulses of the PMT are processed by a gated photon counter whose output, in turn, is directed into a personal computer for data storage and further analysis. A different dye and a frequency doubler are employed for the measurements in the pump wavelength region around 288 nm.

The LIF measurements were carried out as follows. After the end of the laser pulse and after suitable delay had elapsed to allow scattered laser light to decay, a first gate (gate A) of the gated photon counter was opened for a period T corresponding to about 5 times the radiative lifetime of the radiating state. The data in gate A contain the LIF signal, any residual background and/or noise, and fluorescence produced by the continuous electron beam. At time T, gate A was closed and a second gate (gate B) was opened for the same period T. Since after a period of 5 lifetimes any residual LIF signal is negligible, the data in gate B contain only any residual background/noise and fluorescence produced by the continuous electron beam. The LIF signal was then obtained as the difference between the accumulated counts in gate A and gate B.

In Si, we employed the following LIF and detection scheme. Si atoms in the ^1S state of the ground-state $(1s)^2(2s)^2(3s)^2(3p)^2$ electron configuration resulting from the electron impact dissociation of SiH_4 were detected by pumping the $(3p)^2\ ^1S \rightarrow (3p)(4s)\ ^1P$ transition around 390 nm and recording the subsequent $(3p)(4s)\ ^1P \rightarrow (3p)^2\ ^1D$ fluorescence at 288 nm. The pump and detction pathways were interchanged for the detection of Si(^1D) atoms. LIF spectra in Si were recorded for impact energies from 20 eV to 120 eV. The properly normalized LIF spectra recorded at different electron energy yield the absolute cross section for the formation of Si(^1S) following neutral dissociation of SiH_4 as a function of energy.

III. Results and Discussion

The absolute cross section for the $N_2(X) \rightarrow N_2^+(X)$ is known [8,9]. Thus, its value at 45 eV of 40×10^{-18} cm^2 can be used to put the Si(^{1}S) cross section on an absolute scale in a straightforward fashion. We determined a value of 30×10^{-18} cm^2 at 45 eV. The error margin of our absolute cross section measurement is estimated to be 25%. The measured cross section (shown in fig. 1 below) rises rapidly from threshold to a plateau around 30 eV and peaks in the energy range from 50 - 70 eV with a maximum value of about 4×10^{-17} cm^2. The cross section declines fairly rapidly with increasing impact energy. The two data points at 40 eV were obtained under very different experimental conditions and thus demonstrate the reliability of the experimental technique. The shape of the cross section is rather similar to the shapes of various photoemission cross sections of Si and SiH_4 reported by Perrin and Aarts [11] which all displayed a prominent structure in the low-energy regime around 30 eV followed by a maximum around 60 eV and rapid decline towards higher impact energies. The shape of our cross section is rather similar to the shapes of various photoemission cross sections of Si and SiH_4 reported by Perrin and Aarts [11] which all displayed a prominent structure in the low-energy regime around 30 eV followed by a maximum around 60 eV and a rapid decline towards higher impact energies. It is interesting to note that the total SiH_4 ionization cross section has a maximum value of 5.4×10^{-16} cm^2 at 70 eV [12] which is roughly half the magnitude of the total SiH_4 neutral dissociation cross section obtained by Perrin et al. [13]. Basner et al. [12] also observed that the ionization of SiH_4 by electron impact is entirely dominated by dissociative processes resulting in the formation of various singly and doubly charged fragment ions.

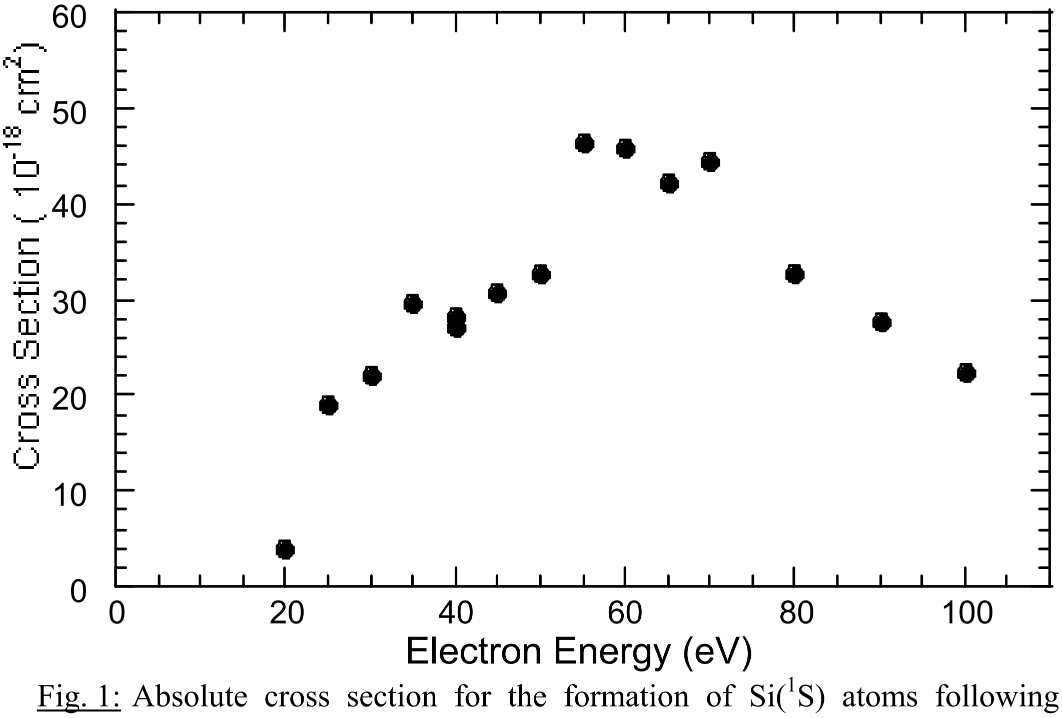

Fig. 1: Absolute cross section for the formation of Si(^{1}S) atoms following electron-impact induced neutral dissociation of SiH_4 as a function of electron energy.

Measurements of the cross section or formation of Si(^{1}S) atoms following electron-driven neutral molecular dissociation of SiF_4 are currently underway as are measurements of absolute cross sections for the formation of Si(^{1}D) atoms following electron-impact dissociation of both molecules. Earlier attempts to measure cross sections for Si(^{1}S) formation from Si-organic compounds such as TMS, TEOS, and HMDSO were unsuccessful , but allowed us to establish upper limits on these cross sections that were on the order of 10^{-20} cm^2 at 70 eV

Acknowledgments

We wish to acknowledge financial support of this work Division of Chemical Sciences, Office of Basic Energy Sciences, Office of Science, U.S. Department of Energy. We further acknowledge the use of equipment funded under NASA grants NAG5-4978 and NAG5-8971 One of us (KM) is also grateful for partial support from the above NASA grants.

References

[1] L.G. Christophorou (editor), *Electron-Molecule Collisions and Their Applications*, Academic Press: New York, 1984

[2] I. Shimamura, and K. Takayanagi (editors), Electron Molecule Collisions, Plenum Press: New York, 1984

[3] R.K. Janev, (editor), *Atomic and Molecular Processes in Fusion Edge Plasmas*, Plenum Press: New York , 1995

[4] T.N. Rescigno, Phys. Rev. A **50** (1994) 1382

[5] T.N. Rescigno, Phys. Rev. A **52** (1995) 329

[6] P.W. Zetner, M. Darrach, P. Hammond, W.B. Westerveld, R.L. McConkey, and J.W. McConkey, Chem. Phys. **124** (1988) 453

[7] M. Darrach and J.W. McConkey, J. Chem. Phys. **95** (1991) 754

[8] N. Abramzon, R.B Siegel, and K. Becker, Int. J. Mass Spectrom. **188** (1999) 147

[9] N. Abramzon, R.B. Siegel, K. Becker, J. Phys. B **32** (1999) L247

[10] T. Glenewinkel-Meyer, J.A. Bartz, G.M. Thorson, and F.F. Crim, J. Chem. Phys. **99,** 5944 (1993) and references therein to earlier work

[11] J. Perrin and J.F.M. Aarts, Chem. Phys. **80** (1983) 351

[12] R. Basner, M. Schmidt, V. Tarnovsky, K. Becker, and H. Deutsch, Int. J. Mass Spectrom. Ion Proc. **171** (1997) 83

[13] J. Perrin, J.P.M. Schmitt, G. de Rosny, B. Drevillion, J. Huc, and A. Lloret, Chem. Phys. **73** (1982) 383

Imaging of femtosecond photon induced dynamics in CF_3I and CF_2I_2

Wim Roeterdink and **Maurice H.M. Janssen**

Laser Centre and Department of Chemistry
Vrije Universiteit
De Boelelaan 1083
1081 HV, Amsterdam, The Netherlands

Femtosecond pump-probe imaging experiments on Rydberg state photon induced dynamics in CF_3I will be discussed. The femtosecond laser pulses excite the CF_3I molecules produced in a cold molecular beam expansion. The pulsed beam is produced by a small piezo pulsed valve synchronized to the 1 kHz repetition rate of the regen-amplified femtosecond laser system .

The angular and energy recoil distribution of the various ions produced in the multi-photon pump-probe excitation are measured with a sensitive two-dimensional MCP/CCD detector. The ion optics are configured for velocity map imaging providing a substantial improvement of the velocity resolution over the conventinal ion-grid extraction optics.

Pump-probe transients for the different ionic fragments will be presented as well as velocity map images at several time delays. The images give direct information about the kinetic energy release of the produced fragments and the angular recoil distribution at various pump-probe delays [1].

The competition between neutral fragmentation and dissociative ionization pathways will be discussed for both CF_3I and CF_2I_2

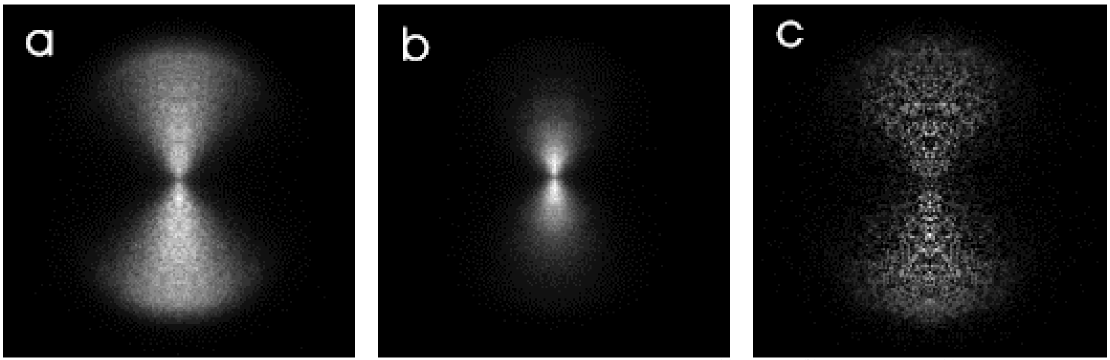

Images of the recoil of I^+ fragments at a pump-probe delay time of 0 $^{(a)}$, 200 $^{(b)}$ and 1000 $^{(c)}$ fs. The molecular beam is perpendicular to the plane, the polarization of the pump laser at 264.2 nm is vertical in the plane of the images.

References

[1] W.G. Roeterdink and M.H.M. Janssen, Chem. Phys. Lett. 345 (2001), 72-80

Electron induced chemistry in technological plasmas: Data for CF_3I, C_2F_4 and associated dissociated fragments

I. Rozum, N.J. Mason and Jonathan Tennyson

Department of Physics and Astronomy, University College London, Gower St., London WC1E 6BT, UK

Introduction

The plasma processing technology used in the fabrication of materials for microelectronics has became one of the most vibrant and commercially successful industries. Despite its high cost and technical importance, plasma equipment is still largely designed empirically, with little help from computer simulations. Models of technological plasmas require quantitative data on the reactions of all the constituent neutral species and ions, especially data on collisional, reactive processes occuring within the plasma.

The molecular reactants currently used (CF_4 and C_2F_6) in plasma processing procedure have been found to be detrimental to the terrestrial environment and global climate as both are strong greenhouse gases. CF_3I and C_2F_4 have been proposed as the next generation of plasma reactant since both have a low global warming potential but still provide efficient sources of CF, CF_2 and CF_3 radicals for the etching of silicon surfaces (Samukawa *et al* 1999).

We are developing a joint experimental and theoretical programme to investigate electron interactions with CF_3I and C_2F_4 and the radical fragments (CF_x). Initial experimental research has concentrated upon measuring absolute scattering cross sections for elastic scattering from and excitation of CF_3I at electron energies typical of those present in commercial plasma reactors. Vibrational excitation cross sections reveal resonance phenomena which indicate dissociative electron attachment may be important at low energies leading to injections of anions into the reactor plasma. A complete analysis of electronic excitation of CF_3I has also been performed, revealing new information on the spectroscopy of the molecule and dissociative pathways leading to reactive CF_x fragments.

The theoretical programme is studying of electron collisions with CF_x radical using the UK molecular R-matrix codes (Morgan *et al* 1998). The first target to be studied is CF_2.

Method

The R-matrix method is used to study the electron collisions with the CF_2 molecular radical (Burke and Berrington 1993, Morgan, Tennyson and Gillan 1998). The general application of R-matrix method to polyatomic molecules employing the UK polyatomic R-matrix code has been described in the literature (Morgan, Tennyson and Gillan 1998, Tennyson and Morgan 1999). The application of these codes to electron collisions with

Cl_xO_y radicals was described by Baluja *et al* (2000, 2001a, 2001b).

In the inner region the total wavefunction describing scattering of an electron by N-electron molecule is (Burke and Berrington 1993)

$$\Psi_k^{N+1} = A \sum_I \Psi_I^N(x_1, ..., x_N) \sum_j \xi_j(x_{N+1}) a_{Ijk} + \sum_m \chi_m(x_1, ..., x_N, x_{N+1}) b_{mk} \quad (1)$$

where A is the anti-symmetrization operator, x_n is the spatial and spin coordinate of the n^{th} electron, ξ_j is a continuum orbital spin-coupled with the scattering electron and a_{Ijk} and b_{mk} are variational coefficients determined by our program.

Target

Our calculations on CF_2 used the 6-311G* Gaussian basis set (11s5p/4s3p) and complete active space configuration interaction (CASCI) wavefunctions where the orbitals were represented by state-averaged pseudo-natural orbitals (NO) obtained from 'all singles and doubles' configuration interaction (CI) calculations for all target states. In averaging procedure we included the $^1A_1$, $^3B_1$, $^1B_1$ and $^3A_2$ states with a maximum weight given to the first excited state as this model gave better target properties.

The ground state dipole moment, calculated using our model (0.448 Debye) is in a very good agreement with the experimental data of Kirchhoff and Lide (1973) 0.469 ± 0.026 Debye and with theoretical calculations of Russo, Sicilia and Toscano (1992) 0.44 Debye.

The details of calculations and comparison with available experimental and theoretical data are described by Rozum *et al* (2002).

Scattering model

Our electron-CF_2 scattering calculations included the seven states X^1A_1, $^3B_1$, $^1B_1$, $^3A_2$, $^1A_2$ and $^3B_2$ and continuum orbitals of Faure *et al* (2001) up to g ($l \leq 4$) partial waves. The range of scattering energies was restricted to the energies below 10 eV. The Born correction that compensates for the neglect of terms with higher l in scattering amplitude, was added to the summed cross sections.

In order to study the dissociative behaviour of resonances we performed calculations in which one C-F bond was stretched from 1.8 a_0 to 3.7 a_0.

Results

Elastic cross sections for CF_2 were calculated at different geometries.The main feature in the elastic cross section is the presence of a shape resonance of $^2B_1$ symmetry (^2A" in C_s). At equilibrium geometry this resonance has position and width of 0.95 eV and 0.18 eV respectively. Analysis of the inner region eigenvectors shows that it is a shape resonance with the extra electron in $3b_1$ orbital.

CF_2 has an equilibrium dipole moment of 0.44 D, which may be enough to support a bound state. However, our calculations show that CF_2 does not have any bound states at its equilibrium geometry. With increasing a C-F bond length the $^2B_1$ (^2A") resonance energy curve approaches the ground state energy curve. As one C-F bond length is increased to 3.2 a_0, this resonance becomes bound (see figure 1). The $^2B_1$ (^2A") resonance thus displays the classic behaviour one would expect of resonance supporting dissociative

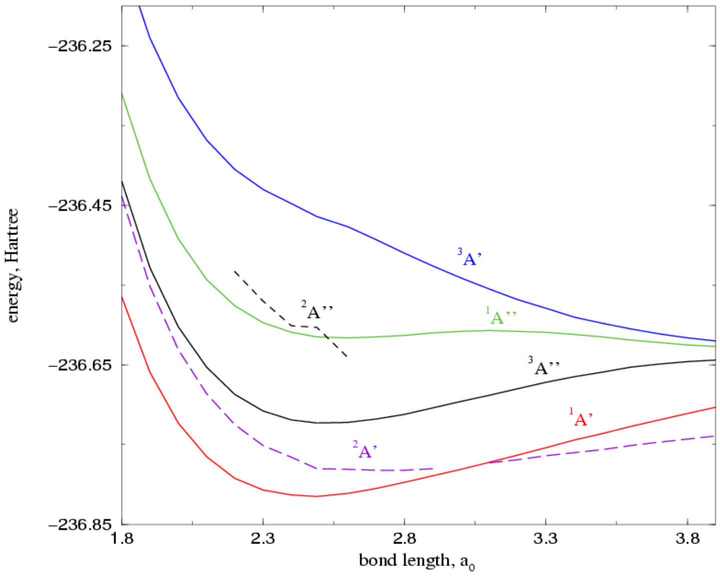

Figure 1. Electronic state energies of CF_2 as a function of changing one C-F bond. The dashed lines represent the resonance energy curves. The dotted line below ground state curve represents the bound state curve. Curves are labelled by the symmetry in the C_{2v} (C_s) point groups.

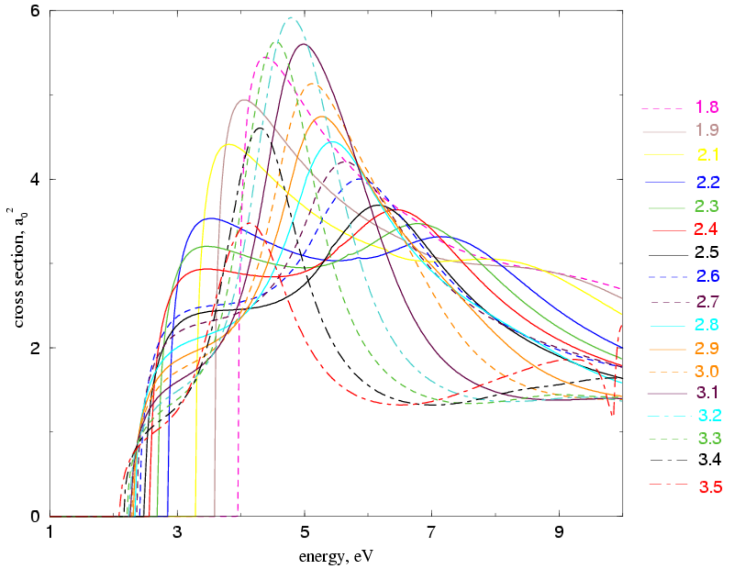

Figure 2. Total cross sections for electron impact excitation of the first excited state $^3B_1$ (^{3}A" in C_s) of CF_2 plotted at different C-F bonds (from 1.8 a_0 to 3.5 a_0).

attachment. Asymptotically the resonance dissociates to CF + F^-(^2P_u) which one would therefore expect to be a major product of low energy electron collisions with CF_2.

Figures 2 presents electron-impact electronic excitation cross section from the ground state $^1A_1$ to the first excited states $^3B_1$. This excitation process is dominated by the $^2A_1$ (^{2}A') symmetry in which there is a prominent resonance with a position and width at equilibrium geometry of 5.61 eV and 2.87 eV respectively. This shape resonance binds the extra electron in the $7a_1$ orbital.

Conclusions

Our calculations on CF_2 give resonance parameters as well as elastic cross-section and excitation cross-sections for the six low-lying excited states, of symmetry $^3B_1$, $^1B_1$, $^3A_2$, $^1A_2$, $^3B_2$ and $^1B_2$. These states have vertical excitation energies in the range 2.44 to 10 eV. We have found shape resonances of $^2A_1$ and $^2B_1$ symmetries at 5.61 and 0.95 eV respectively. Performing an asymmetric stretch of CF_2 we found that $^2B_1$ (^2A" in C_s symmetry) resonance is bound at a bond length beyond 3.2 a_0, providing a route for dissociative attachment in this molecule (Rozum *et al* 2002).

We have started to perform calculations on electron collisions with the CF_3 radical. Only the dipole moment and the Hartree-Fock energy for the ground state of CF_3 are known. In order to obtain the target parameters, in particular the vertical excitation energies, we are performing molecular structure calculations using program GAMESS.

Asknowledgments

This work was supported by the UK Engineering and Physical Sciences Research Council. We wish to thank to L.A. Morgan, J. Gorfinkiel and K.L. Baluja for usefull discussions and guidance.

References

Baluja K L, Mason N J, Morgan L A and Tennyson J 2000 *J. Phys. B: At. Mol. Opt. Phys.* **33** L677

Baluja K L, Mason N J, Morgan L A and Tennyson J 2001 *J. Phys. B: At. Mol. Opt. Phys.* **34** 2807

Baluja K L, Mason N J, Morgan L A and Tennyson J 2001 *J. Phys. B: At, Mol. Opt. Phys.* **34** 4041

Burke P G and Berrington K A 1993 *Atomic and Molecular Processes - An R-matrix Approach* IOPP, Bristol

Faure A, Gorfinkiel J D, Morgan L A and Tennyson J 2001 *Comput. Phys. Commun.* (to be published)

Morgan L A, Tennyson J and Gillan C J 1998 *Comput. Phys. Commun.* **114** 120

Rozum I, Mason N J and Tennyson J 2002 *J. Phys. B: At, Mol. Opt. Phys.* (to be submitted)

Samukawa S, Mukai T and Noguchi K 1999 *Material Science in Semiconductor Processing* 203

Tennyson J and Morgan L A 1999 *Phil. Trans. R. Soc. Lond. A* **357** 1161

Negative and Positive Ionisation Processes in SF_5-CF_3

W. Sailer, H. Drexel, V. Grill, A. Pelc[a], B. Gstir, G. Hanel, M. Probst, N.J. Mason[b], E. Illenberger[c], J. Fedor[d], J.D. Skalny[d], P. Scheier, and T.D. Märk[e]

Institut für Ionenphysik der Leopold Franzens Universität, Technikerstrasse 25, A - 6020 Innsbruck, Austria

[a] *Institute of Physics, Maria Curie-Sklodowoska University, Lublin, 20031 Poland*
[b] *Department of Physics and Astronomy, University College London, Gower Street, London WC1E 6BT, UK*
[c] *Institut für Chemie-Physikalische und Theoretische Chemie, FU-Berlin, Takustrasse 3, D-14195 Berlin, Germany*
[d] *Department of Plasmaphysics, Comenius University, 84248 Bratislava, Slovak Republic*
[e] *also adjunct Professor at Department of Plasmaphysics, Comenius University, 84248 Bratislava, Slovak Republic*

1. Introduction

Trifluoromethyl sulphur pentafluoride, SF_5CF_3, was recently discovered in stratospheric air at concentrations of about 0.12 ppt with the tendency to increase at a rate of about 6 % per year.[1] The molecule possesses several remarkably strong IR bands in the "atmospheric IR window" (800 - 1300 cm^{-1}). Due to these properties it is considered to be the most effective greenhouse gas on a per molecule basis in the Earth's atmosphere. By assuming the same atmospheric lifetime as SF_6, the global warming potential (GWP) of SF_5CF_3 is estimated to be 18 000 times that of CO_2.[1] However, due to the low concentration its contribution to the overall radiative force in the atmosphere remains at present very small.

In our experiments low energy electron attachment and electron impact ionisation to this potent greenhouse gas is studied at high energy resolution by means of mass spectrometric detection of the product anions/cations. A large dissociative electron attachment (DEA) cross section forming $SF_5^- + CF_3$ is observed within a very narrow energy range close to zero eV. In addition, comparatively weak resonances are observed near 1 eV yielding the fragment ions CF_3^- and F^-. In the first direct electron impact ionisation measurement of this compound several cations (CF_3^+, CF_2^+, CF^+, SF_5^+, SF_4^+, SF_3^+, SF_2^+, SF^+) are detected and their appearance energies (AE) measured. Some implications for the atmospheric lifetime of SF_5CF_3 and hence its global warming potential (GWP) are considered.

Thus, apart from its possible role in the atmosphere, a comparison of the attachment behaviour between SF_5CF_3, SF_6 [2] and for instance two other SF_6-derivatives, namely SF_5Cl (chloro sulphurpentafluoride) and SF_5NCO (pentafluorosulphur isocyanate) is of general interest.

2. Experimental

The dissociative electron attachment spectrometer consists of a molecular beam system, a high resolution trochoidal electron monochromator (TEM) and a quadrupole mass filter with a pulse counting system for analysing and detecting the ionic products. The TEM used here has recently been described in detail.[3] It achieves an energy resolution of 35 meV, for the present experiments, the instrument was operated at an FWHM of ≈ 80 meV, a reasonable compromise between product ion intensity and electron energy resolution. The electron impact ionization spectrometer consists of a molecular beam system, a hemispherical electron monochromator and a quadrupole mass filter with a pulse counting system, too. For negative ion formation the energy scale was calibrated by recording Cl^- from CCl_4,[4] for positive ionization it was calibrated against the appearance energy of cations from krypton.

3. Anion yields

Electron attachment to SF_5CF_3 in the electron energy range 0-10 eV generates three anionic fragments SF_5^-, CF_3^- and F^- (Figure 1) with intensity ratios (as monitored by the count rate at the highest peak of the respective cross section curves) of 1:0.004:0.0007. The present relative cross section data of SF_5^- have been calibrated by using the absolute data for the total cross section reported by Chen et al. [5], the CF_3^- and F^- data by using the measured intensity ratios.

From thermodynamic considerations of the different bond strengths involved we assign the observed anion signals to the following dissociative electron attachment reactions

$$\begin{array}{lclcl}
e^- (E \approx 0\ \text{eV}) & + & SF_5CF_3 & \rightarrow & SF_5^- + CF_3 \\
e^- (E \approx 1.1\ \text{eV}) & + & SF_5CF_3 & \rightarrow & SF_5 + CF_3^- \\
e^- (E \approx 0\ \text{eV}) & + & SF_5CF_3 & \rightarrow & F^- + SF_4\,CF_3 \\
e^- (E \approx 0.9\ \text{eV}) & + & SF_5CF_3 & \rightarrow & F^- + SF_5\,CF_2
\end{array}$$

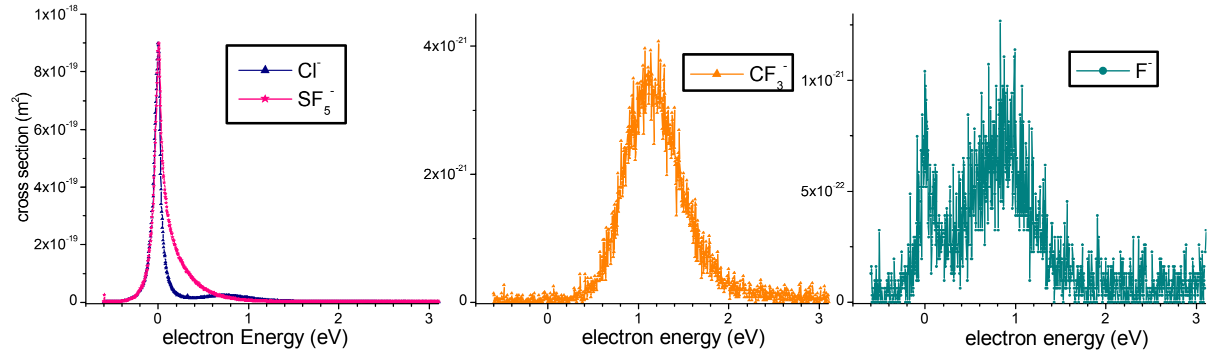

Figure 1

4. Cation yields

The appearance energies of the product cations were derived using a data analysis procedure described in detail in a recent publication.[6]

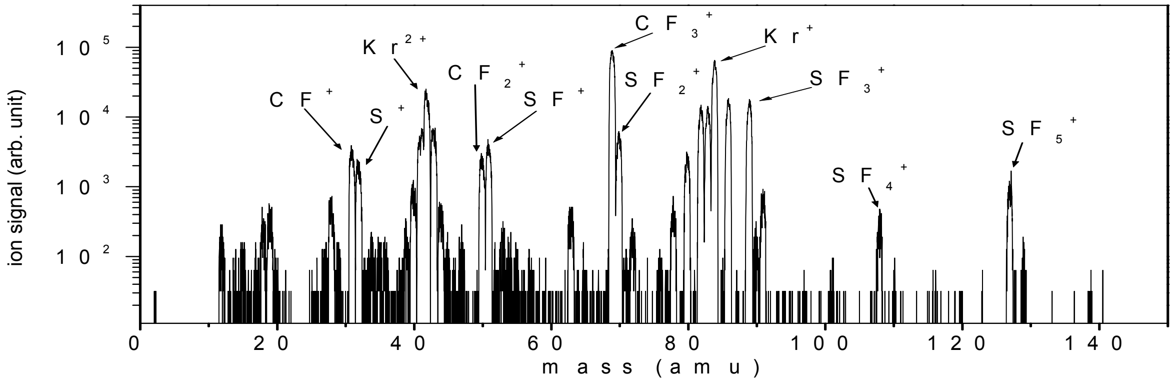

Figure 2

Figure 2 shows the mass spectrum of SF_5CF_3 together with krypton which was used as the calibrant of the electron energy for determining the appearence energies. No parent ion was observed at any incident electron energy suggesting that the lifetime of $SF_5CF_3^+$ is insufficient for its transit through the quadrupole (< 10 microseconds). Fragment ions observed include

CF^+, CF_2^+, CF_3^+, SF^+, SF_2^+, SF_3^+,SF_4^+ and SF_5^+. The strongest signal arises from CF_3^+, a process that involves the simple rupture of the S-C bond. Due to the similar masses (50,51) and isotope effects, the signal from CF_2^+ may be partially influenced by SF^+ as may CF_3^+ and SF_2^+ (masses 69 and 70 respectively). CF^+ is also close to S^+ (mass 31 and 32 respectively) but we do not believe that at the low energies used in this experiment any S^+ will be formed since this would require complete fragmentation of the parent molecule. This is partly confirmed by experiments on the related compound SF_6 where no S^+ ions are formed at electron energies below 100 eV. Formation of $SF_4^+ + CF_4$, a process that requires the migration of single fluorine atom across the S-C bond, exhibits the lowest ionisation threshold of all the fragment ions produced.

The following table gives the cation reaction processes identified and the corresponding energetics.

$e^- (E \geq 24.44 \pm 0.10\ eV) + SF_5CF_3 \rightarrow CF^+$
$e^- (E \geq 17.80 \pm 0.50\ eV) + SF_5CF_3 \rightarrow CF_2^+$
$e^- (E \geq 12.87 \pm 0.10\ eV) + SF_5CF_3 \rightarrow CF_3^+$
$e^- (E \geq 12.66 \pm 0.20\ eV) + SF_5CF_3 \rightarrow SF^+$
$e^- (E \geq 15.6 \pm 1.0\ eV) + SF_5CF_3 \rightarrow SF_2^+$
$e^- (E \geq 14.48 \pm 0.10\ eV) + SF_5CF_3 \rightarrow SF_3^+$
$e^- (E \geq 12.10 \pm 0.30\ eV) + SF_5CF_3 \rightarrow SF_4^+ + CF_4$
$e^- (E \geq 16.10 \pm 0.30\ eV) + SF_5CF_3 \rightarrow SF_4^+ + CF_3 + F$
$e^- (E \geq 13.16 \pm 0.60\ eV) + SF_5CF_3 \rightarrow SF_5^+$

In order to obtain information about the dissociation pathways of the $SF_5CF_3^+$ cation and to compare between the measured AEs and the theoretically predicted ones, we performed quantum chemical calculations at the MP2, B3LYP levels of theory and with the G2MP2 model chemistry. All methods of calculation predict for the two reactions producing CF_3^+ and SF_4^+ AE's too low by about 1eV compared with the experimental values, whereas values for the cations with higher AE's tend to agree slightly better, the theoretical values being higher than the experimental ones.

5. Implications for the role of SF_5CF_3 in the terrestrial atmosphere

The chemical reactivity of SF_5CF_3 is very low as are the photodissociation [7] and photoabsorption [8] rates. Hence ion-molecule reactions [9] and elecron attachment rates come into play in determining the atmospheric lifetime and thus the ultimate global warming potential. As the density of free electrons in the earth's atmosphere is low, the gas phase DEA may not be at a level to be of relevance in any of the complex cycles in atmospheric chemistry of SF_5CF_3.[10] However, it is accepted that photon initiated heterogeneous chemistry at the surface of particles (dust particles, aerosols, polar stratospheric cloud particles) can play an important role in the destruction of stratospheric species (e.g. the ClO_x compounds) [11]. Since electron attachment to SF_5CF_3 is exclusively dissociative we would expect the atmospheric lifetime of SF_5CF_3 to be quite short. Further experiments are however required to investigate the properties of SF_5CF_3 on ice and dust surfaces.

Acknowledgment

This work has been supported in part by the FWF, Wien, Austria and the EU Commission, Brussels and the Austrian-Slovak Cooperation Programme. N. J. Mason thanks the UK

EPSRC for financial support and J. D. Skalny acknowledges provisions from grant Vega 1/8313/01.

References

[1] W. T. Sturges, T. J. Wallington, M. D. Hurley, K. P. Shine, K. Sihra, A. Engel, D. E. Oram, S. A. Penkett, R. Mulvaney, and C. A. M. Brenninkmeijer, *Science* **289** (2000) 611.

[2] L. G. Christophorou, D. L. McCorkle, and A. A. Christodoulides,*Chapter: Electron Attachment Processes*, in: L.G. Christorphorou (Ed.), *Electron-Molecule Interactions and Their Applications*, Vols I, Academic, Orlando, FL, 1984.

[3] V. Grill, H. Drexel, W. Sailer, M. Lezius and T. D. Märk, *Int. J. Mass Spectrom.* **205** (2001) 209.

[4] D. Klar, M.-W. Ruf and H. Hotop, *Int. J. Mass Spectrom.* **205** (2001) 93

[5] C. L. Chen, R. E. Wotton and P.J.Chantry Proceedings of 7th International Conference on Gas Discharges and their Applications (1982) 321

[6] Matt S, Echt O, Wörgötter R, Grill V, Scheier P, Liftschitz C and Märk TD (1997) *Chem. Phys. Lett.* **264** 149

[7] R. Y. L. Chim, R. A. Kennedy, R. P. Tuckett, W. Zhou, G. K. Jarvis, D. J. Collins and P. A. Hatherly, *J. Phys. Chem.* (2001) submitted for publication.

[8] P.A. Kendall and N.J. Mason, *J. Electron. Spec. and Rel. Phenom.* **120** (2001) 27-31

[9] C. Atterbury, R.A. Kennedy, C.A. Mayhew and R.P. Tuckett, *Phys. Chem.Chem. Phys.* **3** (2001) 1949

[10] H. H. Rees, *Physics and Chemistry of the Upper Atmosphere*, Cambridge University Press, Cambridge, 1989.

[11] C. R. Webster et al. *Science* **261** (1993) 1130.

Excitation of chiral molecules and their hydrated clusters by R2PI studies.

M. Satta[b], S. Piccirillo[d], D. Scuderi[a], A. Paladini[a], L. Dalla Vedova[c], A. Filippi[c], M. Speranza[c], A. Giardini[a,b]

[a] *Dipartimento di Chimica, Università di Roma "La Sapienza", pl. A. Moro 5, I-00185 Roma, Italy*
[b] *CNR-Istituto Materiali Speciali, I-85050 Tito Scalo (Pz), Italy*
[c] *Facoltà di Farmacia, Dipartimento di Chimica e Tecnologia delle Sostanze Biologicamente Attive, Università di Roma "La Sapienza", pl. A. Moro 5, I-00185 Roma, Italy*
[d] *Università di Roma "Tor Vergata"Dipartimento di Scienze e Tecnologie Chimiche, Via della Ricerca Scientifica, I-00133 Rome, Italy*

1. Introduction.

Molecular clusters play a key role in the molecular scale explanations of macroscopic phenomena, being in between the isolated gas phase and the condensed phase. This condition allows to obtain information on intermolecular forces (dispersive, polarization, and electrostatic forces) simply by studying the physicochemical properties of isolated clusters and to extend them macroscopic systems. Weak interactions and hydrogen bond are particularly relevant both in inorganic as well as biological systems, characterized by high molecular and chiral selectivity.

Molecular-scale understanding of intermolecular forces and solvation effects can be performed through gas phase methodologies as laser spectroscopy and mass spectrometry [1,2]. Only recently these methodologies have been applied to study the physicochemical properties of chiral systems [3-5], while in condensed phase enantioselective intermolecular interactions have been studied in the past by various techniques (NMR, CD, Chromatography).

In this paper we report on a comprehensive study of the short-range forces operating in the molecular complexes between several chiral aromatic alcohols (M) and water (***solv***), through the application of mass resolved REMPI technique.

2. Experimental methodology.

The experimental setup, which combines a supersonic molecular beam, two Nd-YAG pumped dye lasers and a time of flight (TOF) mass spectrometer, has been already described [5]. Supersonic beam production of the adducts is obtained by adiabatic expansion of a carrier gas (Ar) seeded with a selected chromophore **M** and partners ***solv*** through a heatable pulsed nozzle of 400 μm i.d. The concentration is ma intained enough low to minimize the contribution of heavier clusters to the spectra. The skimmed supersonic jet (1 mm skimmer diameter) enters into a second chamber equipped with a TOF mass spectrometer. Molecules and clusters in the beam are excited and ionized by one or two tunable dye lasers pumped by the same Nd-YAG laser and the ionized species are detected by a channeltron. The mass selected photoionization signals are recorded and averaged by a digital oscilloscope and stored on a PC.

One colour R2PI experiments (1cR2PI) involve electronic excitation of the species of interest by absorption of one photon $h\nu_1$ and by its ionization by a second photon $h\nu_1$. Mass discrimination of the ionized complex may be complicated by its fragmentation, due to the excess energy gained in ionization process [4, 6-7].

The photoionization efficiency curves have been obtained by two colour R2PI (2cR2PI) sequence: i- the first exciting laser ($h\nu_1$) is tuned on the $S_1 \leftarrow S_0$ transition of the species of interest; ii- the laser intensity is lowered to about 1% of the initial fluence to minimize the $h\nu_1$ absorption; iii- a second laser ($h\nu_2$) is scanned through the cluster ionization and fragmentation threshold regions. The photoionization spectra were corrected for the effect of the electric field strength (200 V/cm) produced by the extraction plates of the TOF spectrometer.

The binding energy D''_0 of the **M-*solv*** adduct is computed from the difference between its dissociative ionization threshold $AE(\mathbf{M})^+ = h\nu_1(\mathbf{M}\text{-}\boldsymbol{solv})^* + h\nu_2(\mathbf{M}^+ + \boldsymbol{solv})$ and the ionization threshold of bare **M**, i.e. $IP(\mathbf{M}) = h\nu_1(\mathbf{M})^* + h\nu_2(\mathbf{M})^+$. The dissociation energy D^+_0 of the ionic cluster $(\mathbf{M}\text{-}\boldsymbol{solv})^+$ is calculated from the difference between its dissociative ionization threshold, $AE(\mathbf{M})^+ = h\nu_1(\mathbf{M}\text{-}\boldsymbol{solv})^* + h\nu_2(\mathbf{M}^+ + \boldsymbol{solv})$, and its ionization threshold $IP(\mathbf{M}\text{-}\boldsymbol{solv}) = h\nu_1(\mathbf{M}\text{-}\boldsymbol{solv})^* + h\nu_2(\mathbf{M}\text{-}\boldsymbol{solv})^+$.

3. The hydration of aromatic molecules.

Hydrated aromatic molecules are simple model systems for the study of selectivity and function of biologically active systems. The role of hydrogen bond interaction and molecular conformation in these systems has been studied for many aromatic molecule –water systems [6] and also on molecules of biological interest [8]. R2PI studies of hydrated clusters of aromatic alcohols are reported. The measure of shifts and binding energy of these systems can lead information on the behaviour of water, which can acts both as proton donor and proton acceptor.

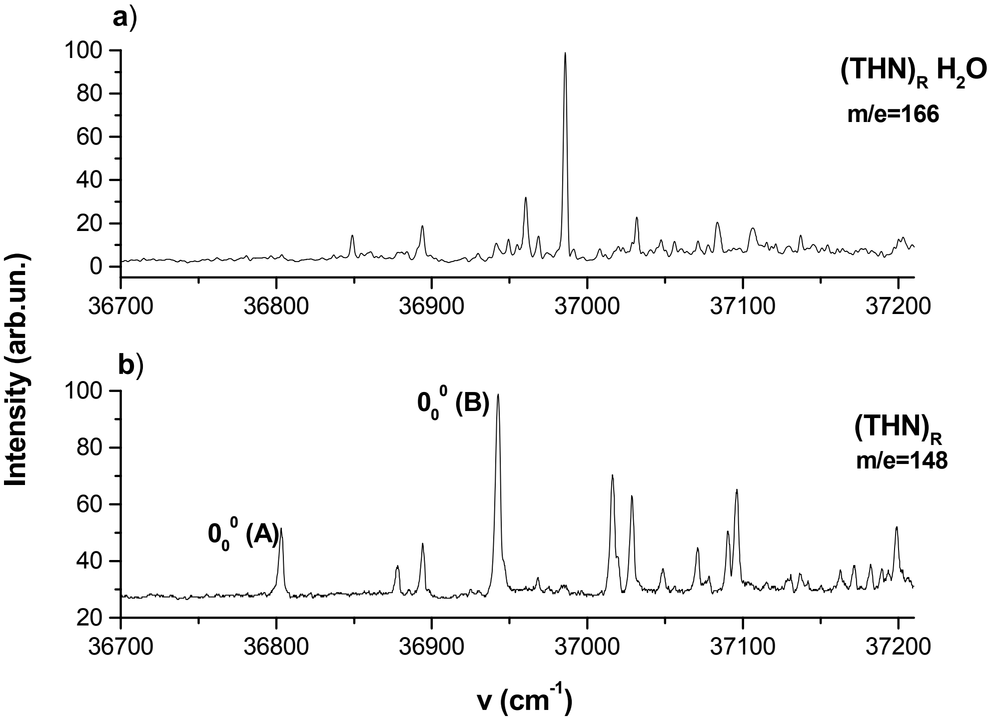

Figure 1 Mass-resolved one colour R2PI excitation spectra of $\mathbf{THN_R}$ (a) and $\mathbf{THN_R\text{-}H_2O}$ (b), measured respectively at *m/z* = 148 and *m/z* = 166, and at a total stagnation pressure of 3 bar.

In fig. 1, the one colour R2PI spectra of 1-tetralol ($\mathbf{THN_R}$) and $\mathbf{THN_R\text{-}H_2O}$ are shown. The two bands marked in the spectrum are tentatively assigned to the two axial and equatorial conformers of $\mathbf{THN_R}$. As already found for 1-phenyl-1-ethanol - water and 1-phenyl-1-propanol – water clusters a blue shift with respect to the 0_0^0 electronic transition $S_1 \leftarrow S_0$ of the chromophore is observed. A blue shift reflects the fact that the interaction forces decrease upon excitation. The blue shift of the electronic transition in many 1:1 aromatic molecule-water cluster is not unusual and can be related to a O—H ---- π interaction between water and the chromophore, in which water acts as proton donor [8,9].

In fig. 2b the one colour R2PI spectra of 1-indanol ($\mathbf{I_R}$) is reported. The two stable conformers predicted from *ab initio* calculation for $\mathbf{I_R}$ molecule, cannot be easily assigned in the spectrum. The spectra of the two conformers could be superimposed within 1-2 cm^{-1}. A few vibronic bands calculated in the harmonic calculations, are marked in the spectrum. Experimental shift of the 0^0_0 electronic transition for **I_R-H_2O** (fig. 2a) is around 0 cm^{-1}. At variance with other non cyclic benzylic alcohols, calculations for **I_R-H_2O** predict that in the most stable structure, **I_R** acts as a proton acceptor towards water, and the O—H --- π interaction is negligible.

The combination of mass selected R2PI technique and *ab initio* computation has proven to be an efficient tool in the study of the hydrated clusters of benzylic alcohols produced in the low temperature envoronment of a supersonic beam.

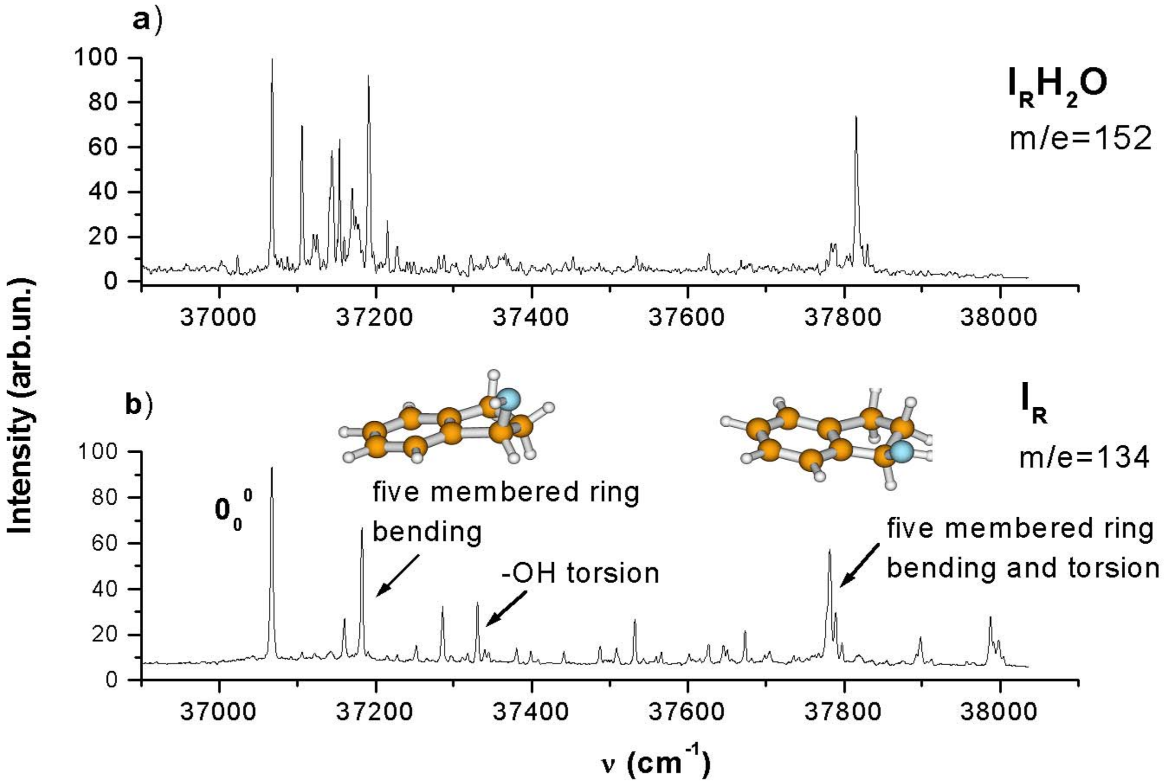

Figure 2 Mass-resolved one colour R2PI excitation spectra of **I_R** (a) and **I_R-H_2O** (b), measured respectively at *m/z* = 134 and *m/z* = 162, at a total stagnation pressure of 3 bar.

References

---

[1] A.W. Garret and T.S. Zweir, *J. Chem. Phys.*, 1992, **96**, 3402.

[2] W. A. Tao, D. Zhang, E. N. Nikolaev, R. G. Cooks, *J. Am. Chem. Soc.* 2000, **122**, 10598; W. A. Tao, R. G. Cooks, *Angew. Chem. Int. Ed. Engl.* 2001, **40**, 757.

[3] K. Le Barbu, F. Lahmani, M. Mons, M. Broquier, A. Zehnaker, *Phys.Chem.Chem.Phys.*, 2001, **3**, xxx

[4] A. Latini, D. Toia, A. Giardini Guidoni, S. Piccirillo and M. Speranza, *Angew. Chem.*, 1999, **111**, 838; A. Latini, M. Satta, A. Giardini Guidoni, S. Piccirillo and M. Speranza, *Chem. Eur. J.*, 2000, **6**, 1042.

[5] D. Consalvo, A. van der Avroid, S. Piccirillo, M. Coreno, A. Giardini Guidoni, A. Mele and M. Snels, *J. Chem. Phys.* 1993, **99**, 8398

[6] B. Brutchy, *Chem Rev.*, 1992, **92**,1567

[7] H. J. Neusser and H. Krause, *Chem. Rev.*, 1994, **94**, 1829

[8] R. J. Graham, R.T. Kroemer, M. Mons, E. G. Robertson, L.C. Snoek, J. P. Simons, *J. Phys. Chem.* A, 1999, **103**, 9706; M. Mons, E. Robertson, J.P. Simons. *J.Phys.Chem. A* 2000, **104**, 420.

[9] R.N. Pribble, T.S. Zwier, *Science* 1994, **265**, 75

Ion optics evaluation of the Plasma Ion Mass Spectrometer (PIMS) designed for the JET tokamak

W. Schustereder, G.F. Matthews[1], N. Cant[1], S.K. Erents[1], J. Vince[1], A. Qayyum, C. Mair, P. Scheier, T.D. Märk

Leopold-Franzens-University of Innsbruck, Institute for Ionphysics, Technikerstr. 25, A-6020 Innsbruck
[1]UKAEA/Euratom Fusion Association, Culham Science Centre, Abingdon, Oxon OX14 3DB,UK

1. Introduction:

Until the development of the Plasma Ion Mass Spectrometer (PIMS) there was no device available for measuring the absolute flux of ions in each charge state flowing in the edge plasma of tokamaks (magnetic fusion devices). Besides the knowledge of the local density in the edge region the PIMS can give an indication of the average ion temperature of the impurities [1,2,3]. The charge state distribution and absolute flux of impurities is dependent on the location and magnitude of the impurity sources and the transport of impurity ions within the scrape-off layer (SOL) and on closed flux surfaces.

The benefit of mass spectrometry compared to spectroscopic methods is that a full evaluation of species in the plasma edge can be achieved by this *in-situ* measurement at a very precisely defined point in space [1,2,3]. These measurements are very relevant for next step of magnetic fusion experiments such as ITER (International Thermonuclear Engineering Reactor) [4] since the production and screening of impurities in current tokamaks is still not well understood and ITER will need a low plasma impurity content to reach its fusion energy goals. JET is currently the closest tokamak in size to ITER in operation today and the only machine in which both beryllium and carbon can be used as wall materials as is planned for ITER. PIMS measurements in JET would provide an excellent benchmark for the edge plasma simulation codes and thus improve our predictions for ITER.

2. Description of the PIMS and its simulation:

The PIMS is a trochoidal mass spectrometer that uses the magnetic field for the confinement of the plasma as its B-field. Thus only electrostatic voltages are needed for the operation of this instrument. The specific requirements for the design of an *in-situ* mass spectrometer can be summarised as follows:

- The instrument must not be negatively affected by the high magnetic field of the tokamak. In JET the range of toroidal magnetic fields used routinely is 1 to 3.4 T.
- The ion optics has to deal with a wide spread of initial ion velocities since the plasma is a hot ion source.
- The geometry must be simple so that the relative transmission probability of various ions is straightforward to model, since there is no practical means to calibrate the device.
- The intensity of the ion source in the boundary plasma necessitates an attenuating slit to avoid space charge effects that may occur if too much current is extracted into the device.
- The outer shell and entrance slit need to withstand up to 40 MW/m^2 for periods of 200 ms which corresponds to the time it takes the JET reciprocating probe drive to insert and withdraw the probe head from the JET plasma. The bulk temperature of the probe may transiently reach 500° C.

The JET reciprocating probe drives are located on the top of the torus. Every two seconds the probe head can be driven into the plasma edge using a fast pneumatic system giving a typical exposure time of 200 ms to the plasma. The drive system imposes important constraints on the probe head design:

- The external diameter of the probe must not exceed 40 mm to be compatible with the JET probe drives. The size also needs to be kept down to minimize the voltage required since breakdown can be a problem in the plasma environment.
- The probe has to be aligned to within a few degrees with the local magnetic field. The most common magnetic field on axis (3.0 m major radius) is 2.5 T, so the field for the reciprocating PIMS probe head at a radius of 3.25 m will be typically 2.3 T (assuming 1/R scaling).

The dimensions of the active components of the JET PIMS are 4.35×8.5×18.5 mm. The focal length is 5.45 mm as compared to 9.5 mm used on DITE [2] and TEXTOR [3]. The ratios of the other dimensions to those in the earlier devices are similar. Due to the space restrictions the number of collectors has also been reduced to two. The entrance slit is 0.1 mm in width and made out of a single piece of TZM molybdenum alloy to maximize its power handling characteristics. Figure 1 shows the geometry of the PIMS as realised in the ion optics calculations including some trajectories calculated with the ion trajectory program SIMION 6 for realistic electric and magnetic fields.

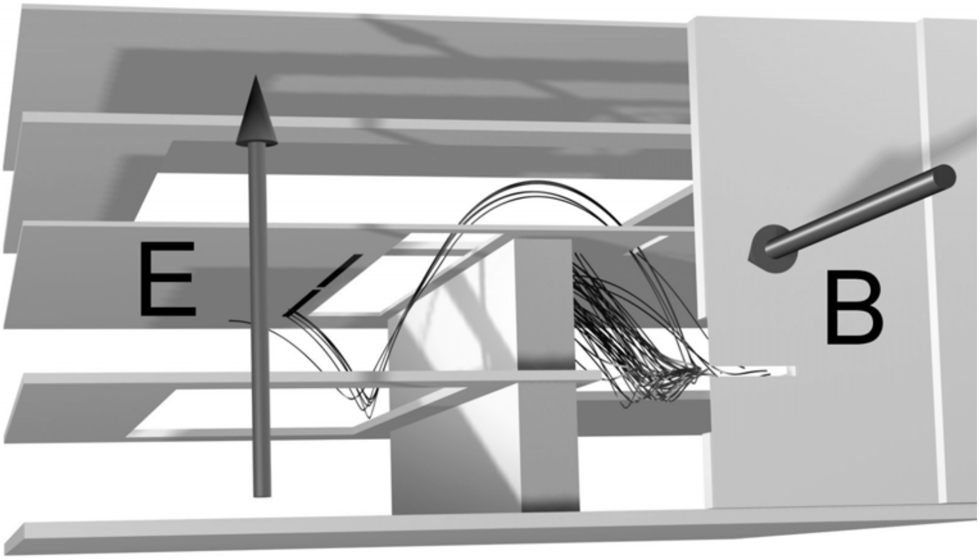

Figure 1: Geometry of the PIMS probe as realised in the ion optical calculations.

Ions enter the PIMS through a small entrance slit in the plate perpendicular to the magnetic field and hence to the other plates in the device. This entrance slit is a symmetry point in the PIMS such that the potential of the plate that is level with the slit remains the same constant potential as the slit. The number of particles reaching the collector regions is a function of the ion temperature and the sheath voltage along with the electric field across the device.

SIMION 6 as well as the similar custom written code in JET [2] compute the vacuum electric fields associated with a series of electrodes defined on a rectangular three dimensional grid through a numerical solution of Laplace's equation. Ions are randomly generated at the entrance slit with a Maxwellian distribution corresponding to a temperature T_i, and are accelerated parallel to the magnetic field to allow for acceleration in the plasma sheath. Ions are then followed through the structure until they impact with one of the surfaces or exit the grid.

The most important issue to be calculated in the ion optics simulations is the transmission of the different charge states of ions we expect to see in the edge of JET. It is clear that the PIMS is expected firstly to detect and distinguish deuterium and carbon ions of different charge states plus smaller amounts of beryllium. Simulations were carried out to confirm that the geometry of the PIMS chosen has transmission characteristics that are not too sensitive to sheath voltage and ion temperature, and that magnetic field misalignment does not significantly degrade the resolution.

Our base case assumes an ion temperature T_i = 50eV and sheath voltage, V_s = 100V (from sheath theory $V_s \approx 3T_e$). Figure 2 shows the maximum transmission versus charge state for the base case where the transmission is the current at the collectors divided by the current entering the device. The results presented here are for the most common toroidal magnetic field at the probe of 2.3 T. One can see from figure 2 that the ions with high M/Z are mainly deposited on collector 2 whilst those with low M/Z go to collector 1. This is because the ions reach the collector from the defining slit in one gyro-period and during this time travel parallel to the magnetic field, see figure 1. Although a single ratio of the two collector currents would not allow one to distinguish the sheath voltage from the ion temperature, by using the current ratios for ions with a range of M/Z the problem becomes soluble [2].

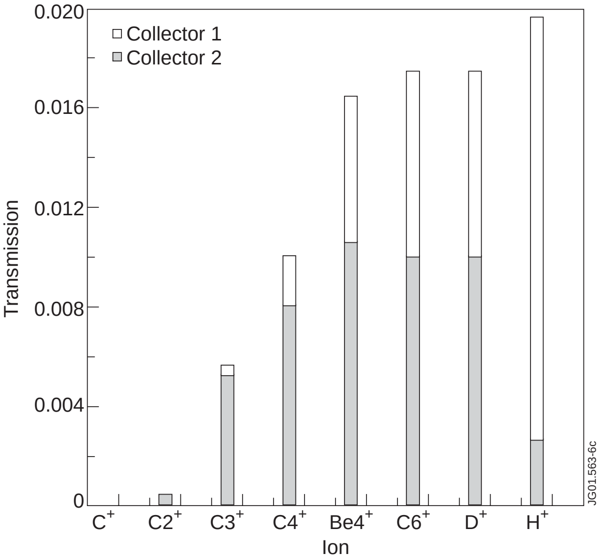

Figure 2: Peak transmission for different charge states of carbon for the base case (see text).

The effects of small field misalignments will be a crucial point in operating the PIMS in JET. This is due to the fact that although the toroidal magnetic field is well known the poloidal magnetic field is not so well known due to uncertainties in the radial profile of the plasma current. The total magnetic field in JET is helical with typical pitch of 15°. In this situation the electric and magnetic fields inside the PIMS may no longer be orthogonal to each other. Misalignments of ±3° about both axes are considered a worst case and have been investigated.

Since we will be making measurements under conditions of variable ion temperature and sheath voltage it is important to ensure that the total transmission (collectors 1 + 2) is not too strongly dependent on the edge ion temperature and sheath voltage. Scans have therefore been done in these parameters for all charge states.

3. Conclusions:

The edge of a magnetic fusion device is a severe and demanding environment for deploying a mass-spectrometer, particularly one whose purpose is to sample a high temperature plasma. Previous experience on small tokamaks has however shown the feasibility and utility of such devices. However, as the largest tokamak in the world, the JET environment and probe drive systems place even more severe demands on the design, including the need to shrink the device dimensions by 43% to give a focal length of 5.45 mm and fit within an overall diameter of 40 mm. Our simulations of the ion optics of the proposed device have however shown that we expect good transmission for the high charge state ions which are predicted to be the most abundant and hence of greatest interest to us. It is clear that ion optics simulations will be essential to the interpretation of any results obtained from the device.

Future work will concentrate on developing biasing schemes and minor geometric variations to optimise the transmission of the lower charge state ions.

Acknowledgements:

Work was carried out under the European Fusion Development Agreement as an EFDA-JET enhancement project and was partly funded by EURATOM and the UK Department of Trade and Industry as well as the FWF, Vienna, Austria.

References

---

[1] G.F. Matthews, *Plasma Physics and Contr. Fusion* **31**, No. 5 (1989) 853
[2] G.F. Matthews, *J. Nucl. Mater.* **176&177** (1990) 1032
[3] G.F. Matthews, D. Elder, G.M. McCracken et al., *J. Nucl. Mater.* **196-198** (1992) 253-257
[4] ITER physics basis editors, et al., *Nuclear Fusion* **39**, No.12 (1999) 2137-2664

Negative Ion Spectroscopy of CF_4 and CF_3Cl

S W J Scully, R A Mackie, R Browning, K F Dunn and C J Latimer

Department of Physics, The Queen's University of Belfast, Belfast BT7 1NN, N Ireland

The photo-ion pair formation process in CF_4 and CF_3Cl have been studied in the VUV between 20 and 55 eV. F^-, F_2^-, Cl^-, Cl_2^- and FCl^- efficiency curves have been measured and the role of various excited and superexcited states investigated. Intravalence transitions, shape resonance states and two electron processes play an important role in the photoabsorption process.

1. INTRODUCTION

Carbon tetrafluoride (CF_4) is a basic fluoromethane and is of interest because of its chemical stability, high degree of symmetry, and the unusual dissociative and optical emission behaviour of its cationic states [1-3]. CF_4 is introduced into the atmosphere by its widespread use as a fire extinguisher and it is also used in the plasma etching of semiconductor materials. Freon molecules, such as CF_3Cl, have been widely used in industry, for example as refrigerants and aerosol propellants and it is recognised that these compounds are responsible, via photochemical mechanisms, for the depletion of the earth's ozone layer. Rydberg and superexcited molecular states which have several different decay channels, including dissociative autoionization and ion-pair formation, can play an important role in the photoabsorption processes of such molecules. In the present work negative ion spectroscopy, which yields information about the precursor excited molecular states, has been used to study CF_4 and CF_3Cl.

2. EXPERIMENTAL APPROACH

These experiments were carried out at the Daresbury Laboratory (UK) synchrotron on beamline 5D, which can provide photons in the energy range 20 – 210 eV. The photons entered the interaction region, via a 2.4mm diameter glass capillary, where they collided with a narrow gas jet. Negative ions produced by photoabsorption were swept from the collision region by a potential difference across two grids. The ions were then focussed, by an electrostatic lens, into a triple quadrupole mass spectrometer. The data was corrected for higher order radiation. The collision region was kept at a low pressure to avoid secondary collision effects and the quadrupole mass spectrometer was differentially pumped to reduce noise from stray electrons.

3. RESULTS AND DISCUSSION

Figures 1 and 2 show the negative ion yield curves, F^- and F_2^- for CF_4, and F^-, F_2^-, Cl^- and FCl^- for CF_3Cl respectively. F^- produced after photoexcitation of CF_4 has been measured by Mitsuke *et al* [4] in the photon energy range 11-31 eV, while F^- and Cl^- from CF_3Cl have been observed by Schenk *et al* [5] in the energy range 8–25 eV. The negative ion yield curves for the other fragments are presented here for the first time. Some of the resonance peaks can be attributed to valence Rydberg transitions. A term value T_R for the Rydberg state is estimated using the formula

$$T_R = \frac{R}{(n-\delta)^2}$$

where R denotes the Rydberg energy (13.6 eV), n the nominal principal quantum number and δ the quantum defect. T_R can then be used to identify the resonance peak energy $E_{h\nu}$ from

$$E_{h\nu} = I_P - T_R$$

where I_P is the vertical ionization potential for the molecular parent ion formed by removal of the electron from the initial orbital.

3.1 CF_4

The ground state electronic configuration of the CF_4 molecule (in T_d symmetry) is given by

$$(1a_1^2 1t_2^6)(2a_1^2)(3a_1^2 2t_2^6)(4a_1^2 3t_2^6 1e^4 4t_2^6 1t_1^6) \quad {}^1A_1$$

where the parentheses denote the F1s , C1s , inner-valence and outer-valence orbitals respectively [7]. The bonding orbitals are $4a_1$ and $3t_2$, while 1e, $4t_2$ and $1t_1$ are of fluorine lone pair character [8]. In addition there are unoccupied (virtual) valence antibonding orbitals $5a_1^0$ and $5t_2^0$ which have $(C\text{-}F)^*$ character [9]. From combined HeI and HeII PES studies [10, 11] the vertical ionization potentials of the outer valence molecular orbitals $1t_1$, $4t_2$, 1e , $3t_2$ and $4a_1$ are known to be 16.2, 17.4, 18.5, 22.12, and 25.12 eV respectively, corresponding with ion states $\tilde{X}\ {}^2T_1$, $\tilde{A}\ {}^2T_2$, $\tilde{B}\ {}^2E$, $\tilde{C}\ {}^2T_2$ and $\tilde{D}\ {}^2A_1$. The inner valence molecular orbitals $2t_2$ and $3a_1$ yield vertical ionization potentials of 40.3 and 43.8 eV [12, 13] corresponding to the ion states $\tilde{E}\ {}^2T_2$ and $\tilde{F}\ {}^2A_1$.

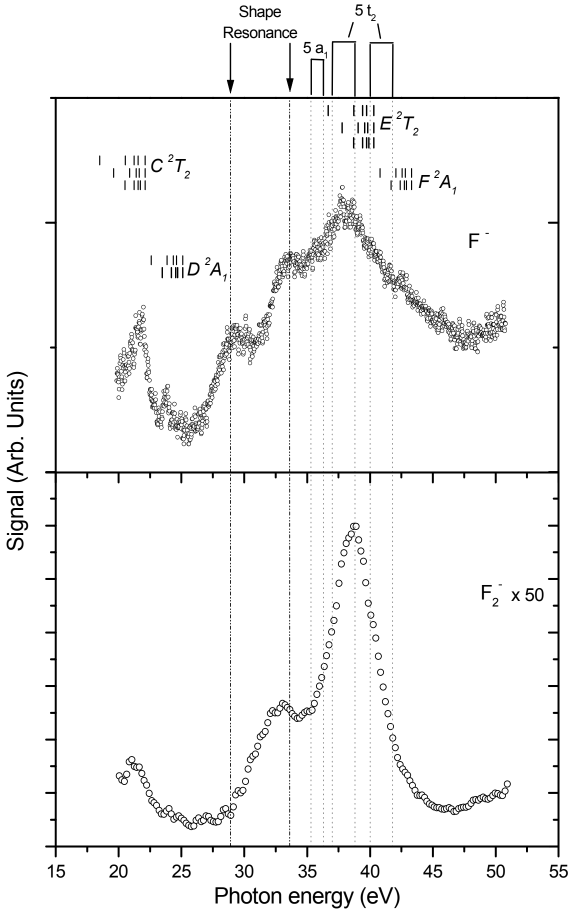

Figure 1: Negative ion yields from CF_4. Solid lines represent Rydberg states converging on ionic states of the molecule, dash dot lines represent shape resonance or quasibound states, and dotted lines represent virtual orbital limits taken from EELS studies [5]. Relative to F^- yield.

The F^- yield curve (figure 1) from 20 → 52 eV was measured with a resolution of ~50 meV, and the F_2^- yield was measured with a resolution of ~200 meV. The process of producing F^- from CF_4 is

$$CF_4\ (\tilde{X}\ {}^1A_1) + h\nu \rightarrow CF_4^{**} \rightarrow F^- + (CF_3^+)^*$$

where CF_4^{**} denotes the superexcited or doorway state which is involved in ion pair formation. The structure in the first peak has also been observed by Mitsuke *et al* [4] and attributed to two different types of vibrational progression lying on a broad background. The first is a vibrational progression of the Rydberg state CF_4^{**} ($3t_2 \rightarrow 4pt_2$ ${}^1T_2$) converging to the third excited ionic state CF_4^+ ($\tilde{C}^2$ T_2). The second vibrational progression is tentatively assigned to two Rydberg states, CF_4^{**} ($3t_2 \rightarrow 5pt_2$ ${}^1T_2$) and CF_4^{**} ($3t_2 \rightarrow 6pt_2$ ${}^1T_2$) converging to CF_4^+($\tilde{C}^2$ T_2) which overlap with each other. The resonances between 24 and 26 eV are in agreement with those observed previously [4]. These have been attributed to Rydberg states converging to the CF_4^+ ($\tilde{D}^2$ A_1) ionic state, $4a_1 \rightarrow 3d$, $3t_2 \rightarrow 4pt_2$ and $4a_1 \rightarrow 5pt_2$. We also see evidence of these Rydberg states in the F_2^- yield between 20 and 26 eV. A comparison with earlier work suggests that the F^- peak at 21.5 eV has a cross section of $\approx 5\mathrm{x}10^{-22}$ cm^2.

Above 26 eV the F^- yield curve has not been observed before and it can be seen from figure 1 that there is a marked increase in F^- production. Rydberg progressions converging on CF_4^+ $(\tilde{E}\ ^2T_2)$ and CF_4^+ $(\tilde{F}\ ^2A_1)$ have been marked on figure 1 and show possible correlation with the final large peak in the case of CF_4^+ $(\tilde{E}\ ^2T_2)$. However discrete Rydberg resonances associated with these inner valence electrons may not be observed since orbital degeneracy leads to apparent band areas in the photo-electron spectra [14]. It has also been shown theoretically [15] that ionisation from the F2s ($3a_1$ and $2t_2$) molecular orbitals cannot be understood on a one particle basis. Therefore ionisation will lead to population of a number of mixed “shake up” states that have the same symmetry as the one-electron transition. A spread of final ionized states will therefore be obtained which will give rise to neutral Rydberg states which may predissociate into the ion-pair channel. These two hole states may therefore explain the broad nature of the peak around 37 eV. However, it is also possible that in the 33-42 eV energy region promotion of the inner valence electrons into antibonding virtual orbitals is leading to negative ion production. Electron energy loss [5] has identified ranges of term values for the $5a_1$ and $5t_2$ unoccupied orbitals which overlap well with the broad peak at $\approx$37 eV for both F^- and F_2^-.

None of the processes suggested above can describe the features seen in both negative ion yields between 26 and 35 eV. We propose that these features are the result of promotion of the $4t_2$ and $3t_2$ electrons into shape resonance states. A shape resonance state is a quasi bound state in the continuum where the outgoing electron is confined by a potential barrier which results from the interplay of attractive and repulsive forces in the molecule. β parameter measurements [14, 16, 17] suggest the presence of shape resonances, in CF_4, between 10 and 15 eV above the vertical ionization potential for the outer valence t_2 orbitals. The two broad peaks in F^- observed here are $\approx$11.5 eV above the respective ionization potentials (see figure 2). The absence of one of these peaks in F_2^- may result from the different character of the $3t_2$ (bonding) and $4t_2$ (F lone pair) orbitals.

The large F^- continuum beyond the final valence electron I_p at 43.8 eV is evidence that two electron processes play an important role in photoabsorption. Negative ion formation involving two electron processes has been reported previously in SO_2 [18]. The broad features between 26 and 42.5 eV may also result from ionic Rydberg states converging on the dicationic states of the parent ion. Auger-electron and double-charge-transfer spectroscopy techniques [19] have been used to identify a number of doubly ionized states in CF_4. These results show a large number of dicationic states in the energy range of interest, starting at 37.98 eV. Double photoionization/fragmentation studies [20] determined the thresholds for the ion-pair formation of CF_4^{2+} into $F^+ + CF_3^+$ (37.6 eV), $F^+ + CF_2^+$ (42.4 eV), $F^+ + CF^+$ (47.5 eV), and $C^+ + F^+$ (62.0 eV) and these correlate with calculated two-hole states of CF_4 [21]. These ionic Rydberg states seem unlikely due to the differences between the F_2^- and F^- yields above 43.8 eV, where two electron processes definitely lead to negative ions.

3.2. CF_3Cl

The ground state electronic configuration of CF_3Cl (in C_{3v} symmetry) is given by

$$(1a_1^2)(2a_1^2 1e^4)(3a_1^2)(4a_1^2)(5a_1^2 2e^4)(6a_1^2 3e^4 7a_1^2)(8a_1^2 4e^4 9a_1^2 5e^4 6e^4 1a_2^2 10a_1^2 7e^4) \quad {}^1A_1$$

where the parentheses denote the Cl1s, F1s, C1s, Cl2s, Cl2p, inner-valence and outer-valence orbitals respectively [9]. In addition there are unoccupied (virtual) valence antibonding orbitals $11a_1^0$, $8e^0$ and $12a_1^0$ which have (C-Cl)*, (C-F)* and (C-F)* character respectively [9]. The ionization potential values for orbitals in the energy region of interest ($9a_1$, $4e$, $8a_1$, $7a_1$, $3e$ and $6a_1$) are 20.2, 21.2, 23.8, 26.9, 40.0 and 42.5 eV respectively [6].

The F^- and Cl^- yield curves (figure 2) from 20 → 52 eV were measured with a resolution of ~50 meV, whereas the F_2^- and FCl^- yields were measured with a resolution of ~200 meV. The main peak in F^- at ≈21 eV has a cross section of approximately 2×10^{-21} cm^2 which is a factor of 4 increase on that seen in CF_4. However the structure closer to the inner valence region is smaller than that around 21 eV in stark contrast to what was observed in CF_4. F_2^- has a similar cross section to that seen in CF_4 which is probably the result of the mesomeric states of these molecules which have substantial ionic character due to the high electronegativity of the ligands. The structure observed in the 20-25 eV region for all negative ions appears to be a result of overlapping Rydberg series converging on the ionic states that result from $7a_1$ and $8a_1$ ionization. Rydberg states assigned using the method of Gilbert *et al* [22] have been marked on figure 2. The Rydberg series involving the $8a_1$ electron appears for all negative ions except F_2^-. This may be due to the $8a_1$ electron having C-F bonding character. This argument could be supported by the increase in F_2^- when the Cl3s non-bonding electron is excited into a Rydberg state, which allows time for the molecule to distort and form the F_2^- fragment. Structure is observed in all channels which cannot be accounted for by predissociating Rydberg states. This structure, represented most clearly in the FCl^- fragment by the peaks at ≈29 eV and ≈37.5 eV, is believed to be the result of neutral transitions of valence electrons into shape resonance states and unoccupied valence orbitals. Zhang *et al* [9] have observed a shape resonance in CF_3Cl at 2.81 eV above the ionization potential of the C1s electron. It seems that this resonance state is responsible for the feature at ≈29 eV which is 2.1 eV above the $7a_1$ ionization potential. In addition they have also observed virtual orbitals with term values; $7b_1+14a_1$ 2.8-3.9 eV and $13a_1+9b_2$ 5.3-6.7 eV. The ranges of these virtual orbitals have been marked on figure 2 and show good overlap with the structure observed. Again, as in CF_4, we also see substantial negative ion signal after the last valence electron ionization potential suggesting two electron processes.

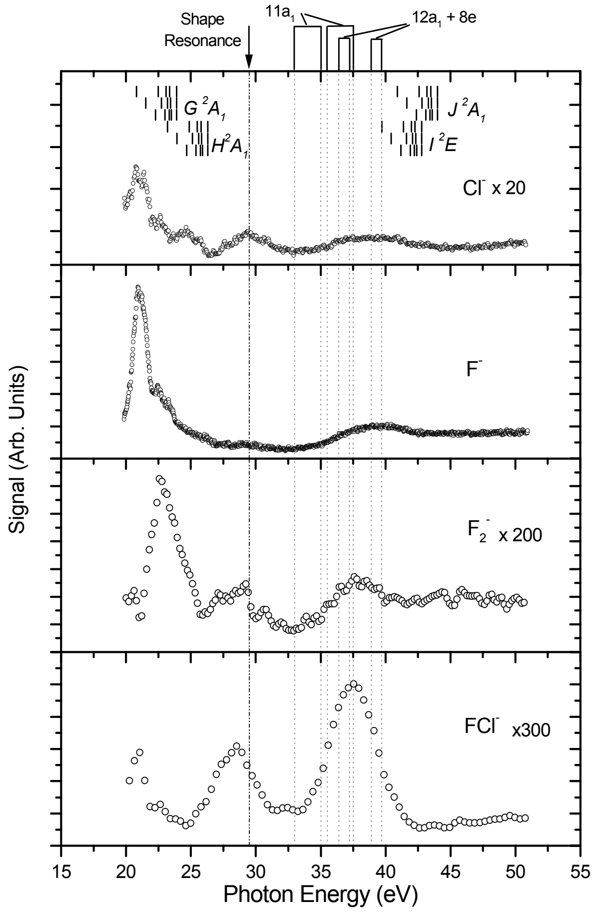

Figure 2: Negative ion yields from CF_3Cl. Solid lines represent Rydberg states converging on ionic states of the molecule, dash dot lines represent shape resonance or quasibound states, and dotted lines represent virtual orbital limits taken from EELS studies [5]. Relative to F^- yield.

References

---

[1] R.P. Tuckett, Chem. Soc. Rev. **19** (1990) 439

[2] J.C. Creasey, *et al*, Chem. Phys., **174** (1993) 441

[3] P.A. Hatherly, K. Codling, D. M. Smith, R.P. Tuckett, K.R. Yoxall and J. F. M. Harts, Chem. Phys., **174** (1993) 453

[4] K. Mitsuke, S. Suzuki, T. Imamura and I. Koyano, J. Chem. Phys. **95** (1991) 2398

[5] H. Schenk, H. Oertel and H. Baumgärtel. Ber. Bunsenges. Phys. Chem. **83** (1979) 683

[6] W. Zhang, J. Cooper, T. Ibuki and C. E. Brion, Chem. Phys., **151** (1991) 343
[7] W. Zhang, G. Cooper, T. Ibuki and C. E. Brion, Chem. Phys. **137** (1989) 391
[8] F. O. Gottfried, L. S. Cederbaum and F. Taratelli, J. Chem. Phys. **104** (1996) 9754
[9] W. Zhang, T. Ibuki and C. E. Brion, Chem. Phys. **160** (1992) 435
[10] C. R. Buncle, M.B. Robin and H. Basch, J. Chem. Phys. **53** (1970) 2196
[11] D. R. Lloyd and P. J. Roberts, J. Electron Spectrosc. Relat. Phenom. **7** (1975) 325
[12] K. Siegbahn, *et al*, *ESCA Applied to Free Molecules*, North Holland, Amsterdam, 1969
[13] M. S. Banna, B. E. Mills, D. W. Davies and D. A. Shirley, J. Chem. Phys., **61** (1974) 4780
[14] I. Novak, A.W. Potts, F. Quinn, G. V. Marr, B. Dobson, I. H. Hillier and J. B. West, J. Phys. B **18** (1985) 1581
[15] R. Cambi, *et al*, Chem. Phys. Lett. **90** (1982) 445
[16] C. M. Truesdale, *et al*, J. Chem. Phys. **80** (1984) 2319
[17] T. A. Carlson, *et al*, J. Chem. Phys. **81** (1984) 3828
[18] G. Dujardin, L. Hellner, B. J. Olsson, M. J. Besnard-Ramage and A. Dadouch, Phys. Rev. Lett. **62** (1989) 745
[19] W. J. Griffiths, *et al*, Chem. Phys. **173** (1993) 109
[20] K. Codling, L. J. Frasinski, P. A. Hatherley, M. Stankiewicz and F. P. Larkins, J. Phys. B **24** (1991) 951
[21] F. P. Larkins and L. C. Tulea, J. Phys. (Paris), Colloq. C9(12) **48** (1987) 725
[22] R. Gilbert, P. Sauvageau and C. Sandorfy, J. Chem. Phys. **60** (1974) 4820

Femtosecond and subfemtosecond time-resolved photoelectron spectroscopy dynamics

P. Šiffalovič, M. Drescher and U. Heinzmann

Fakultät für Physik, Universität Bielefeld, D-33615 Bielefeld

M. Hentschel, R. Kienberger, Ch. Spielmann, G.A. Reider, N. Milosevic, T. Brabec, P. Corkum and F. Krausz

Institut für Photonik, T.U. Wien, A1040 Wien

The contribution presents a recently performed visible-pump/extreme ultraviolet (EUV) probe spectroscopy experiment using spectrally selected high harmonics of intense laser pulses for the study of electronic dynamics on semiconductor surfaces. Transient changes of surface photo voltage at the p-GaAs(100) surface are observed after photoexcitation with 3.1 eV femtosecond laser pulses. The time evolution of the band-bending is probed by measuring the kinetic energy shifts of the Ga-3d core level photoelectrons after excitation with 70 eV femtosecond EUV pulses. Carrier transport from the bulk to the surface is observed to occur within 400 fs after photoexcitation while a subsequent relaxation is determined as evolving on a picosecond time scale. The technique to isolate an individual higher harmonic of the pulse without loss of its fs-time structure and to focus the monochromatized radiation on the target makes use of specially designed nanometer multilayers as narrow band EUV mirrors.

The same technique has been used to realize the first attosecond metrology experiment [1]. The work demonstrates – for the first time – the generation, characterization and use of isolated bursts of electromagnetic radiation being confined in time to less than 1 femtosecond. For reasons of cross-comparison, one period of visible light is 2 fs. In order to gain access to the attosecond regime, high order ($n > 55$) harmonics of near infrared pulsed (7 fs) laser radiation have been filtered out at 90 eV by means of EUV multilayer optics. Theoretical models predict the formation of a light packet much shorter than the generating laser pulse. The main progress of our work is the development and realization of a visible/EUV cross-correlation scheme which provides sub-laser-cycle temporal resolution to test this theoretical prediction experimentally. The kinetic energy of 4p valence photoelectrons from free Krypton atoms ionised by the EUV radiation in the presence of the laser field was used as the cross-correlation signal. In this photoionization experiment which looks at the energetic distribution of the photoelectron at the instant of its creation or shortly later the measured evolution of the kinetic energy spectrum as a function of the delay between the EUV and the laser pulse therefore represents a laser field/EUV intensity cross correlation. Thus, the high harmonic pulse has actually been confined to 650 ± 150 attoseconds.

References

---

[1] M. Hentschel, R. Kienberger, Ch. Spielmann, G.A. Reider, N. Milosević, T. Brabec, P. Corkum, U. Heinzmann, M. Drescher and F. Krausz, *Nature* **414** (29. Nov.), 509 (2001)

Plasma analysis of different TiN PVD processes at various process parameters

G.N. Strauss[1], **S. Schlichtherle**[1], **H.K. Pulker**[1], **M. Meyer**[2], **H. Jehn**[3], **M. Balzer**[3] ,
C. Misiano[4], **V. Silipo**[4]

[1]Univ Innsbruck (A), (I), [2]DaimlerChrysler (D), [3]FEM (D), [4]CeTeV (I)

Summary:

TiN coatings of some microns in thickness were deposited by different reactive plasma deposition technologies (Magnetron Sputtering Magnetically Assisted, Arc Source Ion Plating, Sputter Ion Plating Plasma Assisted) on various metal parts. The experiments were carried out in specially designed plants under variable vacuum and plasma conditions. The plasma properties of the different processes were investigated by mass spectrometry and the energy distribution of process relevant particles was additionally determined.

The aim of this work was to find proper processes and conditions for a reliable low cost deposition of hard coatings at relatively high gas pressures.

The investigations were supported by the European Union in the TIPCOAT-Project: Brite EuRam BE-3815/Contract BRPR-CT97-0397

Keywords:

Tribological coatings, Magnetron Sputtering, Ion plating, Arc source, Plasma parameters, TiN

Introduction:

The growing demand for enhanced performances and durability for mechanical components, together with an increased use of steel, light metals and workable alloys have lead, in the last decades, to a wider use of coatings for hardening, protection and low friction. The best results in this area have been found with PVD (Physical Vapour Deposition) techniques.

The industrial target of this work was the development of a new PVD (Physical Vapour Deposition) process and plants, by Ion Plating Plasma Assisted Technologies (IPPA). For this purpose the alternative PVD-processes had to be modified to coat 3D complex components, at costs and at substrate temperatures lower than 250 °C. One goal was to coat locally, near atmospheric pressure, large and heavy forming tools primarily for the car-component industry.

Three main objectives were forseen:

1) Set-up of an isotropic deposition process for the realisation of tribological coatings, even on surface details not in optical view of the sources.
2) Set-up of a plant operating near atmospheric pressure for only local coating of large mechanical components
3) Lowering of coating costs through a dramatic shortening of cleaning and deposition times.

In order to reach these industrial objectives, two innovative solutions were studied concerning I.P.P.A.:

- “High Pressure Ion Plating”;
- “Multi-Plasma Ion Plating”.

“High Pressure Ion Plating” in the range up to 0,1 mbar to obtain high isotropy in coating. “Multi-Plasma Ion Plating” to enable an indepentend control of the plasma for ionisation of the vapourised material and of the substrate bias in the high pressure process. In particular the generated multi plasmas and their influence on layer properties have been studied.

2. Experiments / Results

Arc sources and planar magnetrons without and with multiplasma configuration have been used at different working pressures to coat unheated metal substrates at variable distances between 8 and 25cm.

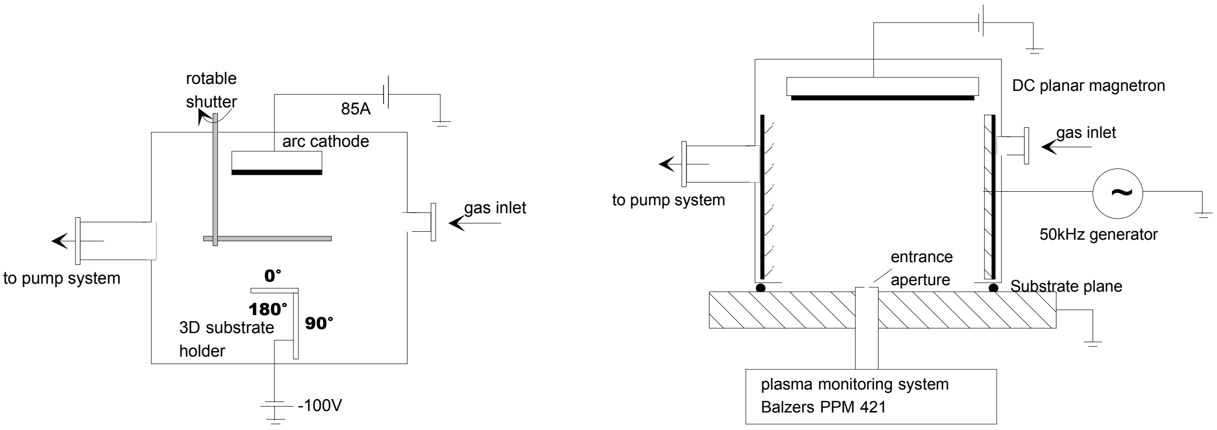

a) b)

Fig.1: a) Schematic of an arc source ion plating plant (with the static standard substrate holder)
b) Schematic of a planar magnetron ion plating plant (with a mass spectrometric plasma monitoring system). The plant can be used as sputter ion plating plasma assisted, or by insertion of a magnetic cylinder as dc magnetron sputtering system magnetically assisted.

Under different working conditions the vapour species of the individual coating material sources was analysed carefully by mass spectrometric measurements with a plasma monitor. The results for arc source ion plating are shown in Fig.4 and for sputtering in Figs 2 and 3.

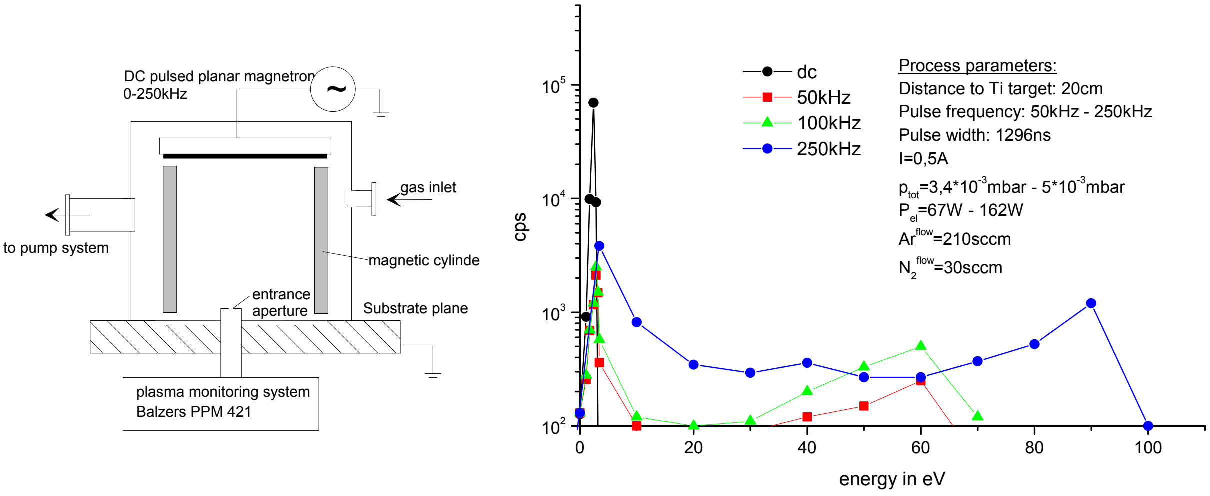

a) b)

Fig.2: a) Schematic of a magnetically forced dc pulsed plasma of a planar magnetron sputtering source.
b) According energy spectrum of the Ar+ ions. As can be seen, with increasing frequency of the current regulated generator the amount and the energy of the ions is strongly increased.

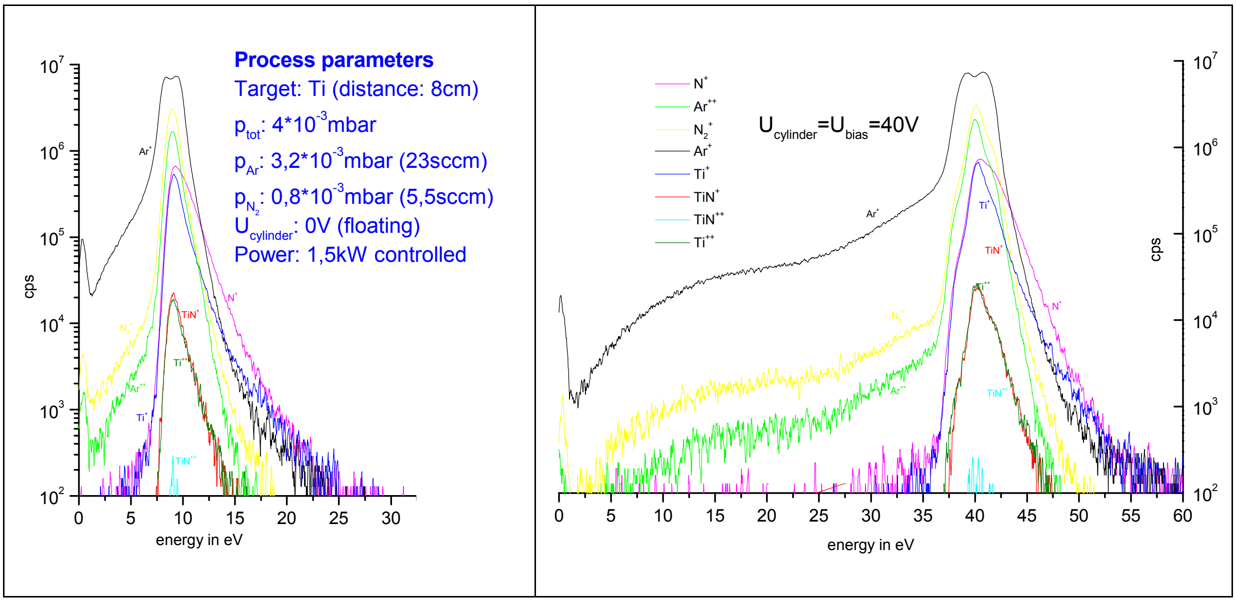

Fig.3: Energy spectrum of all ions of the TiN process in medium frequency biased magnetron sputtering (Fig.1b). Left: without bias (floating), right: 40V medium frequency (50kHz) bias. As can be seen with bias ion population and energy again is increased.

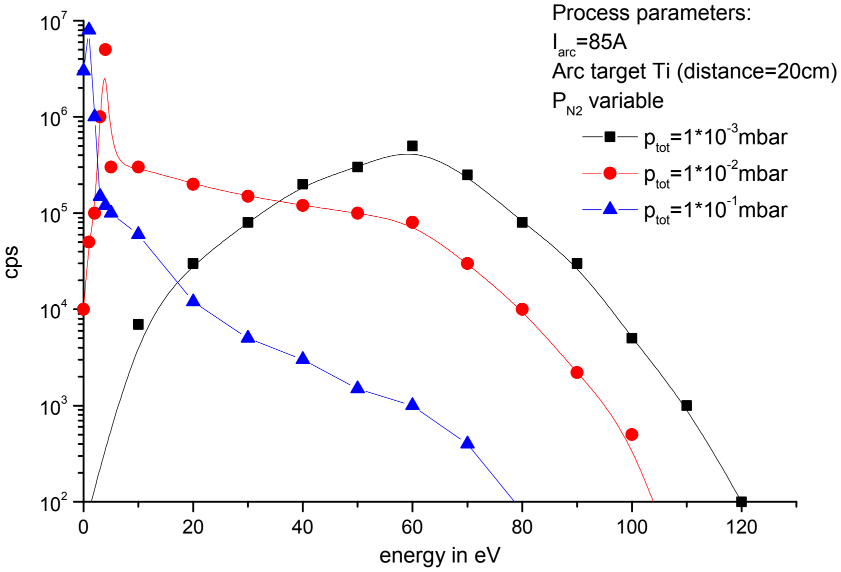

Fig.4: Energy spectra of the Ti+ ions in the reactive TiN arc source ion plating process (Fig. 1a) at various N_2 gas pressures (1*10^{-3} mbar to 1*10^{-1} mbar) at constant arc current (Ti cathode distance 20cm). It is remarkable how many energetic Ti+ ions were found even at 10^{-1} mbar gas pressure!

From Fig.3 it can be seen that in medium frequency forced dc magnetron sputtering at low pressure the amount of Ar^+ ions is higher than that of Ar^{2+}. Also N_2^+ is higher than N^+, and there is no N_2^+ . Ti^+ is larger than Ti2$^+$, and TiN^+ larger than TiN^{2+}.

From the energy spectra of all ions of arc source ion plating it was found that the intensity of N^+ is much higher than that of N_2^+ . TiN^+ could also be detected. The intensity of TiN^+ increased with rising N_2 - gas pressure. The intensity of TiN^{2+} was even 10 times higher than that of Ti^+.

At medium gas pressure in the 10^{-3} mbar regime the investigated coating methods and their variants resulted in films of proper quality but of differences in thickness and hardness dependend on gas pressure, bias voltage, and on impact angle of the coating material.

Sputter deposited films have a relatively smooth surface. Arc deposited films show more or less droplets, that are macroparticles emitted from the arc cathode. The degree of source material poisoning (nitride formation) has some effect on the number and size of droplets produced such that with increasing degree of arc cathode poisoning, and this happens at higher N_2-gas pressure, fewer and smaller droplets result.

Mainly the mechanical film properties as hardness, adherence and abrasion resistance are influenced by many parameters, e.g. substrate material, surface roughness, surface pre-treatment, temperature, and so on which are not considered in detail in this presentation.

Increasing the gas pressure improved in all cases the 3D coating uniformity. However, an increase of the gas pressure from the 10^{-3} mbar region to about 10^{-2} mbar decreased more or less strong the energy and modified the energy distribution of the coating material vapour species of both, the arc source and the various magnetron sputter variants.

An increase in the gas pressure to about 10^{-1}mbar decreased, the energies of the sputtered coating material so strong that no high performance films could be deposited under such conditions. In arc-source ion plating, however, the amount of coating material and its particle energy is, even at about 10^{-1} gas mbar pressure, high enough to form proper films on unheated substrates during reasonable times. In order to measure the insitu substrate current density in the cathodic arc source deposition arrangement, in some experiments, the substrate holder was replaced by an ion current probe.

3. Discussion/Conclusions

The magnetically forced and medium frequency pulse biased dc magnetron sputter deposition variants, operating in the 10^{-3} mbar gas pressure range, showed a relatively large amount of single and double charged positive ions with kinetic energies up to 55 and 95eV, as consequence of the applied modifications.

Cathodic arc deposition, in the same gas pressure range of 10^{-3} mbar, showed a very high number of such ions with energies up to more than 100eV, depending on the value of the applied arc current.

However, at constant distance between source and substrate the higher gas pressure increases also the number of energy reducing collisions of the coating-material vapour-species with the gas molecules.

The arc source process, even when performed at high gas pressures of about 10^{-1} mbar, showed a remarkable amount of ions with energies up to 75eV resulting in high performance TiN films of quite proper 3D homogeneity. The arc source technique is able to increase film thickness uniformity up to 3 times with respect to the traditional coatings if the samples are mounted in a way that they do not influence each other.

Table 1: Characteristic data of the different reactive deposition processes

PROCESS	PARAMETERS	DEGREE OF IONISATION	PRINCIPAL IONS DETECTED	ENERGY RANGE
ARC EVAPORATION	Low pressure TiN deposition $pN_2 = 4*10^{-3}$mbar Arc current = 85A Substrate bias = floating	high	N^+ Ti^+ Ti^{++} N_2^+ TiN^+	0 – 80eV 0 –110eV 0 – 80eV 0 – 50eV 0 –45eV
ARC EVAPORATION	Medium pressure TiN deposition $pN_2 = 1,3*10^{-2}$mbar Arc current = 85A Substrate bias = floating	high	N^+ Ti^+ Ti^{++} N_2^+ TiN^+	0 – 80eV 0 –110eV 0 – 80eV 0 – 40eV 0 –35eV
ARC EVAPORATION	High pressure TiN deposition $pN_2 = 1*10^{-1}$mbar Arc current = 85A Substrate bias = floating	high	N^+ Ti^+ Ti^{++} TiN^+	0 – 20eV 0 –80eV 0 – 40eV 0 –15eV
DC Magnetron Sputtering	Low pressure TiN deposition $1,5*10^{-3}$mbar	low	N^+, N_2^+, Ar^+, Ti^+ ,TiN^+	0 – 30eV
Magnetron sputtering	Medium pressure TiN deposition $1,5*10^{-2}$mbar	low	N^+, Ar^+, Ti^+	0 – 2eV 0 – 0,5eV 0 – 2eV
Medium frequency forced DC Magnetron sputtering	Low pressure TiN process Ar: $3,2*10^{-3}$mbar N_2: $0,8*10^{-3}$mbar	medium - low	N^+, N^{++}, N_2^+, Ar^+, Ar^{++}, Ti^+, Ti^{++},TiN^+	Floating: 0 – 30eV $U_{Cylinder}$=80V Ar^+, Ar^{++}, Ti^+: 0 –100eV Ti^{++}: 75 – 90eV

Plume dynamics in the laser ablation of transition metal carbides

R. Teghil, L. D'Alessio

Dipartimento di Chimica, Università della Basilicata, via N. Sauro 85, 85100 Potenza, Italy

A. Giardini Guidoni, A. Santagata

CNR Istituto Metodologie Inorganiche e Plasmi, Sez.Potenza, via S. Loja, Tito Scalo, Italy

1. Introduction

Carbides of the group 4 elements are refractory materials widely used as coatings in the high temperature technology field for their chemical-physical properties. In fact these compounds present a very high thermal stability and a noticeable resistance to corrosion [1, 2]. Various deposition techniques, such as chemical vapour deposition, plasma spraying and ion sputtering, are commonly used to obtain carbides thin films but we have focused our attention on pulsed laser ablation deposition (PLD). PLD technique is currently employed for its capability to evaporate and to deposit every kind of material and it has shown to be particularly useful for the deposition of coating of refractive materials with very high melting temperature [3]. In spite of its good performances as deposition technique, PLD suffers from the incomplete knowledge of the mechanisms leading both to the vaporisation of the material and to its deposition on the substrate. In this paper we will summarise the results of the analysis of the gas phase produced by laser ablation of titanium, zirconium and hafnium carbides, with the aim to elucidate the ablation mechanism in this three systems.

2. Experimental

The experimental apparatus has been already described [4]. It consists of a vacuum chamber equipped with quartz windows for laser beam inlet and in-situ optical analyses, heatable substrate holder and rotating target support. The limiting pressure inside the chamber was 1.0×10^{-4} Pa. The laser source was a frequency doubled Nd:YAG laser ($\lambda = 532$ nm, $\tau = 10$ ns, 10 Hz repetition rate) impinging on the target with an incidence angle of 45 degrees

The characterisation of the gas phase was carried out by emission spectroscopy (OMA-ICCD system, EG&G, coupled to an ARC50 spectrograph by a bundle of 20 optical fibers), optical imaging (ICCD camera, EG&G) and time of flight mass spectrometry (LAMMA 500, Leybold). The spatial and temporal resolutions of the ICCD systems were 150 μm and 5 ns respectively.

3. Results and discussion

The ablation rate, measured through the target weight loss, can give an indication on the ablation mechanism involved in the laser-material interaction. Zirconium and hafnium carbides show a linear dependence from laser fluence [4, 5] while titanium carbide has a peculiar behaviour. In fact the plot is not linear and can roughly divided into three zones, I, II, and III that in our hypothesis correspond to different ablation mechanisms [6]. In particular zone I corresponds to a high temperature thermal vaporisation and zone II to a real ablation, while at higher laser fluence (zone III) the laser spallation mechanism leads to the increase of the ablation rate. On the contrary the linear plot obtained for ZrC and HfC should indicate a single ablation mechanism.

The X-ray analyses of the films deposited on silicon substrates indicate that the films are crystalline in the whole temperature range at middle and high fluences for titanium carbide, while in the case of zirconium and hafnium carbides the crystallinity is fluence and temperature independent. The composition from XPS shows that the stoichiometry of the titanium carbide films is TiC_2 in the fluence zone I and TiC in the zones II and III [6], while for the other carbides one obtains ZrC and HfC stoichiometry irrespective of the laser fluence [4, 5].

Time of flight mass spectrometry, performed on plasma (plume) produced by the interaction of the laser radiation with the target, confirms the differences between TiC and the other two systems. In fact at laser fluence lower than 3 J/cm^2 (zone I) the main component of the TiC plasma, together with metal and carbon, is TiC_2 but its importance decrease very rapidly with the increasing of the fluence (zones II and III). On the other hand the dicarbide is present in the gas phase from ZrC and HfC, but only in a small quantity whatever the fluence might be [4, 5]. It is important to note that the metal dicarbide molecule is present in a small amount in the gas phase produced by conventional thermal equilibrium vaporisation [7] and in that conditions its abundance grows with the increasing of the temperature.

The ICCD imaging of the total emission of plasma produced from the three different targets evidences strong differences between the shape of the plume of TiC and those of ZrC and HfC. In fact at low laser fluence only one emission maximum is observed for all systems while at laser fluence higher than 3 J/cm^2 a second emission maximum appears in the case of TiC, becoming more evident with the increase of fluence [5, 8]. The analysis of the emitting species, resolved in space, frequency and time, has allowed to have indications about the plume composition and dynamics. The main components of the carbide plumes are metal and carbon atoms, both neutral and ionised, but double ionised (Ti^{++}) particles are present only in the case of TiC. An example of the velocity distribution of the different species is reported in fig.1, where the velocity distribution curves for a) neutral and ionised hafnium, b) neutral and ionised titanium is shown. In the first case the velocities are 1.1 10^6 cm/s 1.5 10^6 cm/s, in the second 1.4 10^6 cm/s and 2.5 10^6 cm/s.

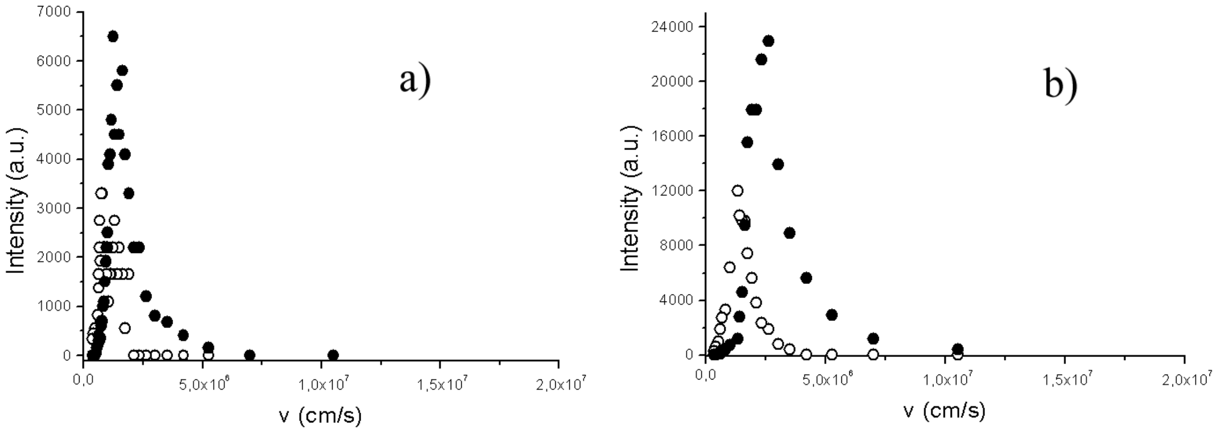

Fig. 1 Velocity distribution for: a) ● Hf^+, o Hf b) ● Ti^+, o Ti. The data were collected at 2.0 mm from the target.

It is evident from the data that while for zirconium and hafnium the metal ions and neutrals have quite the same velocity, in the case of titanium the situation is different and the velocity of the ions is higher. If we match our emission spectroscopy results with those obtained from ICCD imaging we could have an idea about the dynamic of the plume expansion for the different systems.

In Fig. 2 the results for TiC plume, obtained at high laser fluence, are shown. The two maxims found in the plume image are clearly related to neutral and ionised titanium atoms travelling with different velocities and this is in good agreement with the results found for other systems, such as aluminium nitride [3]. From these data the front of plume seems to be due to the emission of C^+ for all three carbides, while the comparable velocity of atoms and ions found for hafnium and zirconium could be considered responsible for the presence of a single maximum in the plume of these systems. The velocity of the double ionised atoms, found only in the TiC ablation, is about one order of magnitude higher than those of the neutral particles.

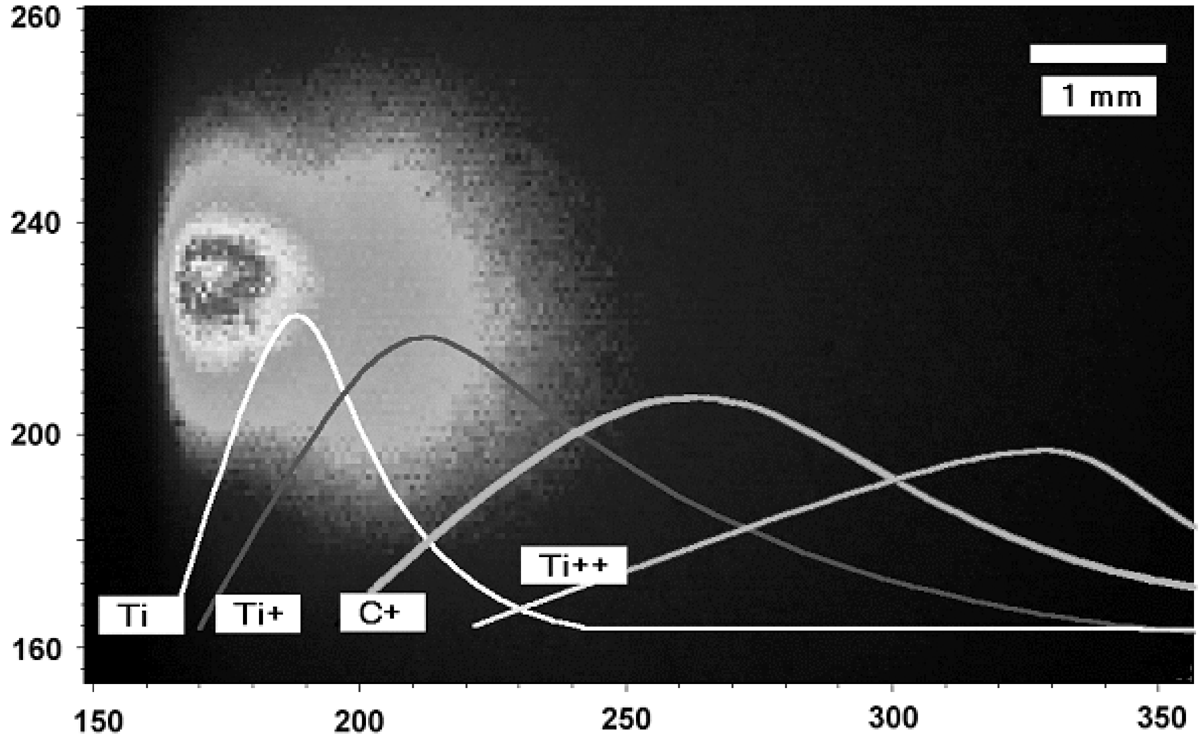

Fig.2 ICCD image of the plume produced by laser ablation of a TiC target at a fluence of 11 J/cm^2. The curves rapresent the velocity distribution of the different species obtained by frequency resolved emission spectroscopy. The values on the axis are in pixels.

The different gas phase characteristics for TiC, ZrC and HfC may be used to clarify the film growth mechanism for these materials. In fact the gas phase the composition seems to be the same for both systems at high fluences (zones II and III for TiC), the only difference between the three systems being the energy of the ionised particles. If we consider that, from TEM analysis, the first step of TiC growth is the formation of layers covering the whole substrate surface, while the ZrC and HfC growth starts with the formation of islands maintaining their structure also when the coverage is complete [9], the charged particles that certainly impinge on the substrate with higher energy compared to neutral ones, could interfere with the formation of large islands [10], that is the first step of columnar growth, favouring the layer-by-layer growth.

4. Conclusions

The data summarised in this work have shown that the characteristics of the gas phase produced by laser ablation of group 4 carbides can be correlated to the growth characteristics of the deposited films. In particular the different film growth structure, columnar for ZrC and HfC, layered for TiC, can be explained in terms of energy of neutral and charged particles present in the plasma.

References

---

[1] G. Georgeiev, N. Fescheschiev, D. Popov and Z. Uzuuov, *Vacuum* **36** (1986), 595.
[2] P.K. Ashwini, V. Kumar and J. Sarkar, *J. Vac. Sci. Technol. A* **7** (1989), 1488.

[3] A. Giardini Guidoni, A. Mele, T. M. Di Palma, C. Flamini, S. Orlando and R. Teghil, *Thin Solid Films* **295** (1997), 77.
[4] L. D’Alessio, A. Santagata, R. Teghil, M. Zaccagnino, I. Zaccardo, V. Marotta, D. Ferro and G. De Maria, *Appl. Surf. Sci.* **168** (2000), 284.
[5] R. Teghil, A. Santagata, M. Zaccagnino, V. Marotta, S.M. Barinov and G. De Maria, *Surf. Coat. Technol.* 00, 2001, 00.
[6] L. D’Alessio, A. M. Salvi, R. Teghil, V. Marotta, A. Santagata, B. Brunetti, D. Ferro and G. De Maria, *Appl. Surf. Sci.* **134** (1998), 53.
[7] C.A. Stern and F.J. Kohl, High. Temp. Sci. 2 (1990), 274.
[8] R. Teghil, L. D’Alessio, M. Zaccagnino, D. Ferro, V. Marotta and G. De Maria, *Appl. Surf. Sci.* **173** (2001), 233.
[9] R. Teghil, L. D’Alessio, A. Santagata, M. Zaccagnino, D. Ferro, V. Marotta and G. De Maria, Proc. 15th Int. Symposium on Plasma Chemistry, A. Bouchoule et al. Eds. Pag. 1989. 2001.
[10] H. Sankur, T.I. Cheung, *Appl. Phys. A* **47** (1988), 271.

Kinetics of ion/molecule reactions in Xe^++acetone system.

P.S. Vinogradov and A.S. Misharin.

Institute for Energy Problems of Chemical Physics, Russian Academy of Science.
Leninsky Prospect 38, bldg. 2, Moscow ,117829 Russia [*]

Abstract

A reaction of Xe+ ion with acetone and subsequent transformations of the product ions at a buffer gas pressure (He) of 1.1 Torr were studied by the flow reactor technique mass spectrometry. A kinetic scheme describing the evolution of the ionic composition has been determined. The rate constants of the key reactions involved in the scheme have been evaluated. A channel of the production of acetone cation in A state in a charge transfer reaction was observed. A production of slowly reacting isomer of the acetone cation in secondary reactions was detected. Its product in the reaction with acetone is the "nonprotonated dimer".

Introduction

A reaction of Xe^+ with acetone is interesting due to a very small difference in energy of the excited long living ***A*** state of the acetone cation and the $^2P_{3/2}$ state of Xe^+. The corresponding state to state charge transfer is exothermic only by 0.23 eV. The charge transfer channel in which the acetone cation is produced in the ground state is exoergic by 2.47eV and the internal excitation of the molecular cation is larger than the threshold of its dissociation (equal to 1.7 eV) in which CH_3CO^+ and CH_3 are produced.

Photoionization, photoelectron spectroscopy, photoelectron - photo ion coincidence (PEPICO) [1-4] and collisional induced decay [5-7] studies indicate on an important role of the production of the ***A*** state of acetone cation for subsequent fragmentation process. A detailed review on the subject is given in works [7-8].

The main goal of the present work was to check if the acetone cations are produced in the charge transfer and if the reactivity of the product ions differs from that measured by other authors when the ion is produced in different ways.

Subsequent chemical transformations of the other product (CH_3CO^+ ion) are of interest. A production of clusters of this ion with two (or more) molecules of acetone ligand may compete with the rearrangement processes resulting in the production of the protonated dimer of acetone and stable molecules $C_5H_8O_2$ (probably 2,4 pentanedione or other isomers). The rearrangement processes in ion clusters are not well studied up to date.

Experimental

The experiments were carried out using the flow technique reactor apparatus described elsewhere [9-10]. Primary Xe^+ ions were produced in the ionizer by an electron impact. The neutral adduct (acetone) was admixed to the flow via a capillary downstream. The concentration of acetone was a varied kinetic parameter. The length of the reaction region L was defined by the distance between the edge of the capillary and the orifice in the first sampling cone. The calculated value of the effective time of reaction was equal to $0.866\ 10^{-3}$ s.

---

[*] E-mail address for contacts pavel@chph.ras.ru and misharin@chph.ras.ru

Results

Fig. 1 presents the dependences of relative currents of the most intensive ions versus the product [A]t where [A] is the concentration of acetone. The kinetics of the production of ternary ions - $[CH_3CO^+CH_3COCH_3]$ (m/e=101), $CH_3COCH_3H^+$ (m/e=59) as well as the production of ions of the fourth generation - $[CH_3CO^+(CH_3COCH_3)_2]$ (m/e=159) and $(CH_3COCH_3)_2H^+$ was observed. It follows from Fig. 1 that the main product of the reaction of Xe^+ with acetone is CH_3CO^+ ion (m/e=43) while the other channel (production of the molecular ion of acetone (m/e=58)) is less intensive.

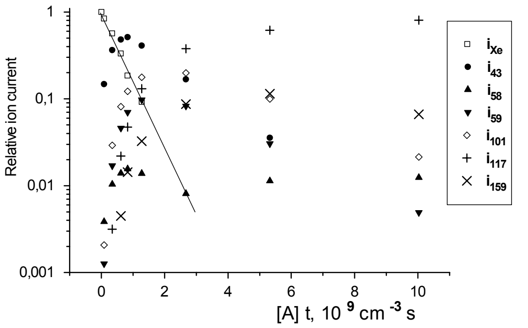

Fig. 1. Kinetic dependences of the relative currents for the most abundant ions. The solid line corresponds to the fit for a decay of the primary ion.

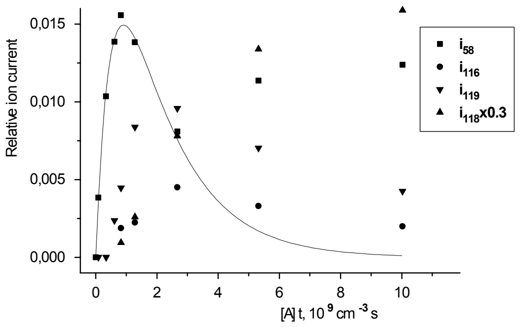

Fig. 2. Kinetic dependences of the relative currents for some small constituents in the ionic composition.

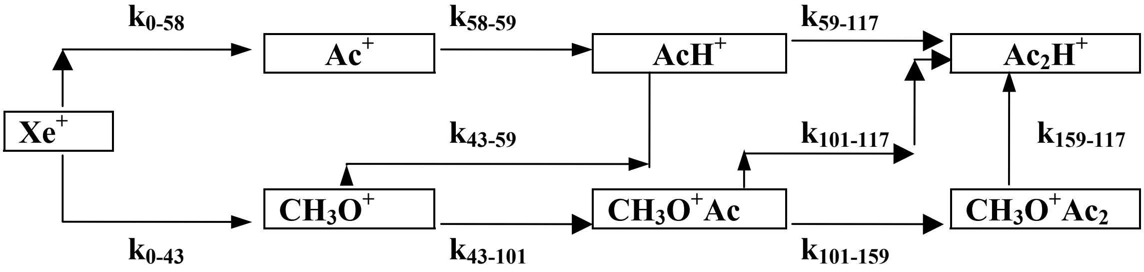

Fig. 3. The scheme of main pathways of the ionic transformations.

Kinetic dependences of some small constituents are presented in Fig. 2. The ions with m/e =116 are ascribed to the nonprotonated dimers of acetone (ion-radical), ions with m/e =118 to the protonated dimers of acetone with one ^{13}C atom, ions with m/e =119 to the clusters of the mixed composition $[CH_3CO^+CH_3COCH_3\ H_2O]$ formed due to the presence of water traces in the buffer gas.

The scheme of the main pathways of ionic transformations is shown in Fig. 3. The values of rate constants were determined from the fitting procedure. Expressions for ion currents were obtained from the solutions of differential equations of chemical kinetics for ionic concentrations in accordance with the given above scheme. The expressions were taken as fitting functions for the experimental dependences of ion currents. The rate constants were optimized parameters. In each procedure not more than two rate constants were determined. While fitting the dependences for the tertiary ions and the ions of the fourth generation the values of the rate constants determined in the previous fitting sessions for the primary and secondary ions were used. The results are shown in Table 1.

Table 1.

Effective binary rate coefficients at 1.1 Torr pressure of He for some processes

	reaction		**rate constant, 10^9 cm3 s^{-1}**
1	**Xe^++Ac**	**→ products**	**1.88±0.06**
1 a)		**→ $C_3H_6O^+$ + Xe**	**0.045±0.002**
1 b)		**→CH_3CO^++Xe**	**1.81±0.07**
2	**CH_3CO^++Ac (+He)**	**products**	**0.84 ±0.05**
2 a)		**AcH^+ + CH_2CO**	**0.29±0.03**
2 b)		**CH_3CO^+Ac**	**0.45 ±0.05**
3	**CH_3CO^+Ac + Ac (+He)**	**products**	**0.49±0.04**
3 a)		**$H^+(Ac)_2$ + products**	**0.22±0.08**
3 b)		**$CH_3CO^+(Ac)_2$**	**0.26±0.4**
4	**$CH_3CO^+(Ac)_2$+Ac**	**products**	**0.25±0.8**
5	**$C_3H_6O^+$+Ac**	**products**	**0.54±0.03**
6	**AcH^+ + Ac + (He)**	**$(Ac)_2H^+$ + (He)**	**0.88±0.1**

Discussion

The main channel of Xe^+ + $(CH_3)_2CO$ reaction is the production of CH_3CO^+ ions. Only 2.5% of $C_3H_6O^+$ ions are formed in a parallel channel. The secondary $C_3H_6O^+$ ions cannot be unambiguously attributed to the ***A*** state of the acetone cation. The determined rate constant of the reaction of the charge transfer product ion with acetone does not differ much from measurements of other authors. In some of those measurements $C_3H_6O^+$ ion was formed by electrons and photons whose energy was lower than the threshold of the production of the cation in the ***A*** state.

For the other secondary ion (CH_3CO^+) a competition of slightly endoergic proton transfer (38±4%) with the association (62±4% at 1.1 Torr of He) takes place.

A reaction of the ternary $CH_3CO^+(CH_3)_2CO$ ion also has the association channel. Another channel is a production of the protonated dimer of acetone $((CH_3)_2CO)_2H^+$. The channel is exoergic about 15 kcal/mole (the estimation is based on the difference in the binding energies of the clusters (31 kcal/mole for $((CH_3)_2CO)_2H^+$ and 12.5 kcal/mole for $CH_3CO^+(CH_3)_2CO$) and a difference in the proton affinities of ketene and acetone taken equal to 3.2 kcal/mole). A competition of an exoergic particle transfer process with an association channel is not typical for ion/molecule reactions.

There is another thermochemically allowed channel of the reaction of $CH_3CO^+(CH_3)_2CO$ ion in which protonated acetone and a stable molecule $C_5H_8O_2$ are produced. E.g. for the CH_3-CO-CH_2-CO-CH_3 product molecule (which requires minimal rearrangement of particles) the reaction is exoergic about 12-13 kcal/mole. A detailed analysis of the kinetic dependence of the ion current of protonated acetone shows that the contribution of the channel is not significant (otherwise the kinetics of the ion of the fourth generation should be imposed on the kinetics of the tertiary ion).[*]

The cluster $CH_3CO^+((CH_3)_2CO)_2$ may be considered as a "metastable" ionic particle i.e. its spontaneous reactive decay (whose ionic product is protonated acetone) is exoergic by several kcal/mole. (It follows from the assumption that the clusterization energy for CH_3CO^++$(CH_3)_2CO$ process more than for $CH_3CO^+(CH_3)_2CO$ + $(CH_3)_2CO$ one.) A careful analysis of the kinetic dependences shows that the time of the "reactive decay" is at least longer than 10 ms.

---

[*] The analysis also shows that the dependence is not affected by the decay of the $((CH_3)_2CO)_2H^+$ ions.

The rate constant of the reaction of the $CH_3CO^+((CH_3)_2CO)_2$ ion with acetone is about 0.25 10^{-9} cm^3 s^{-1}. The channels of the production of $CH_3CO^+((CH_3)_2CO)_3$ and $H^+((CH_3)_2CO)_3$ ions are not significant (the intensities of the corresponding ion currents are too low to explain the loss of the ion in the reaction). Thus the main ionic product of the reaction is the protonated dimer of acetone i.e. same ionic product of the rearrangement channel of the reaction of the precursor $CH_3CO^+(CH_3)_2CO$ ion cluster with acetone.

Why does a collision of the $CH_3CO^+((CH_3)_2CO)_2$ ion with acetone induce the production of the protonated dimer of acetone? As a possible explanation the production of $C_5H_8O_2$ neutral may be suggested. It is not clear why does this product is not produced efficiently in the reaction of a smaller ion cluster. The effect may be attributed to also to a higher exothermicity in the case of the larger cluster.

At [A]t > 3 10^{9} cm^{-3} s an additional source of a production of $C_3H_6O^+$ ions becomes efficient (see Fig.2). It is not possible to identify the process resulting in the production of these ions. The dependence does not show a decrease in the range. It may indicate that the ions practically have a low rate of the reaction with acetone.

Thermochemical calculations show that the production of protonated acetone from acetone cation is exoergic by 4.5 kcal/mole while the formation of the product from its isomer (enolic acetone cation whose energy level is by 14 kcal/mole lower) is endoergic. The only pathway for the loss of the isomeric ion in reaction with acetone is the association reaction producing nonprotonated dimer. The ion with m/e=116 was observed in our experiment see (Figure 2). The loss of the dimer in the reaction with acetone takes place in an exoergic reaction in which the protonated dimer of acetone is produced.

References

[1] T. Baer*, Adv. Chem. Phys.* **64,** 111 (1985)

[2] R. Bombach, J.P. Stadelmann and J. Vogt, *Chem. Phys.* **72,** 259 (1982)

[3] D.M. Minz and T. Baer, *Int. J.Mass Spectrom. Ion Phys.*, 25 (1977)

[4] P.J. Derrick, and S. Hammerum, *Can. J. Chem.* **64**, 1957 (1986)

[5] K. Qian, A. Shukla, S. Howard, S. Anderson, J. Futrel, *J. Phys, Chem.* **93**, 3889 (1989)

[6] K. Qian, A. Shukla, J. Futrel, *J. Phys, Chem.* **92**, 5988 (1992)

[7] R. Zhao, R. Tosh, A. Shukla, J. Futrel, *Int. J. Mass. Spectrom. Ion Proc.***167/168**, 317 (1997)

[8] C. Lifshitz*, J.Phys.Chem.* **87,** 2304 (1983)

[9] P.S. Vinogradov, O.V. Dmitriev, *Khimiya Visokih Energiy* 24, 483, (1990) (*Russian*)

[10] P.S. Vinogradov, D.M. Borisenko, In Proceedings of the 46th ASMS Conference on Mass Spectrometry and Allied Topics. Orlando, Florida, 1998, ThPA 009

Modelfree Determination of Dissociation Energies

M. Vogel[1], K. Hansen[2], A. Herlert[1] and L. Schweikhard[3]

1 *Institut für Physik, Johannes Gutenberg-Universität, D-55099 Mainz, Germany*
2 *Insitute for Physics, University of Jyväskylä, Finland*
3 *Institut für Physik, Ernst-Moritz-Arndt-Universität, D-17487 Greifswald, Germany*

1. Introduction

The most fundamental parameter in the characterization of any free stable polyatomic particle (molecule, fullerene, polymer or cluster) is its dissociation energy. It is of great importance since it reflects structural and dynamical properties of the system under investigation and is of major relevance in any activated process the particle can undergo.

Therefore, numerous methods have been developed to extract the dissociation energies from various properties of the systems. These activities have been a major part of research in physical chemistry during most of the 20^{th} century. Many models exist that equate the rate of disintegration at a known excitation to the dissociation energy [1-8]. However, such a determination of dissociation energies is rather indirect and depends on the characteristics of the respective model as well as on a number of often implicit assumptions about the systems' properties. It is thus vulnerable to systematic uncertainties of all kind.

A new procedure [9] allows a direct measurement of dissociation energies without any assumptions on how the disintegration process proceeds. It does not rely on any model of the system, of its disintegration behavior or of other properties.

As an example, we have determined the dissociation energies of a series of gold clusters Au_n^+ [9, 10]. The resulting dissociation energies show no energy dependence and are typically about one order of magnitude more accurate than values from traditional analyses. Thus, the new method allows to experimentally set benchmarks for any theory which attempts to describe activated processes of polyatomic systems.

2. Method

The basic idea of the new method [9] is to compare the excitation energy E_A of a sequential decay

$$A \to B \to C \tag{1}$$

with the corresponding energy E_B of the single decay

$$B \to C \tag{2}$$

that leads to the same final product. When the single decay process (2) depends in a measurable way on the amount of excitation energy present, it can be used as an uncalibrated thermometer for the last step of the sequential reaction (1). Adjusting either of the two excitation energies E_A and E_B to produce the same reading of the thermometer, the difference in excitation energies, $E_A - E_B$, is a direct measure of the energy consumed in the first step of the sequential decay, which is essentially the dissociation energy of A.

2.1 Decay Rate as a Thermometer

The rate k of unimolecular decay upon photoexcitation may serve as a thermometer to measure the energy content of the intermediate reaction product. In the case of free gold cluster ions, process (1) reads

$$Au_n^+ \rightarrow Au_{n-1}^+ \rightarrow Au_{n-2}^+ \tag{3}$$

and is compared to the corresponding single-step process

$$Au_{n-1}^+ \rightarrow Au_{n-2}^+ \tag{4}$$

at the same rate k for the build-up of the product Au_{n-2}^+. The dissociation energy D_n of the cluster Au_n^+ is then given by

$$D_n = E_{ph,n} - E_{ph,n-1} + (E_{th,n} - E_{th,n-1}) - E_{KER} \tag{5}$$

where $E_{ph,n}$ and $E_{ph,n-1}$ are the photoexcitation energies of the respective cluster sizes, $E_{th,n}$ and $E_{th,n-1}$ are their initial thermal energies and E_{KER} is the kinetic energy of the evaporated atom in the first step of the sequence. The contributions of both the thermal energy and the KER lead to only small corrections. The thermal energy is given by approximately 0.021 eV per vibrational degree of freedom, as calculated from the bulk heat capacities. A Debye approach results in the very similar value of 0.020 eV. The kinetic energy release is a measurable quantity [16-18], but in view of the small magnitude of the correction, a calculated estimate suffices here. Figure 1 illustrates the determination of the dissociation energy of Au_{17}^+ where the decay rates serve as a thermometer. The decay rates have been measured by pulsed laser excitation of size-selected cluster ions stored in a Penning trap [9]. As the measurements show, the decay rates of the last step of the sequential reaction $Au_{17}^+ \rightarrow Au_{16}^+ \rightarrow Au_{15}^+$ and the single-step reaction $Au_{16}^+ \rightarrow Au_{15}^+$ as a function of photoexcitation energy show the same dependence on the excitation energy with the only difference of an energetic shift of 3.47(6) eV. By use of eq. (5) this translates into a dissociation energy of the Au_{17}^+ cluster of 3.37(9) eV.

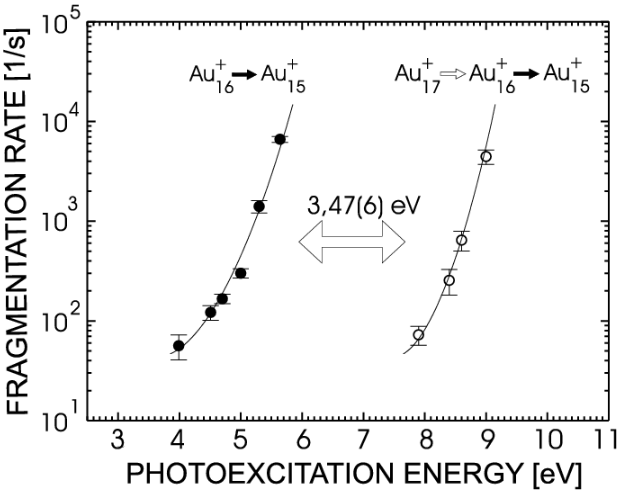

Figure 1: Rates of fragmentation as a function of photoexcitation energy for the decays $Au_{17}^+ \rightarrow Au_{16}^+ \rightarrow Au_{15}^+$ and $Au_{16}^+ \rightarrow Au_{15}^+$ (from ref. [9]).

2.2 Branching Ratio as a Thermometer

Alternatively, in the case of small, even-size group-11-element clusters (Cu_n^+, Ag_n^+, Au_n^+) the energy-dependent decay pathway branching ratio [11, 12] can be used as a thermometer [10]. In this case the sequential reaction

$$Au_n^+ \rightarrow Au_{n-1}^+ \begin{array}{l} \nearrow Au_{n-2}^+ + Au \quad (f_1) \\ \searrow Au_{n-3}^+ + Au_2 \quad (f_2) \end{array} \tag{6}$$

is compared to the single-step reaction

$$Au_{n-1}^+ \begin{array}{l} \nearrow Au_{n-2}^+ + Au \quad (f_1) \\ \searrow Au_{n-3}^+ + Au_2 \quad (f_2) \end{array} \tag{7}$$

at the same branching ratio f_2/f_1 of the products Au_{n-3}^+ (after neutral dimer evaporation) and Au_{n-2}^+ (after neutral monomer evaporation). Again, the dissociation energy is given by eq. (5) Figure 2 shows the branching ratios as a function of photoexcitation energy for the determination of the dissociation energies of Au_{14}^+ and Au_{16}^+. The energetic differences of 3.31(5) eV in the case of Au_{14}^+ (top picture) and 3.15(7) eV in the case of Au_{16}^+ (bottom picture) translate via eq. (5) into dissociation energies of D_{14}=3.24(7) eV and D_{16}=3.03(9) eV, respectively.

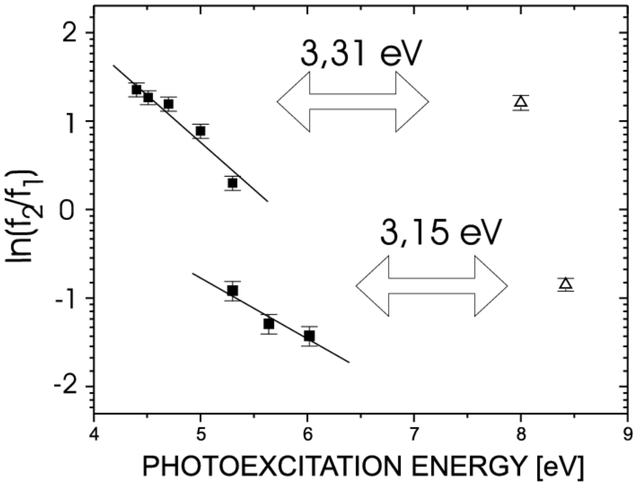

Figure 2: Branching ratios as a function of photoexcitation energy for the determination of the dissociation energies of Au_{14}^+ (top picture) and Au_{16}^+ (bottom picture). From ref. [10].

3. Results and Outlook

The new method has been applied to gold cluster ions Au_n^+ of sizes n=14-24. Figure 3 shows the resulting monomer dissociation energies. Open symbols give the values from the new method with the decay rate as thermometer. Full symbols represent values from the decay branching ratio as thermometer. As can be seen, the values from the independent methods agree within statistical uncertainties. The new method is currently applied to the vanadium cluster V_{13}^+, where a precise knowledge of the dissociation energy is required for a study of radiative cooling

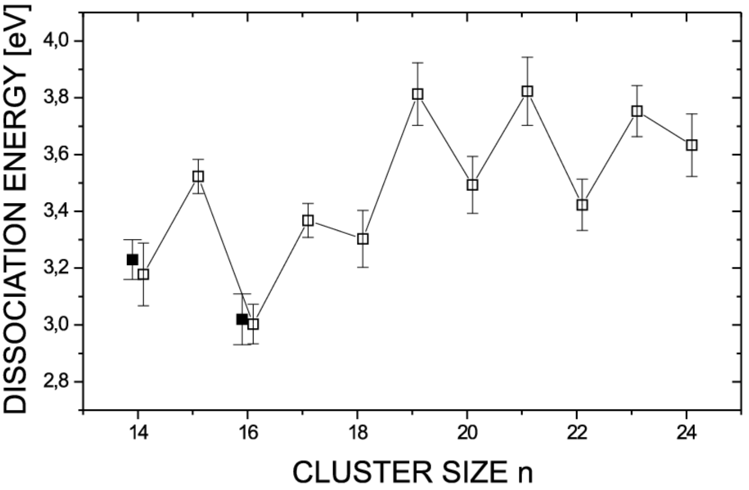

Figure 3: Dissociation energies of clusters Au_n^+ n=14-24 (from ref. [10]). Open symbols correspond to values from the decay rate as thermometer, whereas full symbols represent values from the branching ratios as thermometer.

from transition metal clusters [16]. Furthermore, the method is currently extended to the determination of dimer dissociation energies, and to the binding energy of a methanol molecule to a gold cluster.

References

[1] L.S. Kassel, *J. Phys. Chem.* **32** (1928) 225

[2] O.K. Rice and H.C. Ramsperger, *J. Am. Chem. Soc.* **50** (1928) 617

[3] V. Weisskopf, *Phys. Rev.* **52** (1937) 259

[4] R.A. Marcus, *J. Chem. Phys.* **20** (1952) 359

[5] C.E. Klots, *J. Phys. Chem.* **75** (1971) 1526

[6] W.J. Chesnavich and M.T. Bowers, *J. Chem. Phys.* **66** (1977) 2306

[7] P.C. Engelking, *J. Chem. Phys.* **87** (1987) 936

[8] K. Hansen, *Philos. Mag. B* **79** (1999) 1413

[9] M. Vogel, K. Hansen, A. Herlert and L. Schweikhard, *Phys. Rev. Lett.* **87** (2001) 013401

[10] M. Vogel, K. Hansen, A. Herlert and L. Schweikhard, *Chem. Phys. Lett.* **346** (2001) 117

[11] M. Vogel, K. Hansen, A. Herlert and L. Schweikhard, *Appl. Phys. B* **73** (2001) 411

[12] M. Vogel, K. Hansen, A. Herlert and L. Schweikhard, *Eur. Phys. J. D* **16** (2001) 73

[13] M. Lundquist et al., *Phys. Rev. Lett.* **75** (1995) 1058, and references therein

[14] A.J. Stace, *J. Chem. Phys.* **85** (1996) 5774

[15] A.J. Stace, A.K. Shukla, *Chem. Phys. Lett.* **85** (1982) 157

[16] C. Walther et al., *Phys. Rev. Lett.* **83** (1999) 3816

On the efficiency of projectile energy deposition for potential and kinetic electron emission from clean metal surfaces

HP. Winter, S. Cernusca, H. Stöckl and F. Aumayr

Institut für Allgemeine Physik, TU Wien, Austria

Recent years have seen important improvements for experimental studies of slow-ion induced electron emission from atomically clean solid surfaces. These developments are of great interest for a better understanding of the relative importance of the kinetic and potential energy of slow projectile ions. Both energy contents can give rise to slow electron emission, hence we speak of kinetic emission (KE) and potential emission (PE). Furthermore, the target surface material and -topography are highly relevant for these emission processes, and in this respect systematic investigations are still lacking. In general, our understanding of the inelastic interaction of slow neutral, singly- and multiply charged projectiles with solid surfaces is still far from satisfactory, since most of the published data in this field involves target surfaces with not sufficiently well defined conditions (for a recent review, cf. /1/).

In our own recent studies we have concentrated on atomically clean target surfaces of both metals and insulators. If such targets have a polycrystalline structure, they may contain defects and their surface is usually rough, in which case the ion impact geometry is rather poorly defined. This is not of much concern for PE which occurs dominantly above the surface /1/, but is rather critical for KE which is initiated only after the ion has made close surface contact. Therefore, better prospects are offered by atomically flat monocrystalline target surfaces with grazing incidence of the projectile ions, which assures rather well defined projectile trajectories. In this case the resulting electron emission can be conveniently studied with the electron statistics technique which not only provides the absolute total electron yield but also the statistical distribution of the number of emitted electrons from which additional details of the mechanisms responsible for electron emission can be obtained /2/. Under such experimental conditions, different projectile trajectories can be identified from their two-dimensional imprint on a channelplate detector behind the impact region /3/. By using such arrangements for slow ion bombardment of Au(111) and LiF(001) we could separate contributions from PE and KE to the total electron emission. With such studies carried out with different projectile charge states and -kinetic energies, a more detailed understanding of the involved KE processes is obtained than just from the total yields, and even more can be learnt if, in addition, the resulting projectile energy loss is measured by means of a time-of-flight technique.

Especially interesting are studies where this projectile energy loss is measured in coincidence with the electron emission statistics, as has been demonstrated for impact of neutral hydrogen atoms on a LiF(001) surface /4/.

Whereas for low ion charge states the resulting total PE yield is proportional to the involved potential energy of the projectile, for higher charged ions an increasing fraction of the related potential energy will be spent for emission of fast Auger electrons and soft x-rays which result from the recombination of transient inner shell projectile vacancies /5/. Nevertheless it is remarkable that a rather large amount of potential energy (typically 100 eV) is needed per emission of one slow electron. To better understand this poor efficiency of PE, we need systematic measurements of the energy distribution of ejected electrons, preferably to be carried out under similar well-defined projectile scattering conditions as described above.

Precise knowledge of these electron energy distributions is even more important for a detailed understanding of the mechanisms responsible for KE from metal surfaces. So far, the common belief was that the KE yield is more or less proportional to the electronic stopping power for the projectile in the target material /6/. However, recent theoretical considerations in comparison with precise KE yield data have shown that at low projectile impact energy, i.e. near the KE threshold, stopping due to the metal electron gas does not provide the dominant KE contribution and thus other KE mechanisms had to be taken into account /7/. This is especially important for heavy projectile ions, whereas for light projectiles stopping in the target electron gas is most relevant for the total KE yield and only then a well-defined (socalled classical) KE threshold can be observed. A recent comparison of the dependences of total KE yields on the ion impact velocity for polycrystalline gold and graphite targets have also shown the important role of the Fermi electron energy for this KE threshold /8/.

Another remarkable feature with respect to ion-induced electron emission is the excitation of plasmons at the expense of the potential projectile energy, the signature of which can be seen in the respective electron energy distributions /9/. Also here more systematic studies are desirable in order to understand the reason for this "potential excitation of plasmons - PEP".

New ways to determine the amount of the projectile potential energy which is kept in a target surface have recently been opened by measurements of the number of electron-hole pairs created in a silicon detector /10/, and of the thermal energy deposited into a copper strip target connected to a lN_2 cooled microcalorimeter /11/. In both cases it was found that only about 30-40% of the total potential projectile energy remain in the surface. If these findings are compared with the relatively small amount of energy carried away by the PE electrons (see above), a significant fraction of the total available potential energy is still missing.

In summary, new experimental techniques are now available for studying in more systematic ways the deposition of potential and kinetic energy of slow ions impinging on well defined target surfaces. A satisfactory explanation of the thereby involved projectile energy balance can probably be obtained from the energy distributions of the ejected electrons which take over a substantial amount of the initial projectile energy.

Acknowledgments

This work was supported by FWF and carried out within Association EURATOM-ÖAW.

References

---

[1] HP. Winter and F. Aumayr, *Physica Scripta T* **92** 15 (2001).

[2] C. Lemell J. Stöckl, HP. Winter and F. Aumayr, *Rev. Sci. Instrum.* **70** 1653 (1999).

[3] C. Lemell J. Stöckl, J. Burgdörfer, G. Betz, HP. Winter and F. Aumayr, *Phys.Rev. A* **61** 012902-1 (1999); J. Stöckl, C. Lemell, HP. Winter and F. Aumayr, *Physica Scripta T* **92** 135 (2001).

[4] A. Mertens, K. Maass, S. Lederer, H. Winter, H. Eder, J. Stöckl, HP. Winter, F. Aumayr, J. Viefhaus and U. Becker, *NIM B* **182** 23 (2001).

[5] F. Aumayr and HP. Winter, *Comments At.Mol.Phys.* **29** 275 (1994).

[6] D. Hasselkamp, in Particle Induced Electron Emission II, Springer Tracts in Modern Physics vol. **123**, Springer Berlin (1992).

[7] J. Lörincik, Z. Sroubek, H. Eder, F. Aumayr and HP. Winter, Phys.Rev. B **62** 16116 (2000).

[8] S. Cernusca, A. Diem, HP. Winter, F. Aumayr, J. Lörincik and Z. Sroubek, *Nucl. Instrum. Meth. Phys. Res. B* (2002, in print).

[9] H. Eder, F. Aumayr, P. Berlinger, H. Störi and HP. Winter, *Surface Science* **472** 195 (2001); J. Lörincik, Z. Sroubek, F. Aumayr and HP. Winter, *Europhys. Letters* **54** 633 (2001).

[10] T. Schenkel et al., *Phys.Rev. Letters* **83** 4273 (1999).

[11] U. Kentsch, H. Tyrroff, G. Zschornack and W. Möller, *Phys.Rev. Letters* **87** 105504-1 (2001).

An Intercomparison of Airborne VOC Measurements

Armin Wisthaler, and Armin Hansel

Institut fürIonenphysik der Leopold-Franzens-Universität, Innsbruck, Austria

Ray Fall

Department of Biochemistry, University of Colorado, Boulder , USA

Paul D. Goldan, Gerd Hübler, and Fred C. Fehsenfeld

Aeronomy Laboratory, National Oceanic and Atmospheric Administration (NOAA), Boulder, USA

Abstract

During the Texas Air Quality Study (TexAQS) 2000 ambient air samples were analyzed on-board the NSF/NCAR ELECTRA research aircraft by two VOC measurement techniques: 1) an in-situ gas chromatograph named TACOH (Tropospheric Airborne Chromatograph for Oxy-hydrocarbons and Hydrocarbons), operated by NOAA's Aeronomy Laboratory, and 2) a chemical ionization mass spectrometer named PTR-MS (Proton-Transfer-Reaction Mass Spectrometer) and operated by the University of Innsbruck. The sample protocols were quite different for the two methods: the TACOH system collected air samples for 15-60 sec (depending upon altitude) every 15 min, the PTR-MS system monitored selected VOCs on a time-shared basis for 2 sec respectively, once every 4-20 sec, depending upon the number of monitored species. Simultaneous measurements of acetaldehyde, isoprene, the sum* of acetone and propanal, the sum* of methyl vinyl ketone and methacrolein (* PTR-MS does not distinguish between isobaric species) and toluene show good agreement despite being performed in the complex and highly polluted Houston air matrix.

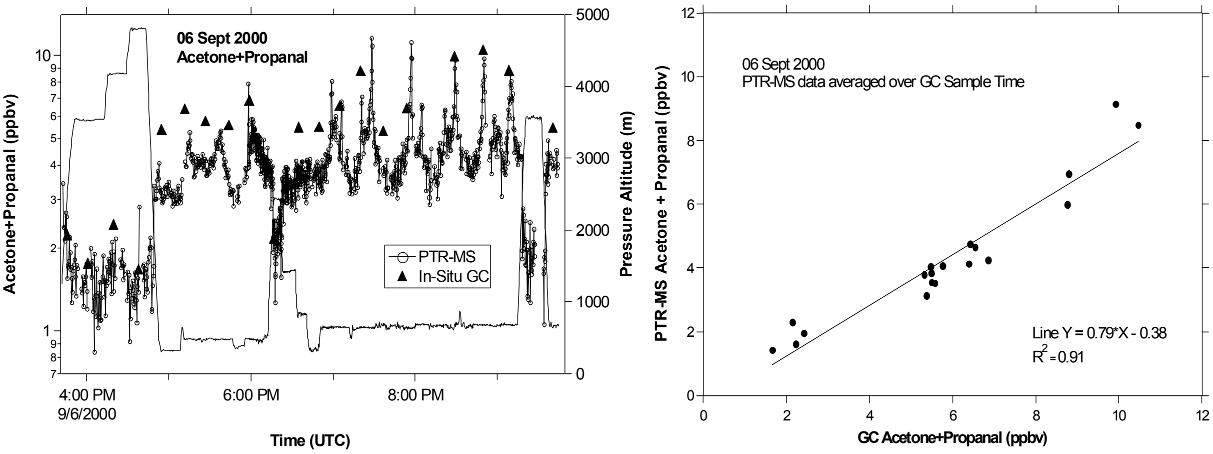

Fig. 1 Flight data of September 6, 2000. Temporal variation of acetone+propanal volume mixing ratios; scatter plot of overlapping PTR-MS and GC measurements

The infrared spectrum of the chiral molecule CDBrClF in the range 600-1150cm^{-1}: A rovibrational analysis of the ν_4 and ν_5 band

Sieghard Albert, Vincent Boudon[1] and Martin Quack

Laboratorium für Physikalische Chemie - ETH-Zürich (Hönggerberg)
CH 8093 Zürich - Switzerland

Abstract

The rovibrational spectrum of the chiral molecule CDBrClF has been analysed on the basis of an effective Hamiltonian [1]. The spectra have been recorded at room temperature with a Fourier transform infrared (FTIR) spectrometer (resolution 0.0024 cm^{-1}) and a supersonic jet diode laser spectrometer (resolution 0.001 cm^{-1}). The assignment of the ν_4 and ν_5 rovibrational lines of the FTIR spectrum for the two major isotopomers CD^{79}Br^{35}ClF and CD^{81}Br^{35}ClF has been carried out with an interactive Loomis-Wood program. Accurate rotational and quartic centrifugal distortion constants for the ν_4 and ν_5 vibrational state of CD^{79}Br^{35}ClF and CD^{81}Br^{35}ClF have been determined. A new experimental technique based on backward wave oscillators is proposed in order to measure the parity violation.

Introduction

CDBrClF, the deutero isotopomer of CHBrClF, is an example of one of the simplest chiral molecules. It has an asymmetric carbon with C_1 point group symmetry. CHBrClF has been analysed recently in detail with respect to its spectra and its intramolecular vibrational redistribution (IVR) dynamics [2–5]. CDBrClF offers the opportunity to investigate the effect of deutero isotopic substitution in the spectra. The vibrational spectrum of CDBrClF has been analysed from the far infrared (FIR) to the near infrared (NIR) region [6]. A rovibrational analysis of the spectrum is challenging due to the congestion of lines which results from the low symmetry of the molecule and the presence of four different isotopomers (CD^{79}Br^{35}ClF : CD^{81}Br^{35}ClF : CD^{79}Br^{37}ClF : CD^{81}Br^{37}ClF = 0.380 : 0.369 : 0.122 : 0.118) .

Another motivation to investigate the rotationally resolved spectra of this molecule arises from effects generated by parity violation [3–5, 7–11]. While an unsuccessful attempt to see these effects in CHBrClF has been made already a quarter century ago [7, 11], our studies seem to be the first on the D-isotopomer in this respect. Both molecules have been studied extensively in theoretical work on parity violation in our group [8–10]. New calculations including CDBrClF [9, 10] show a very small impact on relative vibrational and rotational frequency shifts due to the parity violation on the order of $\Delta\nu/\nu = 10^{-17}$ to 10^{-16} [8–10]. Recent, still unsuccessful experiments giving a limit on the order of $\Delta\nu/\nu = 10^{-13}$ are in agreement with these calculations [12].

Experimental details

The spectrum of CDBrClF has been recorded in two different ways. A Fourier transform infrared (FTIR) spectrum in the spectral region between 600–1140 cm^{-1} was measured with the Zuerich BOMEM DA 002 interferometric Fourier transform infrared (FTIR) spectrometer [13] with a resolution up to 0.004 cm^{-1}. Diode laser spectra using the Zuerich supersonic slit jet system [14] were obtained in the region 745–752 cm^{-1}. The diode laser spectra were recorded with a resolution of 0.001 cm^{-1}. In order to improve the vibrational cooling CDBrClF has been mixed with helium with a CDBrClF:He seeding ratio of 1:4, resulting in rotational temperatures in the range T_{rot}=15–40 K.

---

[1] present address: Laboratoire de Physique de l'Université de Bourgogne 9 av. A. Savary, B.P. 47870-21078 Dijon Cedex, France

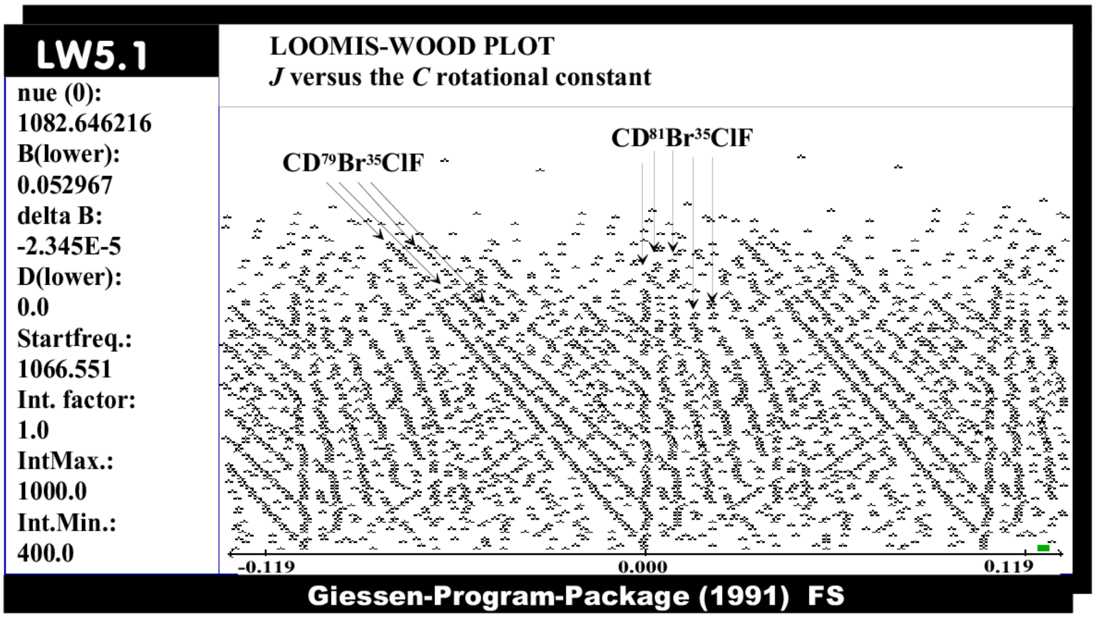

nue (0):
1082.646216
B(lower):
0.052967
delta B:
-2.345E-5
D(lower):
0.0
Startfreq.:
1066.551
Int. factor:
1.0
IntMax.:
1000.0
Int.Min.:
400.0

Figure 1: Loomis-Wood plot of the ν_4 band. The P-branches of the c-type series are shown. The rotational quantum number J is plotted versus the rotational constant C. The vertical series belong to the isotopomer $CD^{81}Br^{35}ClF$ and the slanted series belong to the isotopomer $CD^{79}Br^{35}ClF$.

Assignment and analysis

The assignment of the observed rovibrational transitions in the FTIR spectra belonging to a particular subband consisting of P- and R-branches has been carried out efficiently with an interactive Loomis-Wood assignment program [15]. Two types of subbands have been assigned in the spectrum of the ν_4 region. One type consists of transitions with $(J \pm 1, K_a, K_c = J \pm 1 - K_a) \leftarrow (J, K_a, K_c = J - K_a)$ (P- and R- branches) which correspond to c-type transitions. The different series can be clearly seen in the Loomis-Wood plot in Fig. 1. The spacing between two transitions of a series is approximately $2C$. The Loomis-Wood plot in the c-type region of the ν_4 band provides an easy separation of transition lines in transitions belonging to the $CD^{79}Br^{35}ClF$ or $CD^{81}Br^{35}ClF$ isotopomer. The other type of subbands consists of $(J \pm 1, K_a = J \pm 1 - K_c, K_c) \leftarrow (J, K_a = J - K_c, K_c)$ transitions (P- and R-branches) which correspond to a-type transitions.

In the ν_5 region of the spectrum, only c-type transitions have been assigned in the FTIR spectrum. The jet-cooled diode laser spectra have been used to assign the a-type transitions. The a-type Q-branches around 748 cm^{-1} in the jet-cooled diode laser spectrum have been assigned from $J = 2$ up to $J = 12$ with K_c up to 2 for $CD^{79}Br^{35}ClF$ and $CD^{81}Br^{35}ClF$. Fig. 2 shows the Q-branches for the two isotopomers.

The rovibrational analysis has been carried out with Watson's A reduced effective Hamiltonian in the I^r representation up to quartic centrifugal distortion constants

$$\tilde{H}^{vv} = A\tilde{J}_a^2 + B\tilde{J}_b^2 + C\tilde{J}_c^2 + \Delta_J\tilde{J}^4 + \Delta_{JK}\tilde{J}^2\tilde{J}_a^2 - \Delta_K\tilde{J}_a^4 - \frac{1}{2}[\delta_J\tilde{J}^2 + \delta_K\tilde{J}_a^2, \tilde{J}_+^2 + \tilde{J}_-^2] \tag{1}$$

with $\tilde{J}_\pm = \tilde{J}_b \pm i\tilde{J}_c$. The rotational constants A, B, C and the centrifugal distortion constants Δ_J, Δ_{JK}, Δ_K, δ_J and δ_K depend upon the vibrational level v. The spectroscopic data have been analyzed by our Wang program [16].

FTIR and jet-cooled diode laser spectra were fitted together with a standard deviation of $d_{rms} = 0.0006$ cm^{-1}. In Table 1 the spectroscopic constants of the ν_4 and ν_5 states are presented. The A rotational constants of $CD^{79}Br^{35}ClF$ and $CD^{81}Br^{35}ClF$ are similar for the ν_4 and ν_5 states in each isotopomer; but significantly smaller than in the ground state. By contrast, the B constants

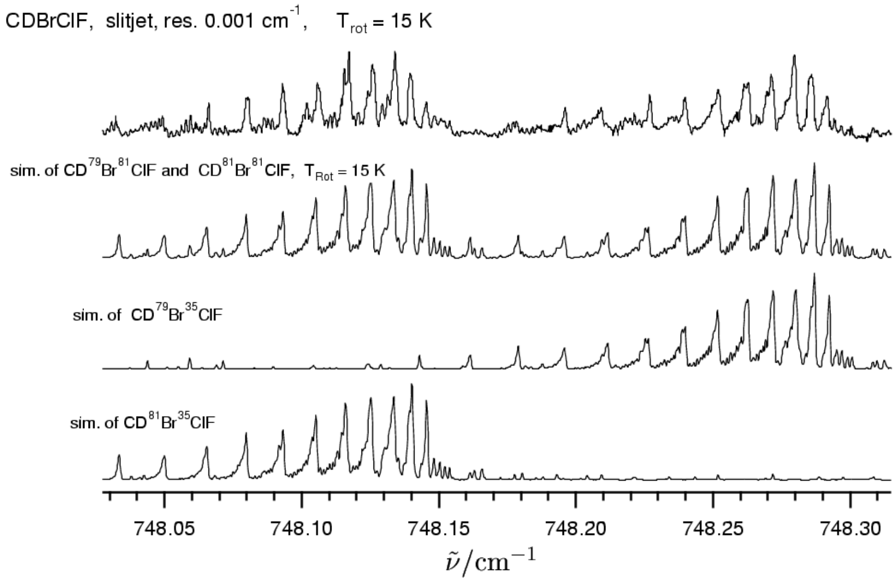

Figure 2: Part of the a-type Q-branches between $J = 2 - 12$. The upper trace shows the jet-cooled spectrum measured in absorbance. The rotational temperature $T_{rot} = 15$ K has been determined by comparison with the simulated spectrum. The lower trace illustrates the simulated spectrum for the two major isotopomers $CD^{79}Br^{35}ClF$ and $CD^{81}Br^{35}ClF$.

are quite similar in the ground and the excited states ν_4 and ν_5 for both isotopomers. The C constants are slightly smaller in the ν_5 state than those in the ν_4 state. The shift of the ν_5 band center for $CD^{79}Br^{35}ClF/CD^{81}Br^{35}ClF$ (0.157 cm^{-1}) is larger than that of the ν_4 band center for the $CD^{79}Br^{35}ClF/CD^{81}Br^{35}ClF$ (0.015 cm^{-1}) pair.

	ν_5		ν_4	
	$CD^{79}Br^{35}ClF$	$CD^{81}Br^{35}ClF$	$CD^{79}Br^{35}ClF$	$CD^{81}Br^{35}ClF$
A	0.207 965 6 (34)	0.207 787 6 (32)	0.207 983 6 (18)	0.207 818 1 (19)
B	0.067 094 9 (70)	0.066 598 2 (57)	0.067 117 9 (68)	0.066 612 7 (55)
C	0.053 193 72 (83)	0.052 749 59 (84)	0.053 237 41 (82)	0.052 793 63 (82)
$\Delta_J \times 10^{-6}$	–0.035 1 (21)	–0.039 4 (23)	0.073 2 (27)	0.138 0 (16)
$\Delta_{JK} \times 10^{-6}$	–0.084 5^2	–0.092 4^3	–0.166 9 (96)	–0.395 6 (61)
$\Delta_K \times 10^{-6}$	0.125 9 (22)	0.138 4 (22)	0.099 5 (70)	0.264 1 (46)
$\delta_J \times 10^{-6}$	0.015 1 (30)	0.056 3 (21)	0.074 9 (13)	0.041 09 (77)
$\delta_K \times 10^{-6}$	–0.128 7 (35)	–0.051 9 (24)	–0.107 59 (81)	–0.117 96 (67)
ν_0	748.299 262 (80)	748.152 728 (80)	1082.811 77 (11)	1082.79656 (10)
n	345	352	834	828
d_{rms}	0.0006	0.0006	0.0006	0.0006

Table 1: Rotational constants and centrifugal distortion constants of the ν_5 and ν_4 states of $CD^{79}Br^{35}ClF$ and $CD^{81}Br^{35}ClF$ from the ν_4 and ν_5 fundamental band transitions. The standard deviations of the parameter values are given in parentheses. d_{rms} is the root-mean-square deviation of the fit. All constants are given in cm^{-1}.

For the simulation of the ν_5 band of $CD^{79}Br^{35}ClF$ and $CD^{81}Br^{35}ClF$ the following transition moment components obtained with *ab initio* calculations [6] were used: $\mu_a = 0.191$ D, $\mu_b = -0.0774$ D, $\mu_c = -0.0348$ D for ν_5. Fig. 2 illustrates the a-type Q-branches of the ν_5 band of $CD^{79}Br^{35}ClF$ and $CD^{81}Br^{35}ClF$ recorded with a diode laser in a seeded supersonic slit expansion with an effective rotational temperature $T_{rot} = 15$ K. The Q-branches have been assigned from $J = 2$ up to $J = 12$. There is a good agreement between the experimental and calculated spectra.

Conclusion

A rovibrational analysis of the ν_4 and ν_5 bands has determined the spectroscopic constants of the ν_4, ν_5 and the ground state of $CD^{79}Br^{35}ClF$ and $CD^{81}Br^{35}ClF$ for the first time. The patterns of the ν_4 and ν_5 bands have also been found in the ν_6 and ν_3 spectral regions of CDBrClF.
The assignment of the highly resolved infrared spectrum of CDBrClF is expected to increase the possibility of finding spectral regions in order to carry out double resonance experiments as described in [7] to measure the energy difference between the two enantiomers caused by the parity violation potential or to measure infrared frequency shifts [12], as recent calculations [8–10] predict. With the ground work presented in [10] and here, it might be possible to detect rotational absorption line shifts caused by the parity violation potential with a phase locked submillimeter spectrometer in the terahertz region [17, 18]. Backward wave oscillators have frequency purity better than 1 Hz. If they are phase locked the ratio is in the range of $\Delta\nu/\nu = 10^{-10} - 10^{-11}$ in the THz region. This ratio is not sufficient to observe the effect in the CDBrClF spectra, but perhaps in heavier molecules. In the spectra presented here no splitting due to parity violation potential has been observed. This is in agreement with recent calculations [8–10].

References

[1] S. Albert, V. Boudon, and M. Quack. In L. Meerts, editor, *Seventeenth Colloquium on High Resolution Spectroscopy*, page 294. Universiteit Nijmegen, (2001); S. Albert and M. Quack, ibid., page 217, and to be published.

[2] A. Beil, D. Luckhaus, R. Marquardt, and M. Quack, J. Chem. Soc. Faraday Discuss., **99**, 49 (1994).

[3] A. Beil, D. Luckhaus, and M. Quack, Ber. Bunsenges. Phys. Chem., **100**, 1853 (1996).

[4] A. Beil, D. Luckhaus, M. Quack, and J. Stohner, Ber. Bunsenges. Phys. Chem., **101**, 311 (1997).

[5] A. Bauder, A. Beil, D. Luckhaus, F. Müller, and M. Quack, J. Chem. Phys., **106**, 7558 (1997).

[6] A. Beil, H. Hollenstein, O. Monti, M. Quack, and J. Stohner, J. Chem. Phys., **113**, 2701 (2000).

[7] M. Quack, Angew. Chem. Int. Ed. Engl., **28**, 571 (1989).

[8] M. Quack and J. Stohner, Phys. Rev. Lett., **84**, 3807 (2000).

[9] M. Quack and J. Stohner, Z. Physik. Chemie, **214**, 675 (2000).

[10] M. Quack and J. Stohner, Chirality, **13**, 745 (2001).

[11] V. Letokhov, Phys. Lett. A., **53**, 275 (1975).

[12] C. Daussy, T. Marrel, A. Amy-Klein, C. Ngyen, C. Borde, and C. Chardonnet, Phys. Rev. Lett., **83**, 1554 (1999).

[13] H.-R. Dübal and M. Quack, J. Chem. Phys., **81**, 3779 (1984).

[14] H. Hollenstein, M. Quack, and E. Richard, Chem. Phys. Lett., **222**, 176 (1994).

[15] B. Winnewisser, J. Reinstädtler, K. Yamada, and J. Behrend, J. Mol. Spectrosc., **136**, 500 (1989).

[16] D. Luckhaus and M. Quack, Mol. Phys., **68**, 745 (1989).

[17] D. Petkie, T. Goyette, R. Bettens, S. Belov, S. Albert, P. Helminger, and F. DeLucia, Rev. Sci. Instrum., **68**, 1675 (1996).

[18] F. Lewen, R. Gendriesch, I. Pak, D. Paveliev, M. Hepp, R. Schieder, and G. Winnewisser, Rev. Sci. Instrum., **69**, 32 (1998).

Direct and dissociative single electron capture in slow collisions of He^{2+} with O_2 and CO

M. Albu[1], L. Mrazek[2], F. Aumayr and HP. Winter

Institut für Allgemeine Physik, TU Wien, Austria

For the next generation of magnetically confined fusion plasma experiments, an important part of the plasma heating will have to be provided by fast alpha particles resulting from D-T fusion reactions. In a so-called burning fusion plasma these He^{2+} ions transfer their initial 3.5 MeV kinetic energy in series of elastic collisions to the deuterium and tritium fuel ions. After having slowed down, they end up as "He ash" which needs to be removed from the plasma to avoid inacceptable bremsstrahlung losses and dilution of the D-T fusion fuel. Removal of the He ash occurs in so far not yet well understood collective plasma processes for which in the outermost plasma region also atomic collisions between He^{2+} and neutral plasma constituents might be of some relevance. In the plasma scrape-off layer (SOL) there are non-negligible concentrations of hydrogen and oxygen molecules which result from particle- and radiation-stimulated desorption from the first wall components.

In collisions of He^{2+} with molecular species, single elctron transfer (SEC) is a highly probable process which may leave the product molecular ions in either bound or unbound (dissociated) states. For a satisfactory understanding of the reaction kinetics and energy balance in the edge plasma it is of interest to determine the absolute and relative importance of these non-dissociative and dissociative SEC processes. For this purpose we can apply as experimental method translational energy spectroscopy which determines the kinetic energy change of the (nearly) forward-scattered charge-exchanged projectile ions. Since these ions assume most of the inelastic energy loss or -gain from the relevant SEC reaction channels, the latter can be identified in the respective translational energy spectrum (TES). By varying the projectile ion scattering angle one may also select the related impact parameter range and thereby enhance or suppress different SEC channels in relation to each other. Such measurements have already been made for He^{2+} impact energies above 2 keV with molecular targets D_2, N_2, O_2 [1] and H_2 [2], and recently also at lower impact energies with H_2 [3], N_2 and CO [4], respectively.

Our translational energy spectrometer provides an ion kinetic energy resolution of ≤ 200 meV and therefore permits, at least in principle, discrimination between different final vibrational states for the SEC reactions of interest [5]. For SEC in collisions with relatively slow doubly charged ions, the socalled "reaction window" [6] offers reliable guidance for predicting the relatively most probable reaction channels, as demonstrated with both atomic [7] and molecular target species [5]. The reaction window favours slightly exothermic SEC reactions which are therefore most probably populated, whereas endothermic as well as stronger exothermic SEC reactions are efficiently suppressed. This clear selectivity for the SEC energy defect becomes less pronounced toward higher impact energy [4], however.

For the present measurements, the He^{2+} projectile ions have been produced from ^{4}He gas in a 5 GHz ECR multicharged ion source. We utilized the SEC reaction

$$He^{2+} + Ne \rightarrow He^{+}(n=1) + Ne^{+}(2s2p^{6}\,{}^{2}S) \qquad (\Delta E = +5.9\ \text{eV})$$

---

[1] Permanent address: National Institute for Physics and Nuclear Engineering "Horia Holubei", RO-76900 Bucharest-Magurele, Romania;

[2] Postdoctoral visiting scientist from J. Heyrovsky Institute of Physical Chemistry, Academy of Sciences of the Czech Republic, CZ-18223 Praha, Czech Republic.

for calibration of the TES kinetic energy gain-/loss scale, by adding Ne gas to the molecular target gas of interest into the collision cell of our translational energy spectrometer. If the fraction of Ne in the target gas mixture is well known, this method also provides a rather convenient way for determination of the absolute state-selective SEC cross sections for the molecular target of interest, by way of comparison with the cross section for the above SEC from Ne. The latter cross section can be very conveniently measured, because at low impact energy the related SEC channel is the only one favoured by the reaction window and therefore corresponds with good accuracy to the respective total SEC cross section. The latter on will be measured in the further course of this work over the impact energy range of interest.
First results of our present study can be summarized as follows.

He^{2+} + O_2 / Ne

TES have been measured at collision energies of 600, 800 and 1000 eV at 0° scattering angle. The dominant SEC channel corresponds to an energy gain of 1.3 eV and is thus identified as the non-dissociative SEC

$$He^{2+} + O_2\,(X^3\Sigma_g^-) \rightarrow He^{+*}\,(n=2) + O_2^+\,(X^2\Pi_g) \quad (\Delta E = 1.3\text{ eV}).$$

A rather broad feature observed for energy gains ΔE between 6 and 10 eV corresponds to reaction channels for dissociative SEC into He^+(n=1) via

$$He^{2+} + O_2\,(X^3\Sigma_g^-) \rightarrow He^+\,(n=1) + O_2^{+*}\text{ (various dissociative states).}$$

We have also measured TES for collision energies of 600 to 1000 eV at a scattering angle of 0.2°. The same reaction channels as mentioned above were observed, but for the finite scattering angle the non-dissociative SEC became slightly less important.

He^{2+} + CO / Ne

For this collision system TES were measured at impact energies between 600 and 1000 eV at 0° scattering angle. Here the non-dissociative SEC channel

$$He^{2+} + CO\,(X^1\Sigma_g^+) \rightarrow He^{+*}\,(n=2) + CO^+\,(X^2\Sigma^+) \quad \Delta E = -\,0.4\text{ eV}$$

was already not observable despite its small endothermicity, which is in clear contrast to similar measurements performed at only slightly higher impact energies [4].
Exothermic dissociative SEC

$$He^{2+} + CO\,(X^1\Sigma_g^+) \rightarrow He^+\,(n=1) + CO^+\text{ (various dissociative states)}$$

was only observable for energy gains ΔE between 6 and 15 eV. TES measured at scattering angles of 0.2° and 1° showed a similar relative importance of the dissociative SEC from CO with respect to the SEC from Ne as under exact forward-scattering conditions.

Acknowledgments

This work has been carried out within EU network project HPRN-CT-2000-00027 (MCInet).

References

[1] S.J. Martin, J. Stevens and E. Pollack, *Phys.Rev. A* **43** 3503 (1991)

[2] J.M. Hodgkinson, T.K. McLaughlin, R.W. McCullough, J.Geddes and H.B. Gilbody, *J.Phys. B: At.Mol.Opt.Phys.* **28** L393 (1995)

[3] D.M. Kearns, D.R. Gillen, D. Voulot, J.B. Greenwood, R.W. McCullough and H.B. Gilbody, Proc. XXII. ICPEAC Santa Fe/USA (July 18-24, 2001), Book of Abstracts of Contributed Papers p. 585

[4] E.Y. Kamber and S.M. Ferguson, loc.cit. [3], p. 586

[5] P. Leputsch, D. Dumitriou, F. Aumayr and HP. Winter, *J.Phys. B: At.Mol.Opt.Phys.* **30** 5009 (1997)

[6] K. Taulbjerg, *J.Phys. B: At.Mol.Opt.Phys.* **19** L367 (1986)

[7] HP. Winter, *Comments At.Mol.Phys.* **27** 91 (1991)

Plasma diagnostics with electrostatic probes in the Reactive Low Voltage Ion Plating process

T. Lechleitner, D. Huber, H.K. Pulker

Univ Innsbruck (A)

Summary:

The analysis of cold plasmas, which are used in thin film coating techniques, is mainly important for the understanding of the correlation between the film properties and the plasma (or the process) parameters. With the knowledge of these correlations, one is able to optimise and eventually improve the coating processes for the production of films with certain desirable properties. The plasma for the Reactive-Low-Voltage-Ion-Plating process is a cold non-isothermal plasma produced by a low-pressure dc non-self sustained arc discharge, controlled by two main parameters, the arc current and the total gas pressure in the chamber.

It shows, that the arc current is in a direct linear relation to the degree of ionisation and the increase of the total gas pressure has a contrary effect.

The additional aim of this work is to show, that the usage of electrostatic probes for the plasma analysis of deposition processes is a powerful tool to complete the common plasma monitor measurements (energy analysing quadrupol mass spectrometer) and to improve the understanding of industrially used plasmas.

Keywords:

Tribological coatings, TiN, Langmuir probe, Faraday Cup, Ion plating, RLVIP

1. Introduction:

The outstanding feature of the RLVIP-Process is a dense beam of ions from the evaporation source and the gas inlet system to the substrate plane, which is responsible for the growth of the film. These ions are mainly produced by electron impact interaction of the arc discharge electrons with the evaporated film material. [1]

The RLVIP process is mainly controlled by two parameters:

1) The arc current between the hot filament of the plasma source as the cathode and the evaporation source as the anode of the arc discharge.

2) The total gas pressure in the recipient, consisting of Argon and a reactive gas component, in this case Nitrogen.

Variations of these parameters show the relation between arc current and total gas pressure respectively with the density and the energy distribution of the ions and electrons in the plasma. Plasma density and energy distribution of the ions are responsible for the properties of the obtained films, such as their density and their mechanical stress.

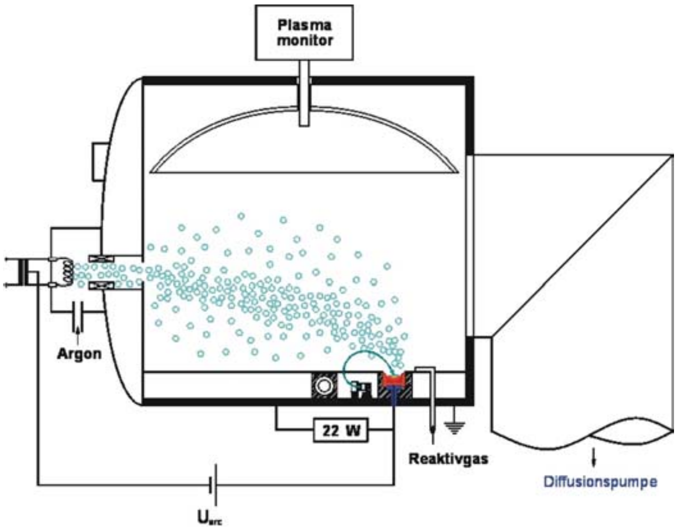

Fig.1: Schematic of a Balzers BAP 800, equipped for a RLVIP Process

2. Experiments / Results

Langmuir Probe measuring equipment:

The Langmuir probe consists of a cylindrical tungsten wire in a glass tube, which can be moved linearly by a pneumatic system. The analysis system allows to follow the results online and to make fast and accurate measurements.

Because of the fast pneumatic motion, the exposure time of the probe to the plasma is very short. Therefore the contamination of the probe by the coating material is not problematic. A gap between the tungsten tip and the glass shielding prevents a conductive connection between the tip and the tube. The measured signal is filtered without harming the characteristic on the basis of a fourier transformation, where specific disturbing frequencies can be deleted well directed.

Faraday-Cup-Measurements:

A Faraday-cup is a special type of an electrostatic probe, which is used for ion beam measurements. Instead of a current-voltage characteristic one measures a present ion beam in the plasma, which doesn’t have to be induced by an attractive probe potential.

The used Faraday-cup consists of an electrode on top of the cup with three grids and a magnetic field placed in front of the electrode. The magnetic field has the task to separate the electrons from the much heavier ions, so that a beam of only ions reaches the electrode. The grids are on different potentials, which allow measuring the ions energy selected, by putting on a variable retarding voltage for the ions in front of the electrode.

After the separation of the electrons in front of the cup the ions pass the first grid, which is grounded. Between the first and the second grid, a variable retarding voltage has to be overcome by the ions. The third grid is put on a negative potential (–30V) in respect of the electrode to prevent secondary electron emission. An incoming ion induces a positive charge on the electrode, which is connected to ground. This positive charge ties an electron out of ground for recombination. An Ampere meter detects this electron. The Faraday cup offers high flexibility and can be positioned at different spots in the recipient. With an increasing retarding potential the measured current decreases. By deriving the function of current over increasing potential (dI/dU_{ret}) one gets the frequency of incoming ions of a certain energy level (≅retarding potential).

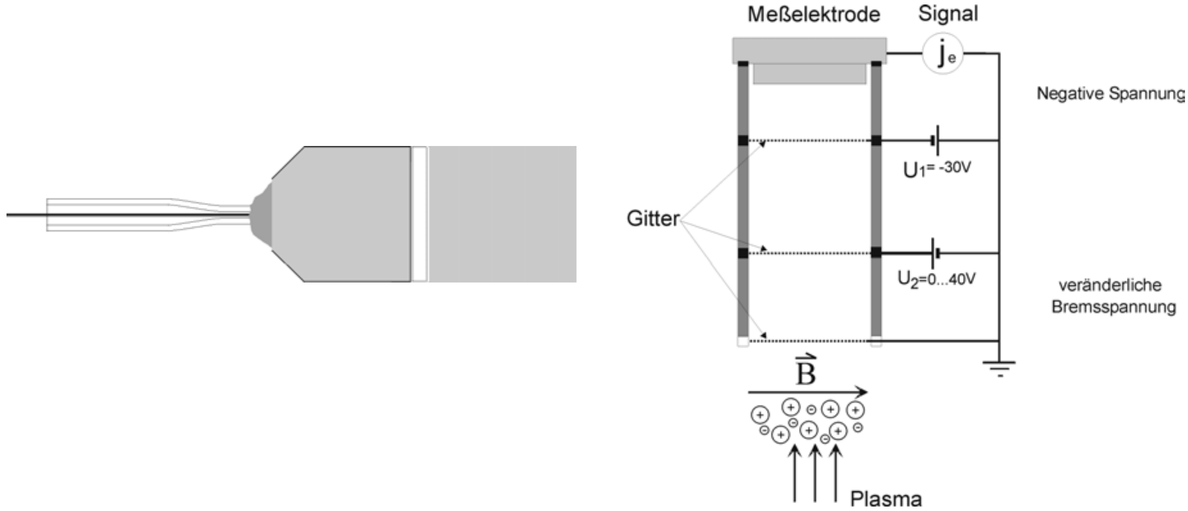

a) b)

Fig.2: a) Schematic of an Langmuir probe tip
b) Schematic of a Faraday Cup

Variation of arc current

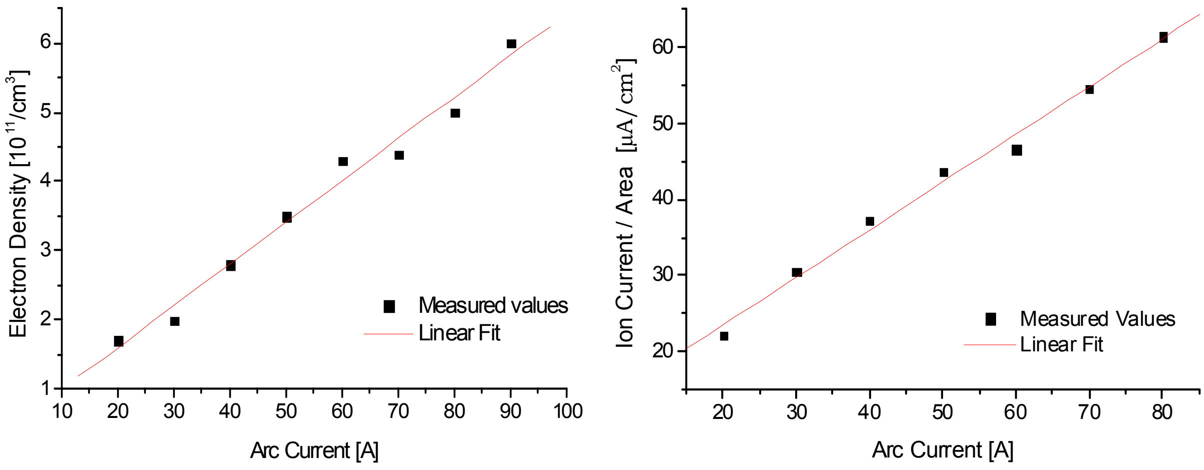

a) b)

Fig.3: a) Langmuir probe measurement: Electron density in dependence of arc current
b) Faraday Cup measurement: Ion current density in dependence of arc current

Variation of total gas pressure

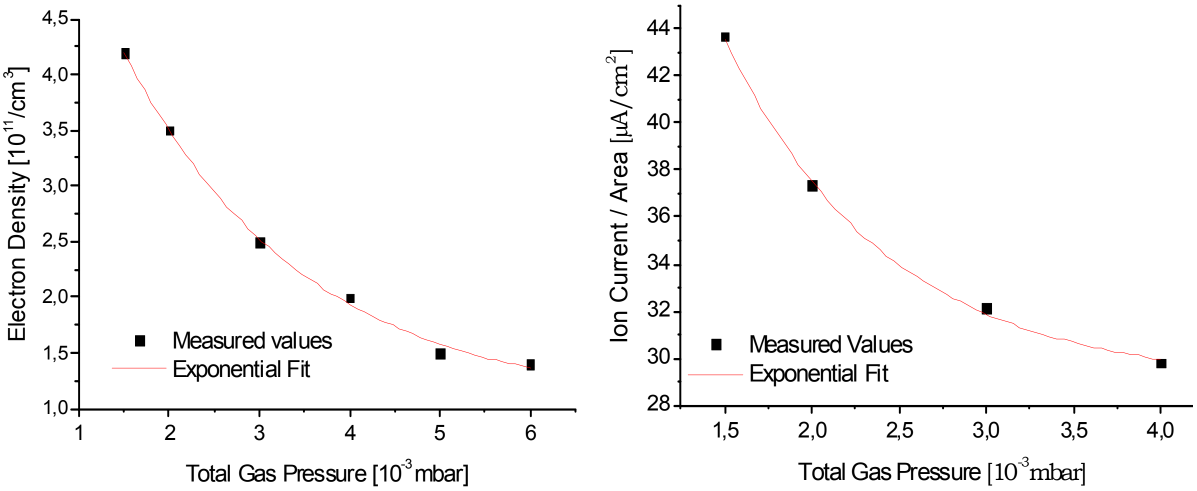

a) b)

Fig.4: a) Langmuir probe measurement: Electron density in dependence of total gas pressure
b) Faraday Cup measurement: Ion current density in dependence of total gas pressure

3. Discussion/Conclusions

Variation of arc current (Fig. 3):

By increasing the arc current, more ionizing electrons are inserted in the plasma. Therefore the electron density increases as well as the ion density. The result is a higher degree of ionisation in the chamber. The relations between arc current and electron density as well as ion current density are directly linear. Not only the degree of ionisation is higher but also the local potential conditions in the recipient change. This leads to a higher acceleration of the ions towards the substrate. The consequence is an increased mean energy of the ions in the plasma and therefore a higher energy input in the films. As a result of these changed conditions, the film density, as well as the intrinsic compressive stress in the films grows. [3]

Variation of total gas pressure (Fig 4):

Increasing the total gas pressure raises the number of collisions in the plasma. This decreases the mean free path of the plasma particles and a kind of thermalization of the ions and neutral particles takes place. The high energetic part of the plasma components decreases, which causes a decrease of the mean energy of the plasma components (electrons and ions).

It is known that the film density is directly correlated to the amount of high energetic ions in the ion beam, whereas the intrinsic compressive stress is correlated to the total energy input in the films [2]. Therefore an increase of the total gas pressure in the recipient decreases film density and the compressive mechanical stress in the films [4].

Another effect is a delocalisation of the locally higher-pressure areas in front of the evaporation source. This has the consequence that ionisation processes take place in a larger volume and not only directly above the evaporation source. The relation between gas pressure and electron density, as well as ion current density shows an exponential decrease (Fig 4).

References

[1] H. K. Pulker, Coatings. on Glass, Elsevier, Amsterdam 1994.

[2] T. Lechleitner, Diploma thesis: Sondendiagnostik des Plasmas bei der Herstellung von TiN-Schichten durch Ionen-Plattieren, Innsbruck 2000

[3] W. Lechner, G. N. Strauss, H. K. Pulker, 41st Annual Technical Conference Proceedings, 287, Society of Vacuum Coaters, Boston 1998

[4] G. N. Strauss, W. Lechner, H. K. Pulker, Thin Solid Films 351, 53-56, Elsevier 1999

Fragmentation and reactivity of energy-selected ferrocenium ions

H. Mestdagh[(a)], C. Alcaraz[(b)], O. Dutuit[(a)], M. Heninger[(a)], R. Thissen[(a)]

(a) Laboratoire de Chimie Physique, Université Paris-Sud - 91405 Orsay - France
(b) LURE, Centre Universitaire - B.P. 34 - 91898 Orsay - France

While investigations on the reactivity of excited bare metal ions ("state-selective reactivity") has been a significant advance in gas phase organometallic chemistry [1], little is known about the dependence of fragmentation and reactivity of ionic metal complexes with their internal energy. In this study, we present results concerning the dissociation of state-selected ferrocenium ions (c-$C_5H_5)_2Fe^+$ commonly called Cp_2Fe^+, as well as their reactions with methanol and ethanol. It is interesting to get more information about the thermochemistry and the reactivity of ferrocene Cp_2Fe and derived ions for different reasons : first it is known to be a very efficient smoke inhibitor in flames [2,3], secondly the Cp (cyclopentadienyl) ligand, widely used in organometallic chemistry, might vary its complexation mode (5, 3 or 1 atoms) with internal energy.

In this study parent ions Cp_2Fe^+ are produced by VUV photoionization of neutral ferrocene using synchrotron radiation (Super-ACO, Orsay), and selected in internal energy by threshold photoelectron-photoion coincidences (CERISES experimental setup [4,5]). Briefly, the apparatus is divided into three differentially pumped regions: the source, the reaction and the detection zones. In the source, state-selected parent ions are formed and can be selected in mass by a first quadrupole filter. State-selected ions are then injected in the second zone which is a RF octopole ion guide where reactions can occur in a collision cell filled with the target gas. In the third zone, either fragment ions or reaction product ions are mass analysed by a second quadrupole filter and detected by microchannelplates. In addition, the long flight time in the octopoles (several hundreds of microseconds) allows studying long-lived metastable ions.

In the study of ferrocenium ion dissociation, several kinds of measurements were performed.

- First, total mass spectra were recorded at different photon energies.

The fragmentation channels are summarized in the Table, as well as the percentage of the observed fragments in the total mass spectrum at a photon energy of 13.75 eV. In addition to the main $CpFe^+$ and Fe^+ fragments, several minor fragments are detected such as $C_{10}H_{10}^{+\bullet}$, which reflects the formation of a C-C bond between the two Cp ligands. Losses of CH_3, C_2H_2 and C_4H_4 also indicate that important structure rearrangements take place before cleavage.

- The appearance energies of each mass-selected fragment ion were measured by recording fragment ion yields as a function of photon energy. Surprisingly, all fragments were found to have the same energy onset, i.e. 13.2 eV photon energy, except for $C_3H_3Fe^+$ (m/z 95). For Fe^+ ions, a sharp increase was observed at 17 eV, above the thermochemical onset of Fe^+ + 2 Cp . The 13.2 eV appearance energy of Fe^+ is thus assigned to the formation of Fe^+ + $C_{10}H_{10}$. The thermochemistry of the ferrocenium ion is not well established; the $CpFe^+$--Cp bond energy is evaluated to 3.7 eV [6] or 3.9 eV [7].The $CpFe^+$ ion experimental onset at 13.2 eV is at 6.55 eV above the Cp_2Fe IP, i.e. about 2.5 eV above the estimated thermochemical onset. This important difference may be attributed either to a dissociation barrier or to kinetic shift.

- In order to evaluate the kinetic shift, coincidence mass spectra have been measured in two different time ranges, by using either the quadrupole mass filter mounted at the exit of the source (detection time in tens of μs) or the quadrupole mass filter mounted after the octopole ion guide (detection time in the hundreds of μs). A shift of the crossing points of the breakdown curves clearly demonstrates the presence of long-lived metastable ions. Figure 1 shows the breakdown curve recorded by the second quadrupole mass filter for the major ions. In this diagram, parent ion lifetimes can be derived in the considered energy range. Results are reported in Figure 2, as well as lifetimes measured from time-of-flight spectra.

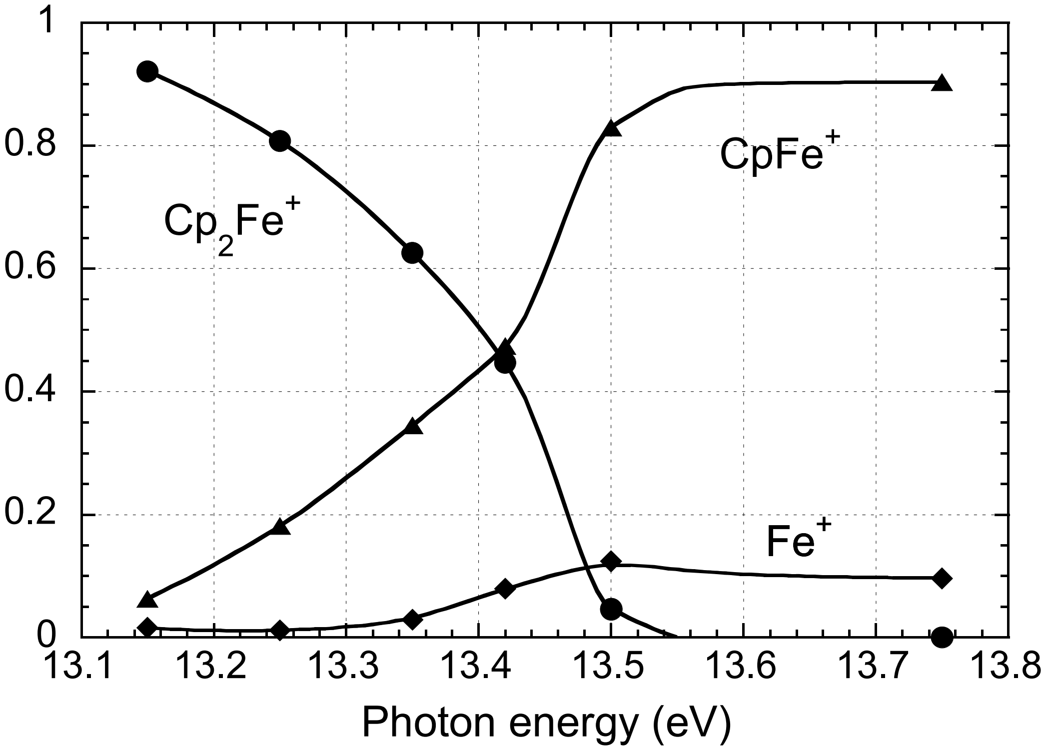

Figure 1 : Breakdown curve of $C_{10}H_{10}Fe^+$, restricted to the most important fragments $CpFe^+$ and Fe^+.

Table : Major fragmentation products of ferrocenium ion.

Mass	Fragment ion(a)	Neutral loss	Appearance threshold (eV)	%, spec. mass 13.75 eV (b,c)	%, coïncid. 13.75 eV(d)
186	$C_{10}H_{10}Fe^+$ (Cp_2Fe^+, parent)	-	6.65	84.2	0
121	$C_5H_5Fe^+$ ($CpFe^+$)	C_5H_5	13.2	11.5	81
56	Fe^+	$C_{10}H_{10}$ 2 C_5H_5	13.2, 17.0	1.9	8
171	$C_9H_7Fe^+$	CH_3	13.2	0.6	5
160	$C_8H_8Fe^+$	C_2H_2	13.2	0.5	3
134	$C_6H_6Fe^+$	C_4H_4 ?	13.2	0.2	3
130	$C_{10}H_{10}^+$	Fe	13.2	0.5	2
95	$C_3H_3Fe^+$	$C_5H_5 + C_2H_2$	17.3	0.1	0

(a) Very minor fragments are found at m/z 158 and 128; their relative intensity increases with increasing photon energy.
(b) Proportion of the considered ion in the mass spectrum, at photon energy Ei = 13.75 eV.
(c) For Ei = 11.5 eV (with LiF cutoff for photons > 12 eV), the parent is the only detectable ion.
(d) Proportion of the considered ion in coincidence with threshold electrons (relative to the sum of ions in coincidence with threshold electrons), at photon energy Ei = 13.75 eV.

- The $CpFe^+$ time-of-flight spectra exhibit two peaks, corresponding to the time-of-flight of the expected fragment and of the parent respectively. The latter corresponds to ions which fragment during their pathway between the source and the detector. Let us note that dissociation lifetime measurements reported in the literature [6,8], also shown in Figure 2, have some ambiguity in the internal energy assignment.

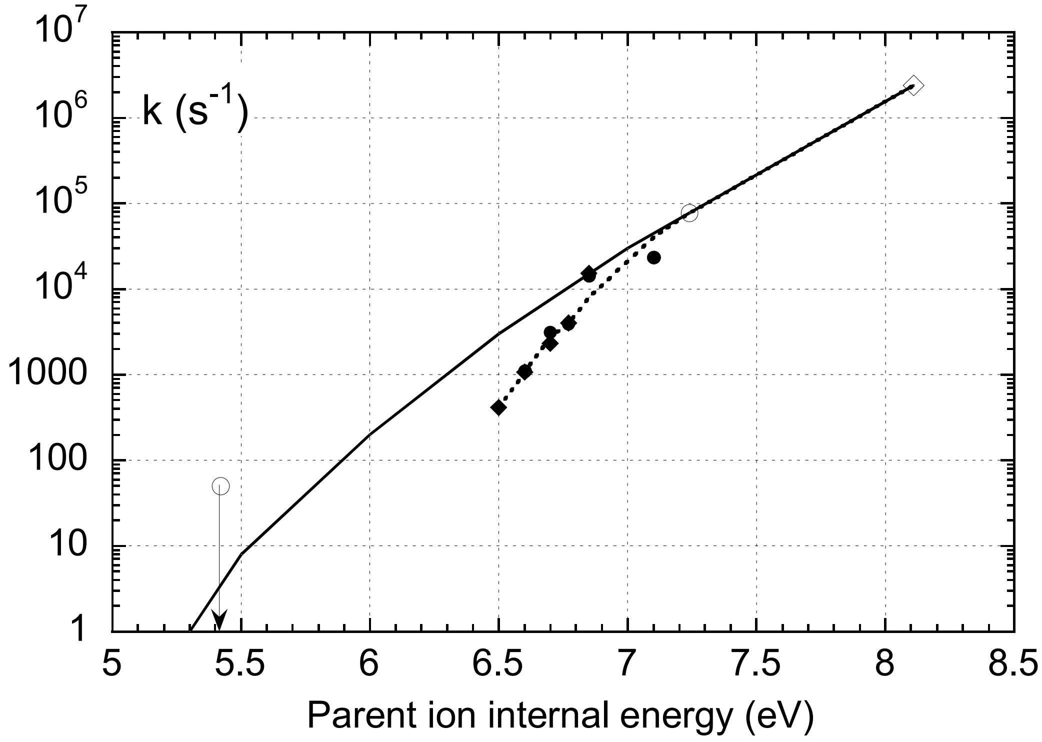

Figure 2: Fragmentation rate constant of Cp_2Fe^+ : ♦ from the fragmentation diagram, ● from the time-of-flight spectra, Literature : O [6] ◇ [8] — RRKM fit [6]

Besides the evidence of a kinetic shift, two arguments seem to indicate the presence of a barrier and a rearrangement prior to dissociation : all fragments have the same appearance energy within experimental errors, secondly fragments such as $C_{10}H_{10}^+$ demonstrate the recombination between the two Cp ligands.

The rate-determining step is thus most probably an isomerization of Cp_2Fe^+, which implies that the Cp loss is not a simple bond cleavage as previously supposed [6,8]. Figure 2 shows a RRKM fit calculated by Faulk and Dunbar [6], assuming a loose transition state. It does not fit well our experimental data. Further RRKM modelling, as well as structure calculations for the transition state, are now necessary to understand the ferrocenium ion dissociation which appears to be much more complex than previously stated.

The reactivity of ferrocenium ion with methanol and ethanol has been investigated as a function of photon energy. It gave quite unexpected results. While no reaction occurs at lower photon energies, several reaction products appear at 13.0 eV photon energy, very close to the fragmentation threshold. It was checked that these ions are really products from the parent ion Cp_2Fe^+, since reaction of each of the different mass-selected fragments with the alcohol leads to different products.

Only one product ion, m/z 201 ("$Cp_2Fe(CH_3)^+$"), comes from single collisions. It is formed in both reactions with methanol and with ethanol.

Several other products appear at the same threshold, mainly m/z 217 ("$Cp_2Fe(OCH_3)^+$") for methanol and 231 ("$Cp_2Fe(OC_2H_5)^+$") for ethanol. Their non-linear increase with increasing reactant gas pressure indicates that their formation involves several collisions.

The observed particular reactivity of the ferrocenium ion just below its fragmentation threshold seems to show that only metastable ions are reactive. It suggests that in order to either dissociate or become reactive, ferrocenium ions have first to isomerize. In order to check this hypothesis, further work is necessary, in particular ab initio calculations of possible isomers.

References

[1] P.B. Armentrout, *Ann. Rev. Phys. Chem.* **41** (1990) 313.
[2] P. Carty, J. Grant, E. Metcalfe, *Applied Organomet. Chem.* **10** (1996) 101.
[3] M. Kasper, K. Sattler, K. Siegmann, U. Matter, H.C. Siegmann, *J. Aerosol Sci.* **30** (1999) 217.
[4] O. Dutuit, C. Alcaraz, D. Gerlich, P.M. Guyon, J. Hepburn, C. Métayer-Zeitoun, J.B. Ozenne, M. Schweizer, T. Weng, *Chem. Phys.* **209** (1996) 177.
[5] J. Loos, D. Schröder, W. Zummack, H. Schwarz, R. Thissen, O. Dutuit, *Int. J. Mass Spectrom.* in press.
[6] J.D. Faulk, R.C. Dunbar, *J. Am. Chem. Soc.* **114** (1992) 8596.
[7] M.F. Ryan, J.R. Eyler, D.E. Richardson, *J. Am. Chem. Soc.* **114** (1992) 8611.
[8] S.J. Han, M.C. Yang, C.H. Hwang, D.H. Woo, J.R. Hahn, H. Kang, Y. Chung, *Int. J. Mass Spectrom.* **181** (1998) 59.